UNIVERSIDADE FEDERAL DE SANTA CATARINA
CAMPUS TRINDADE
PROGRAMA DE PÓS-GRADUAÇÃO EM ENGENHARIA DE AUTOMAÇÃO E SISTEMAS

Adriano Silva Martins Brandão

Modeling and predictive control with defocusing in thermosolar systems

Florianópolis
2023

Adriano Silva Martins Brandão

Modeling and predictive control with defocusing in thermosolar systems

Tese submetida ao Programa de Pós-Graduação em Engenharia de Automação e Sistemas da Universidade Federal de Santa Catarina para a obtenção do título de Doutor em Engenharia de Automação e Sistemas.
Supervisor:: Prof. Julio Elias Normey Rico, Dr.
Co-supervisor:: Prof. Daniel Limón Marruedo, Dr.

Florianópolis
2023

Ficha de identificação da obra elaborada pelo autor,
através do Programa de Geração Automática da Biblioteca Universitária da UFSC.

Brandão, Adriano Silva Martins
Modeling and predictive control with defocusing in thermosolar systems / Adriano Silva Martins Brandão ; orientador, Julio Elias Normey-Rico, coorientador, Daniel Limón Marruedo, 2023.
148 p.

Tese (doutorado) - Universidade Federal de Santa Catarina, Centro Tecnológico, Programa de Pós-Graduação em Engenharia de Automação e Sistemas, Florianópolis, 2023.

Inclui referências.

1. Engenharia de Automação e Sistemas. 2. MPC Híbrido. 3. desfoque. 4. planta solar. 5. neuro-fuzzy. I. Normey-Rico, Julio Elias . II. Marruedo, Daniel Limón. III. Universidade Federal de Santa Catarina. Programa de Pós-Graduação em Engenharia de Automação e Sistemas. IV. Título.

Adriano Silva Martins Brandão

Modeling and predictive control with defocusing in thermosolar systems

O presente trabalho em nível de doutorado foi avaliado e aprovado por banca examinadora composta pelos seguintes membros:

Prof. Eduardo Fernandez Camacho, Dr.
Universidad de Sevilla

Prof. José Luis Guzmán Sánchez, Dr.
Universidad de Almería

Prof. Gustavo Artur de Andrade, Dr.
Universidade Federal de Santa Catarina

Certificamos que esta é a **versão original e final** do trabalho de conclusão que foi julgado adequado para obtenção do título de Doutor em Engenharia de Automação e Sistemas.

GOV.BR
Documento assinado digitalmente
JULIO ELIAS NORMEY RICO
Data: 26/02/2023 05:49:56-0300
CPF: ***.840.859-**
Verifique as assinaturas em https://v.ufsc.br

Prof. Julio Elias Normey Rico, Dr.
Coordenador do Programa

GOV.BR
Documento assinado digitalmente
JULIO ELIAS NORMEY RICO
Data: 26/02/2023 05:50:41-0300
CPF: ***.840.859-**
Verifique as assinaturas em https://v.ufsc.br

Prof. Julio Elias Normey Rico, Dr.
Orientador

Florianópolis, 26 de Janeiro de 2023.

Dedico este trabalho a meu avô, que durante todo o período em que tive a graça de estar em sua presença, sempre me incentivou a estudar e aprender.

Também dedico esta tese a Vicente, meu pequeno sobrinho que me motiva a criar um mundo melhor para ele.

AGRADECIMENTOS

Agradeço primeiramente a Deus.

Agradeço imensamente à minha família, e em especial aos meus pais que incondicionalmente me apoiaram durante todo este período de dedicação aos estudos.

Agradeço aos maravilhosos amigos, antigos e novos, que tenho e que fazem com que a rotina, muitas vezes solitária e desgastante do doutorado, se tornasse um dos períodos mais agradáveis da minha vida. A vossa generosidade não conhece limites!

Agradeço imensamente aos meus orientadores, passados e presentes. Primeiramente ao Prof. Julio, por ser não só uma magnífica referência de pesquisador, mas por toda a orientação ao longo destes anos. Agradeço também ao Paulo, o primeiro coorientador que tive neste trabalho. A sua ajuda na primeira metade deste doutorado foi essencial para que eu conseguisse seguir em frente. Agradeço também ao Prof. Daniel Limón, pela maravilhosa acolhida e orientação desde o meu período em Sevilha. Não menos importante, agradeço ao Prof. Marcus Americano, por ter acreditado que eu era capaz de fazer os estudos de pós-graduação aqui na PosAutomação da UFSC. Muito obrigado!

Por fim, agradeço a ANEEL e Petrobrás, por terem dado suporte financeiro durante a maior parte do meu doutorado. No mesmo sentido, agradeço à CAPES pelo apoio financeiro que possibilitou meu período sanduíche na Universidad de Sevilla, na Espanha.

“Now these points of data make a beautiful line
And we’re out of beta
We’re releasing on time
So I’m GLaD I got burned
Think of all the things we learned
For the people who are still alive”
(GLaDOS, 2007)

RESUMO

Uma das fontes renováveis de energia com maior potencial é a irradiação solar, que fornece uma quantidade significativa de energia. Devido à baixa densidade e grande intermitência associados a esta fonte, a sua exploração envolve a utilização de concentradores, que possuem taxas de conversão que podem ser consideradas baixas quando comparadas com outras fontes de energia. Esta baixa eficiência se reflete nos custos de geração, sendo observado que em todas as técnicas de captação de energia solar, este é muito superior aos custos possíveis com soluções tradicionais. Neste contexto, o desenvolvimento de tecnologias para captação, armazenamento e utilização da energia solar de forma eficiente é crucial para a viabilidade econômica destes processos. Diferentemente das fontes de energias mais tradicionais, a fonte da energia solar não pode ser manipulada diretamente, portanto, o estudo de técnicas avançadas de controle, como o Controle Preditivo Baseado em Modelo (MPC) é interessante para aumentar a viabilidade deste tipo de processo. Este trabalho visa estudar técnicas de controle preditivo em sistemas termossolares com coletores fresnel, em especial MPC híbrido e não linear. Estes controladores são utilizados em problemas que envolvem todo o processo de geração de energia e as interações entre seus componentes, além de considerar o desfoque dos coletores utilizados para captar energia solar. As propostas de controladores apresentadas são desenvolvidas objetivando um custo computacional que permita a implementação em processos reais, além de promover alguma melhora em indicadores de produtividade do processo. É apresentada uma modelagem ótica simplificada de um coletor Fresnel, possibilitando a compreensão de como as características óticas deste tipo de coletor afetam o processo. Além disso, também é mostrado um estudo de possibilidades para o rastreamento do Sol neste tipo de coletor, avaliando os possíveis ganhos que a manipulação individual de cada espelho do coletor pode trazer para o processo. Também são avaliadas propostas de controle preditivo que consideram como o desfoque proposto pelo controlador é implementado. Potenciais erros ou incertezas provenientes da utilização do desfoque como variável manipulada são investigados e, por fim, é proposta uma forma alternativa papa a implementação da estratégia, utilizando redes neuro-fuzzy. Os resultados mostram que os controladores preditivos propostos são capazes de controlar o processo evitando superaquecimento, mas para que esta operação possa ocorrer sem introduzir incertezas consideráveis no controlador, a posição angular dos espelhos deve apresentar valores de incerteza muito baixos. A proposta alternativa de implementação com neuro-fuzzy se mostrou superior quando comparada com a abordagem baseada em otimização.

Palavras-chave: MPC Híbrido, desfoque, planta solar, neuro-fuzzy

ABSTRACT

One of the renewable energy sources with the greatest potential is solar irradiation, which provides a significant amount of energy. Due to the low density and high intermittency associated with this source, its exploitation involves the use of concentrators, which have conversion rates that can be considered low when compared to other energy sources. This low efficiency is reflected in the generation costs, and it has been observed that in all solar energy harvesting techniques, these are much higher than the costs possible with traditional solutions. In this context, the development of technologies to capture, store and use solar energy efficiently is crucial for the economic viability of these processes. Unlike more traditional energy sources, the source of solar energy cannot be manipulated directly, so the study of advanced control techniques such as Model Predictive Control (MPC) is interesting to increase the viability of this type of process. This work aims to study predictive control techniques in thermosolar systems with fresnel collectors, in particular hybrid and nonlinear MPC. These controllers are used in problems involving the entire power generation process and the interactions between its components, as well as considering the blur of the collectors used to capture solar energy. The controller proposals presented are developed aiming at a computational cost that allows implementation in real processes, besides promoting some improvement in process productivity indicators. A simplified optical modeling of a Fresnel collector is presented, allowing the understanding of how the optical characteristics of this type of collector affect the process. In addition, a study of possibilities for sun tracking on this type of collector is also shown, evaluating the possible gains that individual manipulation of each collector mirror can bring to the process. Predictive control proposals that consider how the proposed controller blur is implemented are also evaluated. Potential errors or uncertainties arising from the use of blur as a manipulated variable are investigated and, finally, an alternative way to implement the strategy is proposed, using neuro-fuzzy networks. The results show that the proposed predictive controllers are able to control the process avoiding overheating, but for this operation to occur without introducing considerable uncertainties in the controller, the angular position of the mirrors must present very low uncertainty values. The proposed alternative implementation with neuro-fuzzy proved to be superior when compared to the optimization-based approach.

Keywords: Hybrid MPC, defocusing, solar plant, neuro-fuzzy

RESUMO EXPANDIDO

Uma das fontes renováveis de energia com maior potencial é a irradiação solar, que fornece uma quantidade significativa de energia à superfície da Terra. Devido à baixa densidade associados a esta fonte de energia, a sua exploração envolve a utilização de concentradores da irradiância solar, associados em série e paralelo, formando campos de coletores solares qu aquecem um fluido de trabalho. Devido ao ciclo diário de variação da intensidade da irradiância solar, estas plantas são dimensionadas de forma a captar múltiplas vezes a energia demandada, o que comumente gera situações de superaquecimento, que devem ser evitadas. Para evitar este superaquecimento, é possível reduzir o nível de concentração da energia solar nos coletores, em um processo denominado desfoque. Este desfoque geralmente não é incorporado no sistema de controle da planta, o que pode reduzir a eficiência global do processo tendo em vista que sistemas de segurança tendem a ser conservadores.

Existem poucos trabalhos na literatura que exploram a incorporação do desfoque ativamente no controle do campo solar, sendo que os trabalhos existentes não contemplam como implementar este desfoque em coletores do tipo Fresnel. Este trabalho se dedica a começar a preencher esta lacuna na literatura, fornecendo propostas de estruturas de controle de campos solares com coletores Fresnel que incorporam o desfoque como variável manipulada, e também analisando os impactos da introdução desta atuação nas incertezas dos modelos utilizados no controle.

Para este fim, foram consideradas técnicas avançadas de controle, como o Controle Preditivo Baseado em Modelo (MPC) que é muito utilizado em pesquisas visando aumentar a viabilidade deste tipo de processo. Este trabalho visa estudar técnicas de controle preditivo em sistemas termossolares com coletores fresnel, em especial MPC híbrido e não linear. Estes controladores são utilizados em problemas que envolvem todo o processo de geração de energia e as interações entre seus componentes, além de considerar o desfoque dos coletores utilizados para captar energia solar. As propostas de controladores apresentadas são desenvolvidas objetivando um custo computacional que permita a implementação em processos reais, além de promover melhoras em indicadores de produtividade do processo. Esta tese está dividida em sete capítulos, sendo estes:

Uma introdução à motivação desta tese, bem como apresentação dos objetivos do trabalho;

Uma revisão de aspectos relevantes da literatura pertentes aos estudos realizados nesta tese, como modelagem de plantas termossolares, Controle Preditivo Baseado em Modelo, modelos óticos de coletores fresnel e inteligência artificial;

O primeiro capítulo de contribuições, contendo um estudo comparativo entre duas propostas de controladores já existentes na literatura com uma nova proposta de controlador, que incorpora aspectos das duas anteriores. Os controladores são avaliados em simulações de casos de operação do campo solar, onde se notou que cada uma

das três propostas de controle é capaz de controlar o processo estudado não havendo uma proposta com desempenho claramente superior em todos os aspectos analisados;

O segundo capítulo de contribuições, no qual é apresentada uma modelagem ótica simplificada de um coletor Fresnel, possibilitando a compreensão de como as características óticas deste tipo de coletor afetam o processo. Além disso, também é mostrado um estudo de possibilidades para o rastreamento do Sol neste tipo de coletor, avaliando os possíveis ganhos que a manipulação individual de cada espelho do coletor pode trazer para o processo. O modelo ótico foi validado com dados de um software de referência e com dados do fabricante do coletor modelado, apresentando proximidade com os dados de referência. As estratégias de seguimento do Sol consideradas apresentaram desempenho muito similar entre si, levando à conclusão de que a estratégia de implementação mais simples é a mais adequada.

O terceiro capítulo de contribuições, onde mais uma proposta de controle preditivo que considera o desfoque como variável manipulada, mas desta vez utilizando um controlador preditivo baseado apenas em um modelo não-linear. Este controlador proposto foi comparado com um dos controladores já presentes na literatura e apresentou desempenho em geral superior, apesar de também ter custo computacional mais elevado. Neste capítulo também foram realizadas análises de sensibilidade na estratégia de desfoque proposta, de forma a compreender como incertezas na configuração do coletor poderiam impactar a capacidade do controle de implementar um certo valor de desfoque. Esta análise conclui que para que o controle utilizando desfoque em coletores fresnel possa ocorrer sem introduzir incertezas consideráveis no modelo, a posição angular dos espelhos deve apresentar valores de incerteza muito baixos;

O quarto e último capítulo de contribuições apresenta uma nova proposta de cálculo do desfoque, agora utilizando inteligência artificial, e mais especificamente redes Neuro-Fuzzy, para realizar o cálculo do desfoque com maior velocidade e precisão. Após treinamento com dados obtidos de um software de referencia para modelagem ótica de coletores solares, a nova proposta se mostrou superior quando comparada com a abordagem baseada em otimização tanto na qualidade dos resultados quanto na velocidade de cálculo;

No último capítulo desta tese, é apresentado um resumo dos resultados obtidos, bem como são apresentadas oportunidades para pesquisas futuras a partir dos trabalhos realizados.

LIST OF FIGURES

LIST OF TABLES

LIST OF ABBREVIATIONS AND ACRONYMS

ADMM	Alternating Direction Method of Multipliers
AI	Artificial Intelligence
ANFIS	Adaptative Neuro-Fuzzy Inference System
ANN	Artificial Neural Network
AR	Assessment Report
CSP	Concentrating Solar Energy
DMC	Dynamic Matrix Control
DNI	Direct Normal Irradiance
EMPC	Economic Model Predictive Control
FIS	Fuzzy Inference System
FL	Fuzzy Logic
GPC	Generalized Predictive Control
HTF	Heat Transfer Fluid
IEA	International Energy Agency
IPCC	Intergovernmental Panel on Climate Change
LFC	Linear Fresnel Collector
MINLP	Mixed-Integer Nonlinear Programming
MIQP	Mixed-Integer Quadratic Programming
MLD	Mixed Logical Dynamical
MPC	Model Predictive Control
NLP	Nonlinear Programming
PID	Proporcional Integral Derivative
PNMPC	Practical Nonlinear Model Predictive Control
PTC	Parabolic Trough Collector
PWA	Piecewise Affine
QP	Quadratic Programming
SWERA	Solar and Wind Energy Resource Acessment
toe	tonne oil equivalent
UN	United Nations

LIST OF SYMBOLS

CO_2	Carbon dioxide
t_s	Sampling time
H_p	Prediction horizon
H_c	Control horizon
N_u	Number of manipulated variables
N_y	Number of controlled variables
J	Stage cost of a continuous-time formulation of MPC
J_t	Terminal cost of a continuous-time formulation of MPC
J_d	Discrete cost function
x	States array
f_{nl}	Nonlinear prediction model
f_d	Discrete prediction model
δ	Focus
$T_{in,i,j}$	HTF temperature as it enters collector j at loop i
$T_{out,i,j}$	HTF temperature as it exits collector j at loop i
$T_{out,field}$	HTF temperature as it exits the collecotr field
T_{ref}	Reference for the HTF temperature as it exits the collector field
T_{MAX}	Upper limit for HTF temperature
T_{MIN}	Lower limit for HTF temperature
T_a	Ambient temperature
$\bar{T}$	Average temerature of the HTF in the collector
ρ_f	Specific mass of the heat transfer fluid
τ_a	Time constant of the defocus actuator
C_f	Heat capacity of the heat transfer fluid
A_f	Transversal secction area of the absorber tube
Γ	Collector efficiency
h	Solar hour angle
h_t	Component of the solar hour angle at the transversal plane of the collector
h_l	Component of the solar hour angle at the longitudinal plane of the collector
$\mathbb{I}$	Solar irradiance
L	Collector length
n_{mirr}	Number of mirrors of the fresnel collector
Δx	Distance between mirrors of the fresnel collector
L_{mirr}	Collector mirror width
C_{mirr}	Collector mirror length
L_{abs}	Collector absorber width
E_{abs}	Collector absorber length

E_{abs}	Collector absorber elevation
n_c	Number of collectors at each loop
n_l	Number of loops at the solar field
H_l	Thermal losses of the collector
v_i	HTF flow value at loop i
v_{field}	HTF flow value at the output of the collector field
v_{MAX}	Upper limit for HTF flow
v_{MIN}	Lower limit for HTF flow
$\delta_{out,i,j}$	Effective focus value applied to the collector j at loop i
$\delta_{i,j}$	Focus value passed to the defocus actuator of the collector j at loop i
$\Lambda_{i,j}$	Binary focus value passed to the defocus actuator of the collector j at loop i
U	Array containing all manipulated variables of a MPC controller over the control horizon
U^0	Array containing the current values of all manipulated variables of a MPC controller repeated over the control horizon
Y^0	Measurements of the controlled variables
U_i	Array containing the values of manipulated variable i of a MPC controller over the control horizon
ΔU	Array containing all manipulated variables movements of a MPC controller over the control horizon
ΔU_i	Array containing the movements of manipulated variable *i* over the control horizon
Δu_i	Increment on manipulated variable *i*
u	Manipulated variable of a MPC
$\mathbf{G}$	Dynamic matrix of a linear MPC
$\mathbf{G}_{pnmpc}$	Dynamic matrix of a PNMPC controller
$\mathscr{F}$	Free response
$\mathscr{F}_{pnmpc}$	Free response of a PNMPC controller
$\widehat{Y}$	Array containing the predictions of model for all controlled variables over the prediction horizon
$\widehat{Y}_j$	Array containing the predictions of model for controlled variable *j* over the prediction horizon
$\overleftarrow{Y}$	Past controlled variables' values
y_i	Controlled variable *j*
$\widehat{y}_i$	Controlled variable *j*
$\overleftarrow{U}$	Past manipulated variables' values
0	Array of zeroes
ϵ_i	Small step value for PNMPC computations of manipulated variable *i*
e_{pnmpc}	Prediction error of the PNMPC controller for the current sampling time

η	State of the PNMPC prediction error filter
R_v	Weight matrix of the solar field MPC controller for the v_i movements
R_φ	Weight matrix of the solar field MPC controller for the minimization of φ movements
Q_T	Weight matrix of the solar field MPC controller for the reference tracking of $T_{out,field}$
Q_v	Weight matrix of the solar field MPC controller for the v_i
Q_φ	Weight matrix of the solar field MPC controller for the minimization of φ
A	Point where the solar ray that limits the shadow in the mirror being analyzed touches the mirror to the right
B	Rotation axis of the mirror to the right of the mirror being analyzed
C	Point where the solar ray that limits the shadow in the mirror being analyzed intersects the plane of the mirrors
D	Point where the solar ray that limits the shadow the mirror being analyzed intersects the mirror being analyzed
E	Rotation axis of the mirror being analyzed
β_i	Inclination angle of mirror *i* of a collector
β_i^{min}	Minimal inclination of mirror *i* so that the reflected beam still intercepts the absorber
β_i^{max}	Maximal inclination of mirror *i*so that the reflected beam still intercepts the absorber
S_i	Shaded area width of mirror *i*
ΔS_i	Width of the region between points **E** and **D** in mirror *i*
$S_{H,i}$	Width of the shadow that the mirror to the right of the mirror being analyzed casts on the plane of the mirrors ignoring interference of other mirrors
$\Delta S_{H,i}$	Position of point **C** subtracted from position of point **E**.
ξ_i	Auxiliary angle in triangle $\angle$**ABC**
φ_i	Auxiliary angle in triangle $\angle$**CDE**
$x_{1,i}^{abs}$	Position on the *x* axis of the most extreme point of the range reflected by the mirror *i* when intercepting the plane of the absorber in the west direction
$x_{2,i}^{abs}$	Position on the *x* axis of the farthest point of the band reflected by the mirror *i* when intercepting the plane of the absorber in the east direction
$x_{c,i}^{abs}$	Position on the *x* axis where a radius reflected at the center of the mirror *i* would intercept the plane of the absorber
δx_i	Projection of the width of the mirror *i* in the plane of the mirrors (or absorber) in the direction of the reflected beams
δS_i	Projection of the shaded area S_i of the mirror *i* in the plane of the mirrors (or absorber) in the direction of the reflected beams

ΔL_i	Difference between x_i and $x_{c,i}^{abs}$
σ_i	Angle between the reflected rays in the mirror *i* and the plane of the mirrors' axes
$x_{1,i}^{mirr}$	Projection of $x_{1,i}^{abs}$ at the mirror's plane in the direction of the reflected beams
$x_{2,i}^{mirr}$	Projection of $x_{2,i}^{abs}$ ate the mirror's plane in the direction of the reflected beams
$x_{1,i}^{\prime abs}$	Correction of $x_{1,i}^{abs}$ considering the shadow cast by the absorber
$x_{2,i}^{\prime abs}$	Correction of $x_{2,i}^{abs}$ considering the shadow cast by the absorber
$x_{C,i}^{\prime abs}$	Center of the illuminated width of the absorber
S_i^{mid}	Binary variable that indicates if the shadow cast by the absorber is completely inside mirror *i*
$\mu_A(x)$	Pertinence function for fuzzy set A
IAM	Incidence Angle Modifier
AR5	Assesment report

CONTENTS

1 INTRODUCTION

The growing demand for energy is a consequence of human development from both an economic and social point of view since the increase in industrialization and the demand for various services lead to growth in the consumption of various energy sources. In its latest annual report on energy and carbon dioxide emissions (IEA, 2019a), the International Energy Association (IEA) states that between 2017 and 2018, global energy demand grew by 2.3%, with natural gas accounting for 45% of the growth in energy consumption. The trend of constantly growing energy demands is evident when looking at the historical values presented by International Energy Agency (IEA), shown in Figure 1.

Figure 1 – Historical world energy demand, broken down by source and measured in Mtoe [1] .

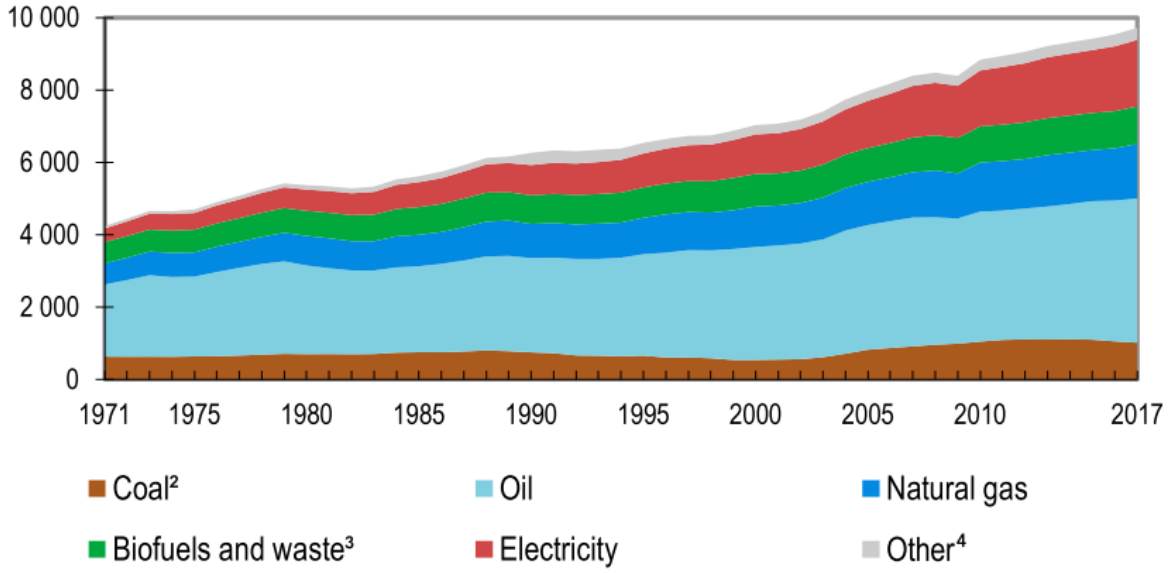

Source: IEA (2019b).

Studies on the greenhouse effect and the factors contributing to its intensification have become necessary, which motivated the United Nations (UN) to create the Intergovernmental Panel on Climate Change (IPCC). This organization is dedicated to providing assessments of the scientific basis of climate change, its impacts, and options for adaptation and mitigation. One of the most important products of the IPCC is the Assessment Report (AR), which presents a compilation of scientific knowledge on the topic and predictions for greenhouse gas emissions scenarios and estimates of the scale of emissions reductions that must be achieved. One of the most important findings of the IPCC Fifth Assessment Report (IPCC, 2021), the most recent report, is the approximately linear relationship between the increase in global average temperature

[1] Tonne oil equivalent.

and the amount of CO_2, as can be seen in Figure 2. This relationship allows the IPCC to set limits on gas emissions from targets for global temperature increase.

Figure 2 – Growth of the Earth's average surface temperature as a function of the cumulative amount of carbon dioxide emissions under various scenarios.

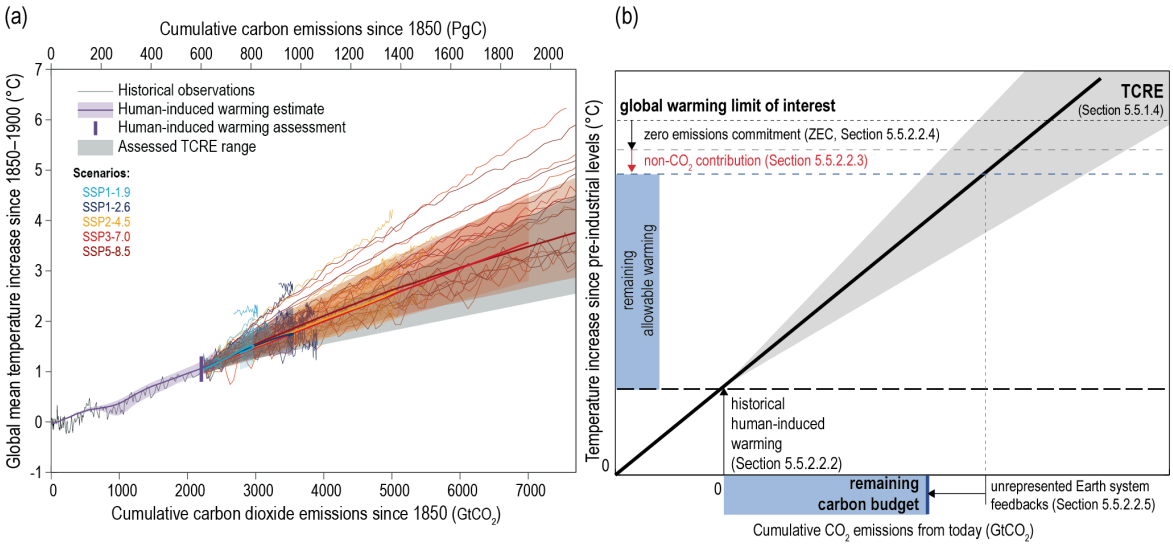

Source: IPCC (2021).

Currently, the most relevant instrument of the UN to define targets for global warming is the Paris Agreement (UN, 2015), in which the goal was set to keep the global average temperature increase below 2℃ as of 2022, preferably below 1.5℃. The scenarios for greenhouse gas emissions made in the AR6 (IPCC, 2021) point out that a large reduction in the emissions of these gases is necessary for it to be feasible to achieve the target in a feasible way, which is not materializing. In this context, there is worldwide interest in the development of clean technologies and renewable sources, considering that these contribute very little to the increase in emissions of CO_2, either because they are inserted in carbon capture cycles, such as biomass, or because they do not involve the burning of fuel, such as hydroelectric, wind and solar energies.

One of the renewable energy sources with the most significant potential for exploitation is solar irradiation, which provides a large amount of energy, even when considering attenuation effects promoted by the atmosphere and clouds (TIAN; ZHAO, 2013). Due to the low density and intermittency associated with this energy source, its exploitation involves the use of concentrators, which have conversion rates between 8 and 30%, which can be considered low compared to other energy sources. This low efficiency is reflected in the energy generation costs, and it has been observed that in all the solar energy harvesting techniques this is much higher than the costs possible with traditional solutions (MACEDO, 2003). In this context, the development of technologies to capture, store and use solar energy in an efficient manner is crucial for the economic viability of these processes (ZHANG et al., 2013). Reports such as Solar

Payback (2018) and Weiss et al. (2017) present data on the use of thermosolar energy in Brazil and in several countries worldwide, showing the potential for expansion of the use of this type of energy in Brazil, both by the level of incident irradiation in the country and by the demands of the industrial and residential sectors.

There are several initiatives that invest in ways to enable the application of solar energy in the energy matrix, such as the Solar and Wind Energy Resource Acessment (SWERA) project, a United Nations program that conducted studies on solar incidence throughout the Brazilian territory, which resulted in the preparation of the Brazilian Solar Energy Atlas (PEREIRA et al., 2017) that enables planning and research of future thermosolar plants in the national territory.

Solar thermal fields present many important characteristics that must be considered in order to safely operate. Constraints such as the upper limit of the operational temperatures of the heat transfer fluid or the maximal flow possible with the avaliable pumps challenge the control structures of these plants, which must also deal with considerable enviromental disturbances, such as clouds. Unlike the more traditional energy sources (fossil fuels, hydroelectric), the solar energy source cannot be directly manipulated, which hinders the availability and economic viability of its use (CAMACHO; SAMAD, et al., 2011). These limitations motivate the study of advanced control techniques, such as Model Predictive Control (MPC), to increase the viability of this type of process. This type of controller can natively deal with operational constraints, operation objectives, and multivariable processes, as is the case of solar plants. Three variations of MPC are widely studied nowadays and have great potential for applicability in thermosolar power generation processes are the Hybrid, Distributed, and Stochastic Predictive Control.

The term MPC does not refer to a specific control strategy, but to a set of algorithms based on prediction and optimization. In these methods, at each controller iteration, the future behavior of the process is predicted from a mathematical model, measurements, and control actions provided by an optimizer. Figure 3 contains a representation of the prediction at one instant. It can be seen in the figure that the proposed actions generate, for example, a predicted behavior that decreases the distance between the value predicted by the model and a reference trajectory. At the end of the iteration calculation, the first control action calculated at the horizon is applied to the process, new measurements are taken, and a new iteration of the controller is started.

Figure 4 presents a general representation of the relationships between the process, model, and optimizer in MPC.

This structure with model and optimizer allows great flexibility of formulations to be used in the controllers, which can be observed given the numerous versions of MPC in the literature. It is possible to include feedforward action when considering the effect of measured perturbations, future reference trajectories, band controls among others

Figure 3 – Representation of the predictions and control actions calculated in the MPC prediction horizon.

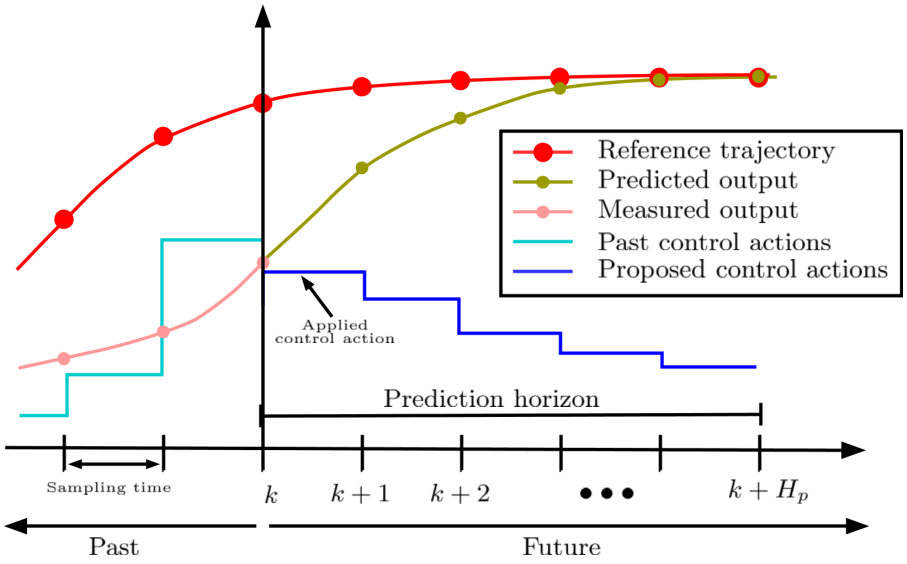

Source: Adapted from Camacho and Bordons (2002).

Figure 4 – Block diagram representing the main elements of the MPC.

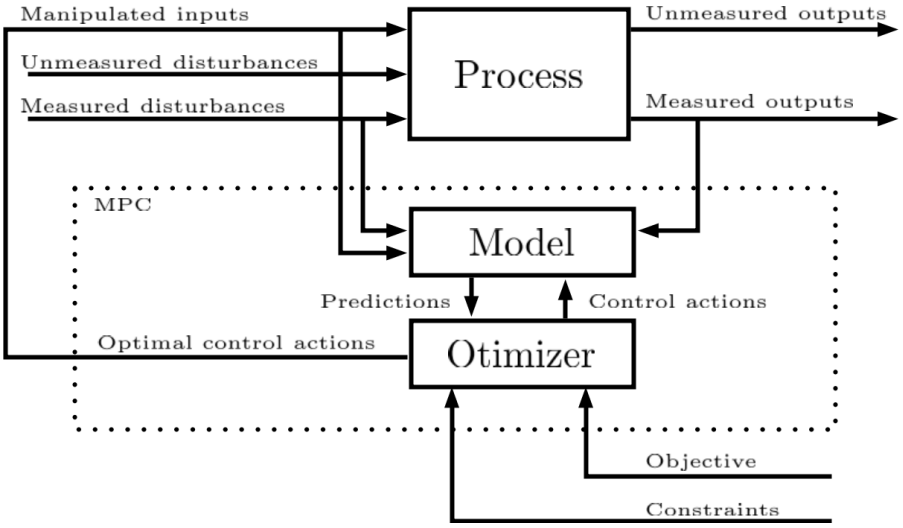

Source: The author.

(CAMPOS et al., 2013).

One of the most important elements of the MPC is the optimizer, which proposes control actions in an iterative process in an attempt to achieve an objective and respect constraints. The objectives and constraints are mathematical expressions established in the controller design phase and can take several forms. In the objectives, quadratic functions are commonly used to penalize the error in the reference tracking, resulting in Quadratic Programming (QP) problems, but elaborate formulations such as Economic Model Predictive Control (EMPC) (RAWLINGS et al., 2012; FONTES et al., 2022) use complex objectives that associate economic and control performance terms. More complex formulations can result in optimization problems of classes such as Mixed-

Integer Quadratic Programming (MIQP) (AXEHILL; HANSSON, 2005; BEMPORAD; NAIK, 2018) or even Nonlinear Programming (NLP) (BIEGLER, 2021).

In Hybrid MPC, both continuous and binary/logical variables are used in the process model and in the controller formulation (VILJOEN et al., 2020; YANG et al., 2022), allowing decisions such as deactivating or activating parts of a process, which is desirable, for example, when partial shading occurs in a solar field and you want to avoid thermal energy loss to the environment. The optimization problems to be solved by MPC can be very complex, especially in large-scale systems.

Heliothermal Plant Control

To enable the operation of heliothermal plants, there are two main controls: sun tracking and control of thermal variables (CAMACHO; GALLEGO, 2015). Figure 5 presents an illustration of a structure that uses these two types of control of a solar field. The local PID controls in the figure are charged with locally controlling the positions of the mirrors or collectors. These controllers receive the references from the forward control so that the system's power generation achieves its objectives. Thus, the control of thermal variables is performed in a layer above that of the mechanical systems for focusing and tracking the sun. This tracking consists of positioning the moving parts of the collector so as to maximize the amount of irradiation incident on the absorber. In flat or parabolic cylinder collectors, the best possible position is where the solar irradiation falls perpendicular to the plane of the collector, while fresnel collectors or plants with a central tower require individual adjustment of several mirrors to allow concentration of the solar energy (CAMACHO; BERENGUEL; GALLEGO, 2014).

Figure 5 – Hierarchy of control systems in a heliothermal plant.

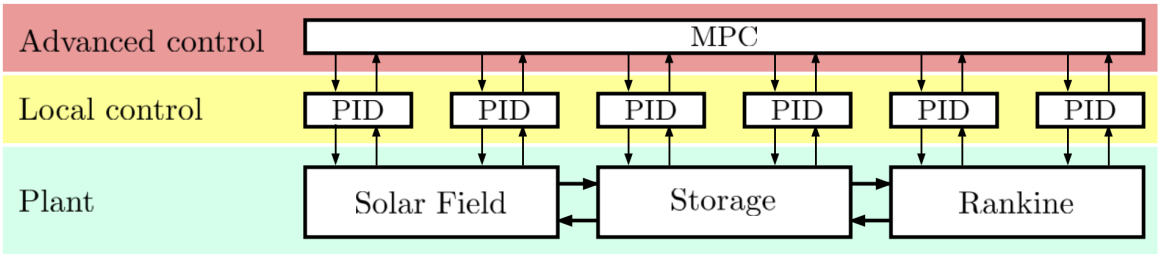

Source: The author.

In the literature, there are several works about the control of thermal variables of solar plants, being a review on control strategies applied to direct steam generation plants found in Aurousseau et al. (2016). The work of Pintaldi et al. (2019) uses predictive control for solar cooling plants, considering thermal energy storage systems. The control of the solar field to avoid thermal fluid overheating, considering collector defocusing, is investigated by some recent works. Sánchez et al. (2018) presents a novel control strategy for overheating prevention of the HTF by defocusing the collectors on a

commercial 50 *MW* parabolic trough plant model by means of a Gain Scheduling MPC. It models how the defocusing is implemented by offsetting the solar tracking angle of the Parabolic Trough Collector (PTC) by some known correlation between the collector inclination and the solar concentration ratio. (ARAÚJO ELIAS et al., 2019) presented an ON/OFF defocus strategy as well as a partial defocusing control strategy taking into account intermediate focusing positions and using hybrid PNMPC controllers. Both approaches were applied on a model of the ACUREX parabolic collectors based solar field (located at the Solar Platform of Almería, Spain), but replacing the optical efficiency terms considering the use of fresnel collectors. The work of Alhaj and Al-Ghamdi (2018) also proposes a control strategy with defocusing, aiming at reducing energy expenditure with the pumping of the thermal fluid.

Most of the existing works that propose proportional defocusing of collectors do not specify how this strategy can be implemented, which may be impossible depending on the actuators or collector type. In the case of fresnel collectors, to the best of the author's knowledge, there are no works that consider how the implementation of the defocusing will occur. The present work intends to address both aspects of the control of the thermal variables of the solar field and the tracking of the sun and defocusing of collectors, analyzing how proportional defocusing can be implemented in fresnel collectors and the challenges of introducing this manipulated variable in the control structure.

1.1 GENERAL OBJECTIVE

To develop and to analyze control solutions that increase the efficiency of solar thermal energy collecting systems through Model Predictive Controllers and defocusing strategies of fresnel collectors.

1.2 SPECIFIC OBJECTIVES

- To develop a simplified optical model of a fresnel collector to study sun blurring and tracking techniques;
- To investigate control techniques for solar fields acting simultaneously on the flow and focus of collectors;
- To develop formulations without using mixed integer programming in controllers acting with collector defocus;
- To analyze the performance of the proposed solutions with others already existing in the literature;

- To analyze the possible challenges presented by the use of defocusing as a manipulated variable.

DOCUMENT STRUCTURE

This thesis is divided as follows: Chapter 2 presents a review of the literature on control in renewable power generation processes and predictive control. Chapter 3 presents the first contribution of this thesis, with a hybrid predictive control formulation for control of solar thermal fields, which was published in the article Brandão, Costa Mendes, Elias, et al. (2019) and presented at Solar World Congress 2019. Chapter 4 presents the second contribution of this work, consisting of a simplified optical model for fresnel collectors and some analyses of solar aiming strategies, which was published in the article Brandão, Costa Mendes, and Normey-Rico (2022). In Chapter 5, the complete defocusing MPC structure proposed in this thesis is presented and evaluated with nonlinear controllers. This chapter also analyses the effects of different sources of uncertanties on the expected precision of the defocusing actuation. The results of this paper resulted in the article Brandão and Normey-Rico (submitted) that was submitted to Solar Energy journal. Chapter 6 presents the last contribution of this thesis, consisting of proposals for improving precision and computation time of the defocusing algorithm with the use of neuro-fuzzy models, which resulted in Brandão, Chicaiza, et al. (2023), which was submitted for the IFAC World Congress 2023. This chapter was developed in cooperation with Phd student William D. Chicaiza, during my period at Universidad de Sevilla, in Spain. Finally, the conclusion of the document is made with an overview of the work, presentation of future research perspectives, an overview of the challenges along the way, and a brief report on the chronological advance of the PhD process that culminated in this thesis.

2 THEORETICAL BACKGROUND

In this chapter, a review of the main topics related to the research themes presented in this document is carried out. Initially, a review of control techniques applied in thermosolar energy generation systems is made. Next, reviews are presented on the types of predictive controllers to be considered: Nonlinear, Hybrid, Distributed, and Stochastic.

2.1 HELIOTHERMIC PLANTS

There are several ways to take advantage of the energy from the sun, from using photovoltaic cells to generate electricity (BRAGA et al., 2019) to drying fruits for snacks (MNKENI et al., 2001). One of the most studied technologies for harnessing solar thermal energy is Concentrating Solar Energy (CSP). Plants that use CSP capture solar radiation and concentrate it in a receiver (called absorber), through which a Heat Transfer Fluid (HTF) circulates, which is heated by the solar energy that reaches the receiver. Solar radiation can be concentrated through lenses or mirrors, the latter being more common (LOVEGROVE; STEIN, 2012). The set of reflecting and absorbing mirrors is referred to as a collector, the main types of collectors being PTC, Linear Fresnel Collector (LFC), and the parabolic disk collector (Figure 6). These collectors are arranged in series and parallel, forming a field of solar collectors, enabling the capture of solar irradiance over a large area and raising the HTF to high temperatures.

*

Figure 6 – Solar tracking on different types of solar collectors.

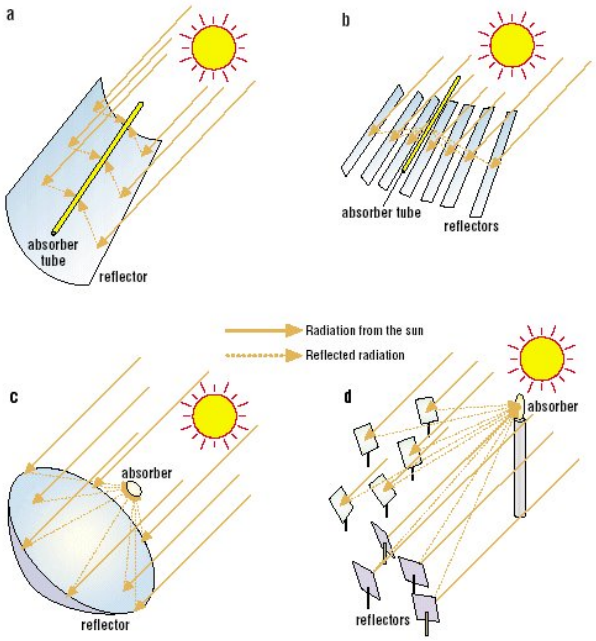

Source: Silvi (2011).

The thermal energy captured by the solar field can be used directly, or it can feed a thermodynamic cycle (such as the Rankine cycle) coupled with a generator, enabling the generation of electrical energy (LOVEGROVE; STEIN, 2012). Heliothermic power plants can be divided into three subsystems: The solar field, composed of collectors and storage tanks of HTF; The heat transfer system, in which the thermal energy from the field is transmitted to the thermodynamic cycle; and the power block, which contains the stages of the thermodynamic cycle and the generator (RETORTA et al., 2018). A representation of the basic structures of this type of plant is presented in Figure 7.

Figure 7 – Overview of a solar thermal plant.

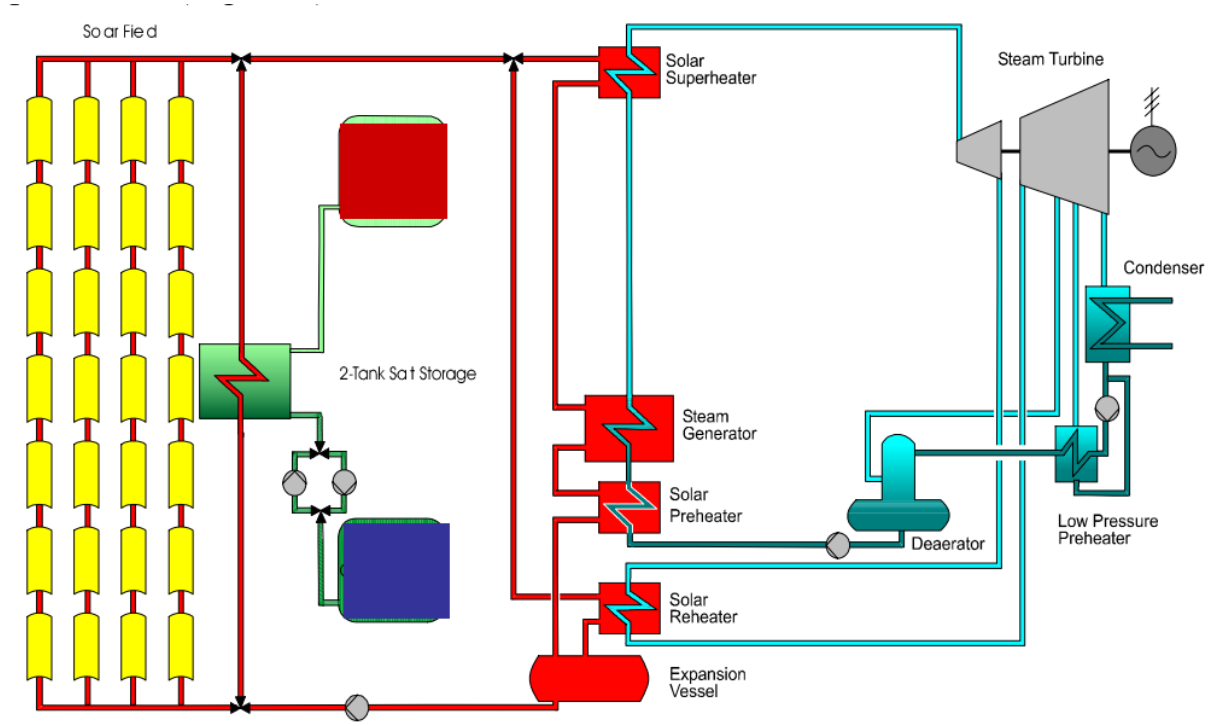

Source: Adapted from U.S. Department of Energy (2011).

The operation of heliothermic plants presents several challenges, such as control of collectors, prediction of solar irradiation, control of energy conversion systems and general control of the process (CAMACHO; BERENGUEL; RUBIO, et al., 2012). As solar irradiance is the energy source of solar plants, predicting this variable is very important for plant planning and operation, which motivated studies that use sky imaging for short-term estimates, such as Achleitner et al. (2014), Darbali-Zamora et al. (2015) and Cervantes et al. (2016).

The control of the collectors must ensure that, even with the relative movement of the Sun, there is concentration of solar energy in the absorbers. How this is done depends on the type of collector and this type of problem is known as solar aiming or solar tracking.

In PTC collectors (BAKHTIARI; BIDI, 2015) (as shown in item a of Figure 6), *tracking* is performed by rotating the reflecting mirrors around the collector tube. In this

case, the strategy is simple and consists of keeping the collector opening perpendicular to the incident rays, in order to make them converge to the focus of the parabola. Due to the optical properties of parabolic mirrors, if the rays do not fall perpendicular to the collector's mirror opening, the sun's rays will not converge on a single focal point, which can impair the capture of solar energy. In the case of parabolic disk collectors (item c in Figure 6), the process is similar to PTC collectors, but a second degree of freedom is introduced in the manipulation of the mirrors. In the case of fresnel collectors (PINO, F. et al., 2013) and central tower (ELSAYED et al., 2018) (b and d items in Figure 6, respectively), tracking is more complex because there are several mirrors with different inclinations, and factors such as mirror shading and cosine losses. A brief review of systems in *tracking* can be found in Jamilu (2017).

In the literature, there are several proposals for optical models for fresnel collectors, but these are mostly very generic and complex, being developed with the objective of design and analysis of collector efficiency. In these cases, techniques from *ray tracing* are used in these models, as presented in Osório et al. (2016), Eddhibi et al. (2017) and Benyakhlef et al. (2014). This type of model can present a high computational cost, being unfeasible in predictive control applications. There are proposals for models that do not use *ray tracing*, such as the one proposed by F.J. Pino et al. (2013), but these are often too complex, which also makes the computation cost high. The work of Barbón et al. (2020) presents a study on the impact of the actuation time of *tracking* and the performance of the collector, which is pertinent to evaluate the maximum sampling time that this system should have.

2.2 FRESNEL COLLECTOR FIELD MODELING

In order to study the fresnel collectors and not having easy access or flexibility to perform experiments in this type of process, it was necessary to study what the literature had avaliable in regard to modeling. The following sections present some of these literature proposed models, considering the thermodynamics and optical characteristics of Linear Fresnel Collectors.

2.3 OPTICAL MODELS FOR FRESNEL COLLECTORS

The first step of the development of the collector optical model is the definition of a set of parameters that describes the collector and the direction of the sun's rays. In this work, a Fresnel collector is considered, with n_{mirr} plane parallel mirrors, equidistant Δx meters, with length C_{mirr} and width L_{mirr}. The absorber is also considered to be flat, with C_{abs} length, L_{abs} width and E_{abs} elevation relative to the plane of the mirrors. The mirrors are numbered from west to east, with the first mirror being the westernmost (towards the sunset) and the last mirror the easternmost (towards the sunrise). A x-

coordinate axis is also defined, originating in the central axis of the absorber. The variables $x_i, i = 1, ..., n_{mirr}$, represents the position of the rotation axis of each mirror i on the x axis. Figure 8 presents a visualization of these parameters in a collector.

Figure 8 – Detailing of some of the collector's parameters.

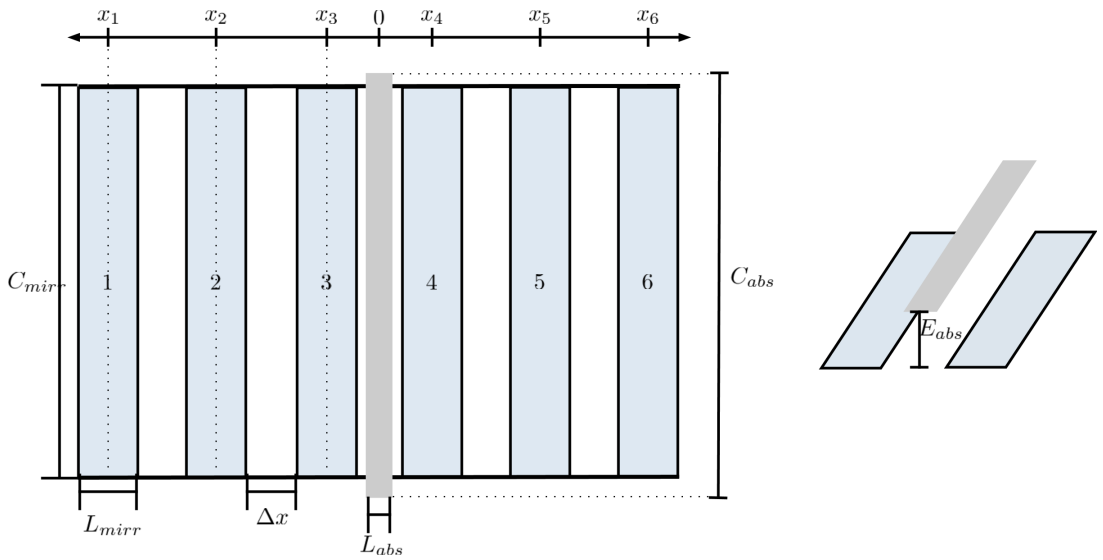

Source: The author.

Figure 9 presents the variables used to define the solar rays. The angle θ represents the angle of incidence of the solar ray in the horizontal plane, measured from zenith location (i.e. solar zenith angle), and can be obtained by equations that relate it to the day, time, and position of the collector, as presented in Sandia National Laboratories (2018). This angle can be decomposed into two perpendicular components:

- h_l, the projection of θ in the longitudinal plane of the collector;
- h_t, the projection of θ in the transversal plane of the collector. It admits negative values from sunrise until solar noon and positive values from solar noon until sunset.

The value of θ as well as the projections can be calculated through the following expressions, given by Pigozzo (2019):

$$h_t = tan^{-1}(tan(\theta)\, sin(\gamma_S)), \tag{1}$$

$$h_l = tan^{-1}(tan(\theta)\, cos(\gamma_S)). \tag{2}$$

Besides the parameters presented above, it is also necessary to define two parameters of each mirror (illustrated in Figure 10):

- β_i is the smallest angle between the plane that passes through the rotation axes of all mirrors and mirror i. It is positive when the mirror is rotated clockwise and

Figure 9 – Detailing of the angles describing the sun rays direction.

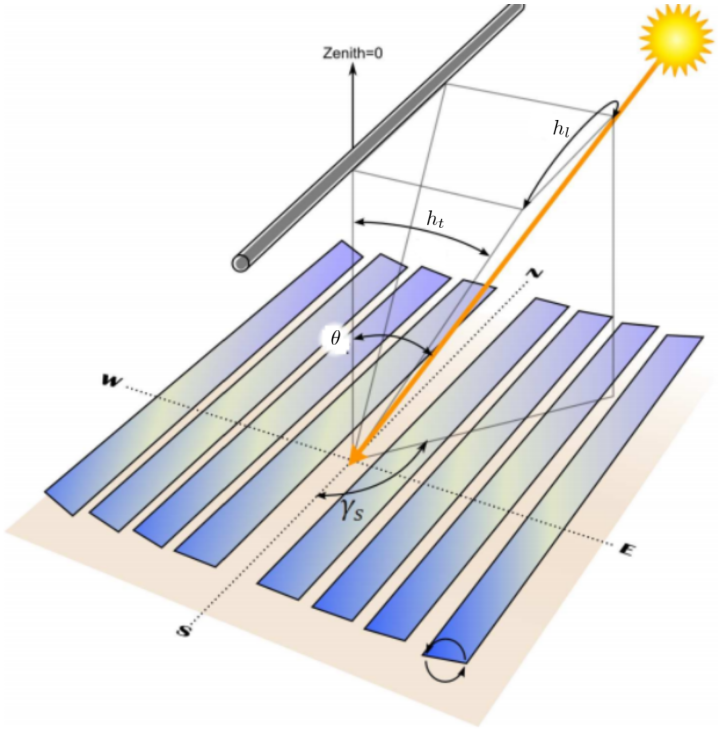

Source: Adapted from Wagner (2012).

negative when the mirror is rotated counterclockwise (as shown in Figure 10). It is limited between -90^o and 90^o and is the variable manipulated to perform the solar tracking;

- μ_i is the angle between the straight line passing through the center of rotation of mirror *i* and center of the absorber, and the horizontal plane (segment $\overline{AB}$ in Figure 10), always measured by the sunrise side. This angle is always positive and can be calculated by the following expression:

$$\mu_i = tan^{-1}\frac{E_{abs}}{x_i}. \tag{3}$$

The first concept to be considered in the model is the reflection of the solar rays in the mirrors. According to Snell's Law, light inciding in a reflective surface will be reflected at an angle equal to the angle of incidence to the normal of this surface. In the case of a mirror *i* of the collector, the angle of incidence of solar rays will be denoted by θ_i, and its transversal and longitudinal projections denoted by $\theta_{t,i}$ and $\theta_{l,i}$ respectively. Figure 11 presents an illustration of these angles.

Note that for solar tracking on a Fresnel collector, $\theta_{t,i}$ is very important, being affected by both the sun's rays' direction (h_t) and the inclination of the mirror (β_i), and is given by Equation (4).

$$\theta_{t,i} = h_t + \beta_i. \tag{4}$$

Figure 10 – Detailing of some of the mirror's parameters.

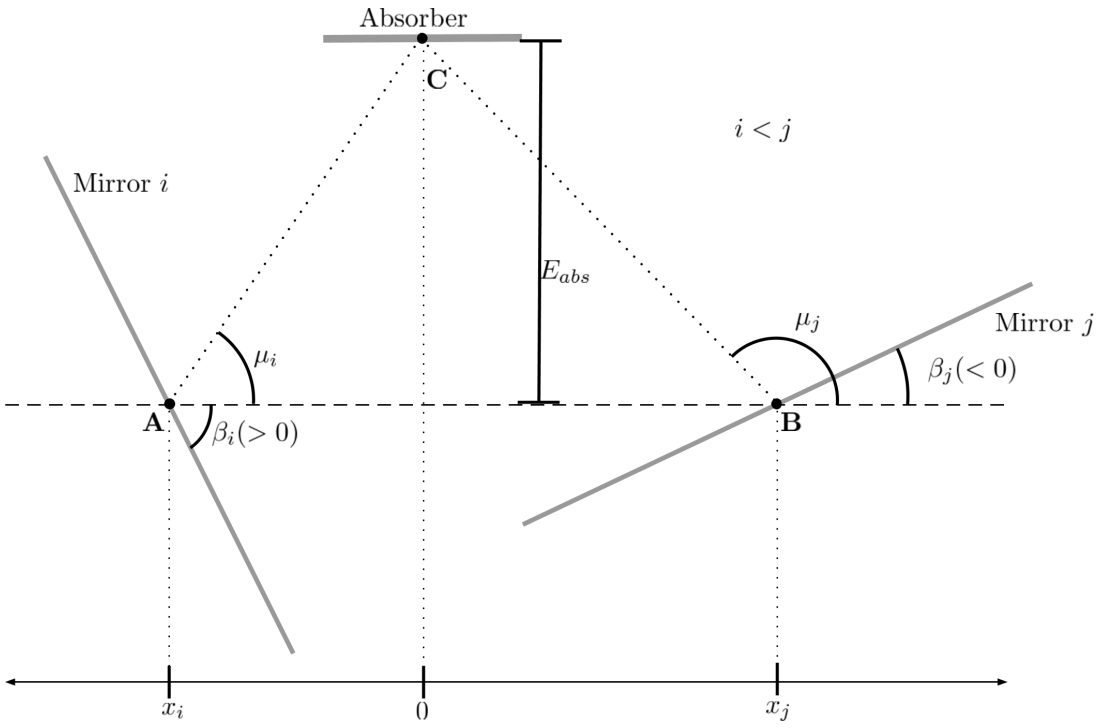

Source: The author.

With the basic parametrization of the problem defined, the different proposals for optical model can be analyzed.

The literature presents some optical models for Fresnel collectors, as presented in (HUANG et al., 2014; TSEKOURAS et al., 2018; CAGNOLI et al., 2018), but these models use ray-tracing techniques, and thus, they have an inherent elevated computational cost, associated with the multiple calculations necessary for the implementation of the ray-tracing technique. Analytical models are also available, such as the one presented in Wang et al. (2020), that presents a simple and accurate model, but assumes an specific aiming strategy, therefore cannot be used to study different tracking techniques or defocusing.

The analytical model proposed by F. J. Pino et al. (2013) considers two and three dimensional characteristics of the collector and incorporates a thermal model of the absorber, but the energy effects of the optical part of the model are validated indirectly, with temperature data from a real collector, thus taking into account the combined behaviour of the thermal and optical models. The model proposed in Zhu (2013) is accurate and does not assume an specific aiming strategy, but demands a considerable computation time, around 3 s per evaluation, that can impede its use on prediction models of advanced controllers.

In addition to optical models, thermodynamic models are very important to describe the behavior of collectors and collector fields. These models relate the discharge temperature of each loop and field to the flow rate of HTF which is heated by the

Figure 11 – Detailing of the angles describing the sun rays direction.

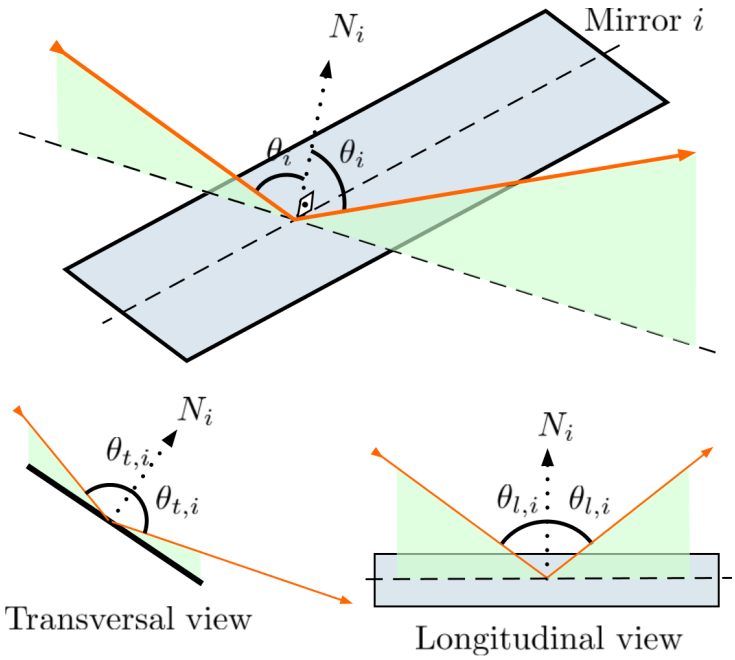

Source: Adapted from (WAGNER, 2012).

radiation concentration in the collector. Due to the high length of the pipes through which the HTF moves, the effect of the transport delay can be significant in this type of process and can make it difficult to implement simple control strategies. The ambient temperature is also important in these models as it directly contributes to the thermal losses in the process. There are several proposals for thermodynamic models for solar fields, as shown in Robledo et al. (2011), Padilla et al. (2011), Spoladore et al. (2011) and Tian, Perers, et al. (2018).

2.4 THERMODYNAMIC MODEL

The literature has some models that represent the dynamics of heat exchange in the absorber tube of a linear collector. Some more sophisticated models, such as Cagnoli et al. (2018), Ordóñez et al. (2020) and Padilla et al. (2011) explicitly consider the interactions between glass insulation, absorber tube, HTF and secundary reflector in order to better estimate the thermal energy exchange. Other models consider a disributed parameter structure, such as Spoladore et al. (2011) and Carmona (1985) to better characterize the distributed nature of the process, which is especially relevant when considering lengthy loops of solar collectors. More general approaches, such as the one presented by Tian, Perers, et al. (2018) use quasi-dynamic models to represent flat plane and PTC collectors in a solar field. This type of model, although useful for process analysis, is not suited for control related works as these impose relevant changes to the inputs of the model.

Although validated and precise, the previouslly presented models can require

much computational effort when composed of partial differential equations. In order to be used on real-time MPC applications, lumped parameter models are better suited as these usually do not requite as much time to be solved. In this sense, Robledo et al. (2011) uses a lumped model coupled with an optical description of a fresnel collector, which is validated with experimental data for temperature but not for the optical components of the model. Araújo Elias et al. (2019) uses an adapted lumped version of the distributed model proposed by Carmona (1985) and that is extensively used in this thesis. This model represents the ACUREX collector field, with Therminol 55 thermal oil as the HTF. In this model, the expression for the output temperature of HTF at each collector is given by eqs. (5-8):

$$\rho_f C_f A_f T_{out,i,j}(t) = \delta_{out,i,j}(t)\,\Gamma(h)\,\mathbb{I}(t) - \rho_f C_f \frac{v_i(t-d_c)(T_{out,i,j}(t)-T_{in,i,j}(t))}{n_c L} - \frac{H_l(\bar{T}(t), T_a(t))}{n_c L}, \tag{5}$$

$$\bar{T}(t) = \frac{T_{out,i,j}(t) + T_{in,i,j}(t)}{2}, \tag{6}$$

$$\rho_f(t) = 903 - 0.672\,\bar{T}(t), \tag{7}$$

$$C_f(t) = 1820 + 3.76\,\bar{T}(t). \tag{8}$$

With:

- $T_{in,i,j}$: Input temperature of HTF at loop i, collector j;
- $T_{out,i,j}$: Output temperature of HTF at loop i, collector j;
- T_a: Ambient temperature;
- v_i: Flow of HTF at loop i;
- $\delta_{out,i,j}$: Applied focus value at loop i, collector j

The other parameters are specific mass (ρ_f), heat capacity (C_f), transversal secction area of the absorber tube (A_f), collector efficiency (Γ), the solar hour angle (h), solar irradiance ($\mathbb{I}$), collector length (L) and number of collectors at each loop (n_c). The function H_l represents the thermal losses at the collector.

As the defocusing of the collectors involves the movement of mechanical parts such as mirrors, there is a dynamic to be considered for changes on the focus. This actuation dynamic is modeled as a first order differential equation with unitary static gain and a time constant τ_a as shown on Equation (9):

$$\tau_a \frac{d\delta_{out,i,j}(t)}{dt} = -\delta_{out,i,j}(t) + \delta_{i,j}(t). \tag{9}$$

Since one of the goals of the controllers considered in this thesis will be to maximize the energy at field discharge, it is not necessary to calculate the mixture

temperature of the union of the parallel loops. Safety considerations regarding thermal fluid are performed only with the fluid temperature in each loop. That is, each loop is modeled as an independent entity. The connection between loop models occurs only in the field flow restriction: The sum of the flow rates of all loops cannot exceed the maximum possible flow rate for the field. The total flow rate in a field with n_l loops is given by Equation (10).

$$v_{field}(t) = \sum_{i=1}^{n_l} v_i(t). \tag{10}$$

2.5 NONLINEAR MODEL PREDICTIVE CONTROL

To represent characteristics such as transport delay, variation of properties of HTF and the dynamics between process variables with fidelity, it is interesting to use nonlinear models such as the one presented in Equation (5). Good models are essential for developing predictive controllers, as they allow the understanding of future process behavior in order to the determine the most appropriate control action. In the case of solar fields, these controllers typically manipulate the load flow rate of each solar field loop in order to control the temperature behavior at the field discharge, as seen in Camacho, Gallego, Escaño, et al. (2019b) and Aurousseau et al. (2016).

In the control of heliothermic fields with concentrators, the control hierarchy can follow a structure like the one presented in Figure 12, with an upper layer that controls the temperature of the thermal fluid in each loop manipulating the flow, and systems at a lower level, that perform the tracking of the Sun and manipulate the mirrors.

Figure 12 – Hierarchy of the control system for a solar thermal loop with two collectors.

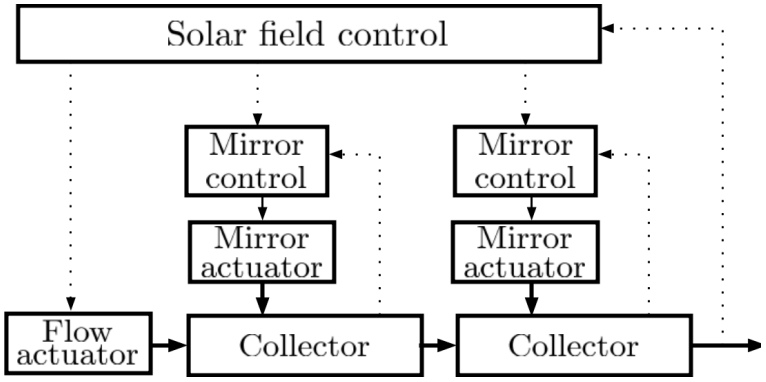

Source: The author.

A review of the types of predictive controllers to be studied in this work will be presented below.

The definition of a controller Model Predictive Control (MPC) consists in the formulation of an optimization problem that calculates the desired control actions. A generic way of representing this type of problem can be found in Equation (11).

$$\min_{U} \int_{0}^{H_p} J(x(t), u(t))\, dt + J_t(x(H_p)) \tag{11a}$$

Subject to

$$\dot{x} = f_{nl}(x(t), u(t)), \qquad t \in [0, H_p], \tag{11b}$$

$$x(t) \in \mathscr{X}, u(t) \in \mathscr{U} \qquad t \in [0, H_p], \tag{11c}$$

$$x(0) \in \mathscr{X}_0, x(H_p) \in \mathscr{X}_{H_p} \tag{11d}$$

where H_p represents the final time of the prediction horizon, $x(t)$ the prediction for the states at a time t, and $u(t)$ the proposed value for the manipulated variables at a time t of the prediction horizon. Function $J(.)$ represents the cost of reaching a certain objective (e.g. the error in following a reference) in the prediction horizon, while the function $J_t(.)$ represents a cost to be evaluated only at the end of the prediction horizon. The prediction is represented in (11b), with the function f_{nl} being the differential equation that represents this model. In (11c) restrictions on states and variables manipulated during the prediction horizon are represented, while in (11d) the initialization of states with measurements (represented by the set $\mathscr{X}_0$) is presented, and terminal restrictions are presented for states and manipulated variables,$x(H_p)$ and u, respectively.

The model used in the prediction can be of several forms, being decisive in the type of control problem and in the algorithm to be used to solve such problem. In the case of nonlinear models, as observed in the works presented in the previous section, the optimization problem to be solved by MPC is a Nonlinear Programming (NLP). Due to the discrete nature of the controllers implementation, it is necessary to partition the controller's prediction horizon and assume some behavior for the controlled variable during the partitions. It is common to assume that the manipulated variables are constant in each partition (Zero-Order Hold). For notation of the discrete MPC, consider the equivalente presented by Equation (12).

$$u(t) = u(k) \quad \text{for} \quad t \in [t_k, t_{k+1}), \qquad k \in [0, 1, ..., H_p - 1]. \tag{12}$$

Where t_s is the duration of each partition (or sampling time), t_k is the time at the beginning of the partition k given by expression $t_k = t_s k$, and k is a non-negative integer. The discretization of the dynamic model of the process involves the calculation of the integral of the equation (11b) is more complex and can be performed in several ways (eg Euler, Runge-Kutta , etc). With this, we have that the optimization problem to be solved in a Nonlinear MPC can be in the form described in (13):

$$\min_{u} \sum_{k=1}^{H_p} J_d(x(k), u(k)) + J_t(x_{H_p}) \tag{13a}$$

Subject to

$$x(k+1) = f_d(x(k), u(k)), \qquad k \in [0, ..., H_p - 1], \tag{13b}$$

$$x(k) \in \mathscr{X}, \qquad k \in [1, ..., H_p], \tag{13c}$$

$$u(k) \in \mathscr{U}, \qquad k \in [0, ..., H_p - 1], \tag{13d}$$

$$x_0 \in \mathscr{X}_0, x_{H_p} \in \mathscr{X}_{H_p}. \tag{13e}$$

Since $J_d(.)$ is a discrete equivalent of the cost $J(.)$, $f_d(.)$ is a discretization of the model given in Equation (11b). A reference on how to implement this type of controller can be found in Johansen (2011) and Kirches (2012).

Some works that use nonlinear MPC in solar thermal systems can be found in Torrico et al. (2010), which proposes a robust nonlinear predictive controller to consider important elements, such as transport delay, to keep the temperature of HTF constant throughout loop in a desalination plant; Camacho, Gallego, Escaño, et al. (2019a) performs a solar field control considering nonlinearities and discrete elements to change the plant's operating mode to maintain production objectives; and Vergara et al. (2016) which performs the control of large solar fields, considering problems such as the passage of clouds through a part of the field and the thermal imbalances that this causes.

One of the challenges to the implementation of predictive controllers that use nonlinear models is the calculation of predictions in solving the optimization problem which, depending on the complexity of the model, can have a high computational cost. This high cost can make the controller unable to calculate the control actions in a sampling period, which would make the real-time application unfeasible. Note that, in this case, the high computational cost is not associated with the complexity of the control problem itself, but with the numerical integration of the differential equation of the process model. A technique widely used to facilitate the calculation of these predictions in nonlinear predictive control problems is the *Multiple Shooting*, which will be described in the next section.

2.5.1 *Multiple Shooting*

The traditional implementation of the calculation of predictions in MPC is performed iteratively and sequentially, using for the calculation of x_{k+1} the previous values of states (x(k)) and manipulated variable (u(k)), as represented in the constraint (13b). Explaining the calculation of the predictions in this way, with x_0 being the initial conditions, we have that:

$$
\begin{aligned}
x(1) &= f_d(x_0, u_0), \\
x(2) &= f_d(x(1), u(1)), \\
&= f_d(f_d(x_0, u_0), u(1)), \\
x(3) &= f_d(x(2), u(2)), \\
&= f_d(f_d(f_d(x_0, u_0), u(1)), u(2)), \\
&\vdots \\
x(H_p) &= f_d(x(H_p-1), u(H_p-1)).
\end{aligned}
$$

Note that in this way the values of $x(k)$ obtained are always consistent with the predictions calculated up to the instant $k-1$ and with the proposed controls, which intuitively seems desirable, but introduces a series of strict restrictions in the optimization problem, which can hinder the convergence of the algorithm. Furthermore, the sequential nature of the calculation of these predictions prevents them from being obtained with parallel computation.

Multiple Shooting (BOCK; PLITT, 1984) is a technique that facilitates solving the optimization problem of MPC and simultaneously calculating the predictions of the process model, especially in nonlinear systems with ill-conditioned dynamics (*stiff*). For such, the values of the initial conditions of the states ($x^0(k)$) in the prediction horizon are defined as decision variables of the optimization problem. This increases the number of degrees of freedom of *solver*, which can facilitate the resolution and makes the value of the states at each instant independent of the process model, which is not desired. To reestablish the relationship between the initial condition value of the states and the process model, the constraint (13b) is replaced by the constraints (14b) and (14c), as shown below:

$$\min_{x^0,u} \sum_{k=1}^{H_p} J_d(x(k), u(k)) + J_t(x(H_p)) \tag{14a}$$

Subject to

$$f_d(x^0(k), u_k) - x(k+1) = 0, \qquad k \in [0, ..., H_p-1] \tag{14b}$$

$$x_k^0 = x_k, \qquad k \in [1, ..., H_p] \tag{14c}$$

$$x(k) \in \mathscr{X}, x^0(k) \in \mathscr{X}, \qquad k \in [1, ..., H_p] \tag{14d}$$

$$u(k) \in \mathscr{U}, \qquad k \in [0, ..., H_p-1] \tag{14e}$$

$$x_0 \in \mathscr{X}_0, x(0)^0 = x_0, x_{H_p} \in \mathscr{X}_{H_p}. \tag{14f}$$

Although problems (13) and (14) result in the same optimal control problem, the new formulation allows *solver* to have more freedom to solve this problem, converging faster.

Note that in this case, it is necessary to define the initial conditions at each point of the prediction horizon ($x^0(k), k \in [1, ..., H_p]$), and not only x_0. As the initial condition given to *solver* does not necessarily imply a feasible solution of (14), a discontinuity of predictions in the prediction horizon may occur in the initial steps of the problem resolution, as can be seen in Figure 13. Although the state trajectories in the figure appear to be continuous, these are discrete and were obtained with an integration step much smaller than the sampling time, resulting in lines that appear continuous. As the *solver* advances the iterations to solve the optimization problem, the constraint (14b) imposes the coherence of predictions, which can also be observed in Figure 13.

Figure 13 – Predictions and control actions in a predictive control problem with multiple shooting. The graph tp the left represents the beginning of the solution. The graph to the right represents the end of the solution.

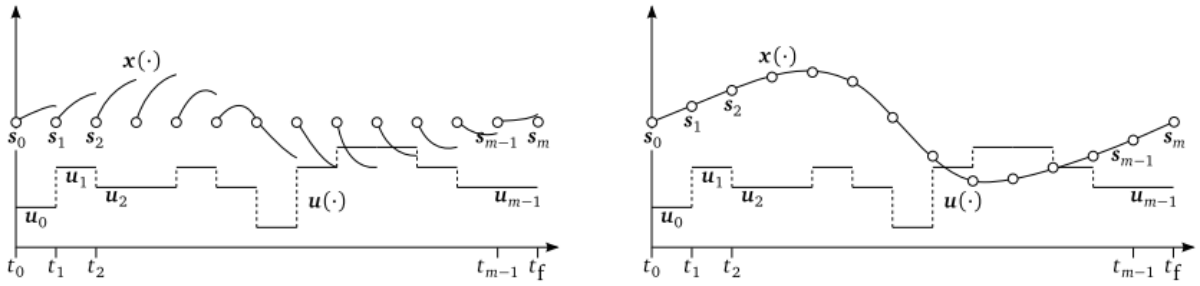

Source: Kirches (2012).

The benefits of using this approach are found in the generation of an optimization problem with a more sparse structure that can be explored by *solvers* of quadratic recursive programming, improving the performance in solving the problem (ANDERSSON, 2013). Furthermore, the convergence of *solver* in nonlinear problems is improved as the negative impact of a bad initial estimate is mitigated over the iterations (BOCK; PLITT, 1984). A comparison of the performance gain possible with the use of *multiple shooting* in solving predictive control problems can be found in the work of Hussein et al. (2019).

2.5.2 Practical Nonlinear Model Predictive Control (PNMPC)

The Practical Nonlinear Model Predictive Control (PNMPC) is a nonlinear MPC proposed by Plucenio et al. (2007) which is based on the linearization of the process model at each sampling time. The control action is obtained by the same methods used in linear MPCs, that is, by solving an Quadratic Programming (QP), which has fast and reliable solvers. In linear MPC, such as Dynamic Matrix Control (DMC) and Generalized

Predictive Control (GPC), the predictions are written as a linear function of the future control increments, expressed in Equation (15)

$$\widehat{Y} = \mathbf{G}.\Delta U + \mathscr{F}. \tag{15}$$

Where **G** is a matrix with coefficients that define the dynamic response of the model to the incremental inputs ΔU and $\mathscr{F}$ represents the response of the system given that no change on the input is provided, being called free response.

In PNMPC the predictions are computed as expressed in Equation (15), and the values of the dynamic response matrix ($\mathbf{G}_{pnmpc}$) and the free response ($\mathscr{F}_{pnmpc}$) are obtained from a nonlinear model f_{nl} at each sampling time. This procedure works in practice but does not guarantee finding the optimal solution for the nonlinear control problem (ANDRADE et al., 2013). In order to understand how to obtain $\mathbf{G}_{pnmpc}$ and $\mathscr{F}_{pnmpc}$, consider that at a given sampling time, the predictions obtained with the nonlinear model for the prediction horizon H_p can be written as a function of the past controlled variables' values $\overleftarrow{Y}$, manipulated variables' values $\overleftarrow{U}$ and some proposed future manipulated variables increments ΔU. In this case, the linearization of this $\mathscr{F}_{pnmpc}(\overleftarrow{Y}, \overleftarrow{U}, \Delta U)$ yelds Equation (16).

$$\widehat{Y} = \mathbf{G}_{pnmpc}.\Delta U + \mathscr{F}_{pnmpc} \cong f_{nl}(\overleftarrow{Y}, \overleftarrow{U}, \Delta U). \tag{16}$$

The free response for the PNMPC controller is obtained by evaluating the nonlinear model with no future movements for the manipulated variables, as seen on Equation (17).

$$\mathscr{F}_{pnmpc} = f_{nl}(\overleftarrow{Y}, \overleftarrow{U}, \Delta U = 0). \tag{17}$$

The dynamic matrix $\mathbf{G}_{pnmpc}$ is given by the jacobian of the nonlinear function, as expressed in Equation (18), with N_u manipulated variables and N_y controlled variables.

$$\mathbf{G}_{pnmpc} = \left.\frac{\partial \widehat{Y}}{\partial \Delta U}\right|_{U=U^0} = \begin{bmatrix} \frac{\partial \hat{Y}_1}{\partial \Delta U_1} & \frac{\partial \hat{Y}_1}{\partial \Delta U_2} & \cdots & \frac{\partial \hat{Y}_1}{\partial \Delta U_{N_u}} \\ \frac{\partial \hat{Y}_2}{\partial \Delta U_1} & \frac{\partial \hat{Y}_2}{\partial \Delta U_2} & \cdots & \frac{\partial \hat{Y}_2}{\partial \Delta U_{N_u}} \\ \vdots & \vdots & \ddots & \vdots \\ \frac{\partial \hat{Y}_{N_y}}{\partial \Delta U_1} & \frac{\partial \hat{Y}_{N_y}}{\partial \Delta U_2} & \cdots & \frac{\partial \hat{Y}_{N_y}}{\partial \Delta U_{N_u}} \end{bmatrix}. \tag{18}$$

Each term $\frac{\partial \widehat{Y}_j}{\partial \Delta U_i}$ is a matrix of the partial derivateives of the predictions of the controlled variables $\widehat{y}_i$ over the prediction horizon H_p with regard to the manipulated variable u over the control horizon H_c, as expressed in Equation (19).

$$\frac{\partial \widehat{Y}_j}{\partial \Delta U_i} = \begin{bmatrix} \frac{\partial \hat{y}_j(k+1)}{\partial \Delta u_i(k)} & 0 & \cdots & 0 \\ \frac{\partial \hat{y}_j(k+2)}{\partial \Delta u_i(k)} & \frac{\partial \hat{y}_j(k+2)}{\partial \Delta u_i(k+1)} & \cdots & 0 \\ \vdots & \vdots & \ddots & \vdots \\ \frac{\partial \hat{y}_j(t+H_p)}{\partial \Delta u_i(k)} & \frac{\partial \hat{y}_j(t+H_p)}{\partial \Delta u_i(k+1)} & \cdots & \frac{\partial \hat{y}_j(t+H_p)}{\partial \Delta u_i(k+H_c-1)} \end{bmatrix}. \tag{19}$$

Notice that Equation (19) has derivatives with respect to the manipulated variables over every instant of the control horizon, which requires $H_p \times H_c$ derivative computations. The zero values above the main diagonal occur due to causailty, as if not zero these would represent an output that depends on future control movements. Yang (2016) performed comparisons on variants of ways to build the matrix $\frac{\partial \widehat{Y}_j}{\partial \Delta U_i}$ and concludes that for many cases, it may not be necessary to compute all these computations. This thesis uses the simplest of these proposals, which only requires H_p evaluations of the partial derivative for each pair of manipulated and controlled variable. This structure is presented in Equation (20), where it is noticeable that the elements are repeated in the direction of the main diagonal.

$$\frac{\partial \widehat{Y}_j}{\partial \Delta U_i} = \begin{bmatrix} \frac{\partial \hat{y}_j(k+1)}{\partial \Delta u_i(k)} & 0 & \cdots & 0 \\ \frac{\partial \hat{y}_j(k+2)}{\partial \Delta u_i(k)} & \frac{\partial \hat{y}_j(k+1)}{\partial \Delta u_i(k)} & \cdots & 0 \\ \vdots & \vdots & \ddots & \vdots \\ \frac{\partial \hat{y}_j(t+H_p)}{\partial \Delta u_i(k)} & \frac{\partial \hat{y}_j(t+H_p-1)}{\partial \Delta u_i(k+1)} & \cdots & \frac{\partial \hat{y}_j(k+1)}{\partial \Delta u_i(k)} \end{bmatrix}. \tag{20}$$

The derivatives needed for the Jacobian ($\mathbf{G}_{pnmpc}$) can be obtained analytically, but given the diversity and complexity of nonlinear models, Plucenio et al. (2007) suggests using numerical derivatives and proposes an algorithm for calculating $\mathscr{F}_{pnmpc}$ and $\mathbf{G}_{pnmpc}$, which consists of evaluating the nonlinear model for some small step value ϵ_i for each manipulated variable. Plucenio et al. (2007) suggests ϵ_i to be 1% of the previously applied manipulated variable value, as presented in Algorithm 1.

Algorithm 1 Computation of $\mathscr{F}_{pnmpc}$ and $\mathbf{G}_{pnmpc}$

Considering:

- $\mathbf{G}_{pnmpc}{}^{i}$ is the ith column of the matrix $\mathbf{G}_{pnmpc}$.
- $\bar{Y}^{i}$ is the output of the nonlinear model when ϵ_i is applied in one position of the incrmental ΔU.
- $\Delta \bar{U}_i$ is an array of zeroes except at the position respective to the first instant of the prediction horizon for input i, where it has ϵ_i as its value.

Do:
$\mathscr{F}_{pnmpc} = f_{nl}(\overleftarrow{Y}, \overleftarrow{U}, \Delta U{=}0)$
for *i from* 1 *to* N_u **do**
  for *k from* 1 *to* H_p **do**
    Compute $\Delta \bar{U}_i$
    $\bar{Y}^{i} = f_{nl}(\overleftarrow{Y}, \overleftarrow{U}, \Delta \bar{U}_i)$
    $\mathbf{G}_{pnmpc}{}^{i} = \frac{\bar{Y}^{i} - \mathscr{F}_{pnmpc}}{\epsilon_i}$

Linear MPC algorithms such as DMC and GPC use mechanisms to correct the

predictions of the process models at each sampling period, with the goal of achieving zero prediction error in steady state. For PNMPC, an explicit version of the correction made in GPC is used, adding to the free response at each point of the prediction horizon the integral of the filtered prediction error e_{pnmpc}. The prediciton error is given by Equation (21) while the filter is presented in Equation (22). As the computation of the predictions is recursive, the corrected prediction of one instant is used to compute the prediction of the next time step.

$$e_{pnmpc} = Y^0 - \widehat{Y}(0) \tag{21}$$

$\widehat{Y}(0)$ is the prediction for the controlled variables at the current time made at the previous sampling time of the controller and Y^0 is the current measurement of the controlled variables.

$$\eta(k) = \eta(k-1) \cdot (1 + f_d) - f_d \cdot \eta(k-2) + e_{pnmpc} \cdot K_i \tag{22}$$

Plucenio et al. (2007) proposes a way to select the filter coefficients by selecting the desired dynamics for the filter as well as an example of the impact of this filter on the response of the control system in the presence of noise is presented. In this work, the coefficients $f_d = 0$ and $K_i = 1$ were used.

2.6 HYBRID PREDICTIVE CONTROL

In addition to continuous variables, it is also interesting to use binary variables in solar field models to represent aspects such as pump activation, valve closure, mirror blur, activation of auxiliary heat sources, etc. Models that incorporate both analog and binary (or integer) variables are called hybrids, and can be used in hybrid predictive controllers, as in Araújo Elias et al. (2019). These formulations result in Mixed-Integer Nonlinear Programming (MINLP) problems, whose solution has a significant computational cost. These types of problems arise in power systems, and in particular solar, as shown by Camacho, Ramirez, et al. (2010). In Camacho, Gallego, Escaño, et al. (2019b), a hybrid controller is used to decide the operation mode of a solar cooling plant, while in Vasallo and Bravo (2016) this type of controller is used to define the production order in a solar plant. Proposing a formulation that does not involve solving a mixed-integer problem, Prada et al. (2004) investigates how to define the production order in a batch process.

There are some types of models that can be used to represent hybrid systems in MPC, such as models Piecewise Affine (PWA), State Machines and Mixed Logical Dynamical (MLD), *Mixed Logical Dynamical*. The following section will explore the models MLD and present some works that use them in predictive controllers as this framework will be used in this thesis.

2.6.1 Mixed Logical-Dynamic Systems (MLD)

Many dynamic systems with logical or integer variables have behaviors governed by logical expressions, such as a solar field that, when it is shaded, must have the flow of HTF stopped to avoid heat loss to the environment. The incorporation of these logic expressions is commonly performed through hierarchical control schemes, in which decisions involving boolean logic are performed in high-level hierarchical structures, while low-level controllers deal only with continuous variables. In the case of processes in which logical variables are deeply embedded in the dynamics of the process, hierarchical structures become inadequate. In view of this type of problem, Bemporad and Morari (1999) proposed a *framework* for the modeling and control of linear systems with logical variables, being called *Mixed Logical Dynamic* (MLD).

In MLD, the logical expressions are rewritten as equivalent constraints in the optimization problem, making it possible to adapt different types of expressions. The dynamic models built with this methodology incorporate continuous (x_c) and binary (x_b) manipulated variables continuous (u_c) and binary (u_b) and continuous (y_c) and binary (y_d). Binary (δ) and continuous (z) auxiliary variables are also used to construct the constraints. The general form of the models MLD is presented in the system of equations (23).

$$\begin{cases} x(k+1) & = Ax(k) + B_1 u(k) + B_2 \delta(k) + B_3 z(k), \\ y(k) & = Cx(k) + D_1 u(k) + D_2 \delta(k) + D_3 z(k), \\ E_2 \delta(k) + E_3 z(k) & \leq E_1 u(k) + E_4 x(k) + E_5. \end{cases} \tag{23}$$

Being

$$x = \begin{bmatrix} x_c \\ x_b \end{bmatrix}, y = \begin{bmatrix} y_c \\ y_b \end{bmatrix}, u = \begin{bmatrix} u_c \\ u_b \end{bmatrix}.$$

and the matrices $A, B_1, B_2, B_3, C, D_1, D_2, D_3, E_1, E_2, E_3, E_4$ and E_5 are the model parameters.

Many works use MLD for the formulation of hybrid controllers, such as Sun et al. (2019), which investigates the application of hybrid predictive control in an intelligent vehicle, or Liu et al. (2020), which implements a predictive control of a Buck converter, or even HanBing et al. (2019), which propose a vibration control in a bridge. In the context of renewable energies, the works of Elias et al. (2018) and Araújo Elias et al. (2019) present formulations of MPC hybrid with MLD in order to avoid the overheating of HTF of a solar field of parabolic collectors.

2.7 ADAPTATIVE NEURO-FUZZY INFERENCE SYSTEM

A Neuro-Fuzzy system is a form of Artificial Intelligence (AI) that combines the advantages of Fuzzy Logic (FL) and Artificial Neural Network (ANN). The most notable

is the Adaptative Neuro-Fuzzy Inference System (ANFIS) proposed by (JANG, 1993). ANFIS uses FL to represent knowledge in an interpretable form based on rules whith linguistic labels of human language. It has the capability to construct an input-output mapping based on human knowledge in the form of fuzzy *if-then* rules. The association with ANN makes the parametrization of the fuzzy rules incorporated into the learning algorithm of the ANN. Once the FIS is obtained after completing the ANFIS training, it is also possible to add rules, making this kind of technique also suitable to adaptive setups.

The next sections will present some basic pertinent concepts of Fuzzy Inference System (FIS) and ANN used in this thesis. Then, the ANFIS structure will be presented in more detail.

2.7.1 Fuzzy Inference System

Fuzzy Inference Systems are computational models used for mapping a given input-output set using the theory of fuzzy sets, concepts of fuzzy logic and IF-THEN rules. The fuzzy set theory and fuzzy logic provide a mathematical basis for the modelling the imprecise nature of real world systems (OLIVEIRA JUNIOR et al., 2007)

Fuzzy Sets

The Fuzzy Sets theory is an extension of the classical sets theory that was formalized by Zadeh (1965) with the goal of building a mathematical basis for modelling imprecise or approximate information. In classical set theory, the pertinence of an element to a given set is taken as true or false. That is, given a set A in an universe U, one can represent the relevance of elements to the set by some function $f(x)$:

$$f(x) = \begin{cases} 1, \text{ if and only if } x \in U, \\ 0, \text{ if and only if } x \notin U. \end{cases}$$

This binary definition is extended by Zadeh with the proposal of more comprehensive membership levels, which assume intermediate values in the range [0, 1]. That is, given a fuzzy set B in a universe U, one can represent the pertinence of elements to this set by a characteristic function:

$$\mu_B(x) : U \rightarrow [0,1].$$

where $\mu(x)_B$ is a function that will indicate the degree of membership of x in B. Several different types of functions can be employed as pertinence functions and the most common are trapezoidal, triangular and, in the case of this thesis a generalized bell function:

$$\mu_B(x) = \frac{1}{1 + \left[\left(\frac{x-c}{a}\right)\right]^{2b}}.$$

where a, b and c are parameters that determine the shape of the function, as exemplified by Figure 14. Notice that for this type of symmetrical function, input values near c have the greatest pertinence, while values lower than $c-a$ have pertinences of less than 50%.

Figure 14 – Representation of the generalized bell pertinence function.

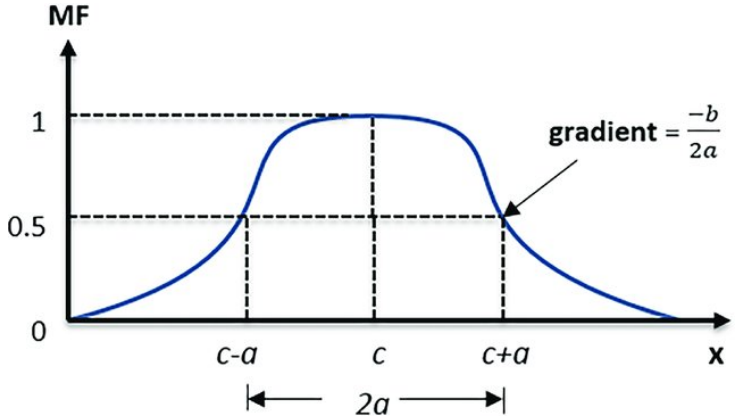

Source: Hossain et al. (2018).

In order to illustrate the pertinence functions, consider the issue of classifiying human body height as average or not. As this concept is very subjective, it is an ideal case for representig fuzzy modelling concepts. Considering the use of the generalized bell pertinence function in this case, one can define that an average height is around $1.7m$, thus we have $c = 1.7m$. In order to determine the parameter a, one can think of values for height that are considered short or tall (thus not average) by more than 50% of people. Considering that most people would find an height of $1.9m$ high, it is possible to obtain: $c-a = 1.9m$, thus $a = 1.7-1.9 = -0.2m$. The value of b can be chosen as to make this transition from average to tall more intense or smooth. Let $b = 1$, thus the membership function for this example ($\mu_{avg}(x)$) is defined as:

$$\mu_{avg}(x) = \frac{1}{1+\left[\left(\frac{x-1.7}{-0.2}\right)\right]^2}. \tag{24}$$

Fuzzy Rules and Takagi-Sugeno Inference Models

A fuzzy rule is a conditional statement given by IF-THEN statements. These are the rules used to make inferences in fuzzy logic, deciding the value of an output variable based on the pertinence values of input variables. The parameters presented in the IF statement are referred to as *antecedents*, while the THEN statement parameters are called *consequent*. As an example of a fuzzy rule, consider the membership function for human height of the previous example ($\mu_{avg}(x)$). It is possible to formulate the following

rule for deciding if a human can ride on an amusement park atraction:

$$\texttt{IF}\ x\ \texttt{is}\ \text{average},$$
$$\texttt{THEN}\ \text{x can ride}$$

The example shows a simple case, but the IF statements can contain multiple conditions, connected by AND and OR connectors. The rules of a fuzzy model can be shaped in numerous ways through expert knowledge of a process in order to replicate some input-optiput relationship, through Fuzzy Inference System (FIS). The literature presents some structures for these inference systems and in the case of this thesis, Takagi-Sugeno models (TAKAGI; SUGENO, 1985) are used. This type of FIS uses rules of the following form:

$$\texttt{IF}\ x_1\ \texttt{is}\ F_1\ \texttt{and}\ x_2\ \texttt{is}\ F_2\ \texttt{and}\ x_i\ \texttt{is}\ F_i\,,$$
$$\texttt{THEN}: f_{TS}(x) = g_0 + g_1 x_1 + \cdots + g_i x_i.$$

where $g_i \in \Re$ are consequent parameters, x_i are the inputs, f_{TS} the output respectively for each rule and F_i represents the fuzzy sets defined by some membership function. The parameters of the memebership functions that define F_i are the antecedent parameters. Notiece that the Takagi-Sugeno model has a polinomial to describe the outputs of the rule, thus having a crisp (i.e. not fuzzy) output.

2.7.2 Neuro-Fuzzy Networks

The term Neuro-Fuzzy Networks refers to the combination of Artificial Neural Network (ANN) with Fuzzy Inference System (FIS). These systems incorporate the techniques of machine learning for ANN with the Fuzzy capabilites to represent complex patterns and consist of an ANN where the neurons are composed of Fuzzy membership functions and rules. In the Neuro-Fuzzy approach, a supervised training phase is performed with reference input/output pairs in order to determine the *antecedent* and *consequent* parameters of the pertinence functions. The rules generated from the data can also be optimized using the expert's knowledge (JANG; SUN, 1995).

This type of network can be trained by online and offline learning. In online learning, the network changes dynamically as the data is presented, so that when more data is provided to the net it does not need to be retrained on the previously presented data. This thesis will only use offline training, in which there is no updating of the network parameters after training. The next section describes the type of neuro-fuzzy network that is predominant in the literature and that is used in this thesis, which is the Adaptative Neuro-Fuzzy Inference System (ANFIS).

2.7.3 ANFIS general structure

Adaptative Neuro-Fuzzy Inference System (ANFIS) is a type of neuro-fuzzy network proposed by Jang (1993) which is considered to be a universal estimator (JANG; SUN; MIZUTANI, 1997). It is composed by five layers of neurons, with two layers of Takagi-Sugeno inference models. Each layer of the ANFIS has a particular structure, with some described by a specific function, such as product or sum. The general structure of ANFIS is represented in Figure 15, and described as follows.

Figure 15 – Representation of the Adaptative Neuro-Fuzzy Inference System.

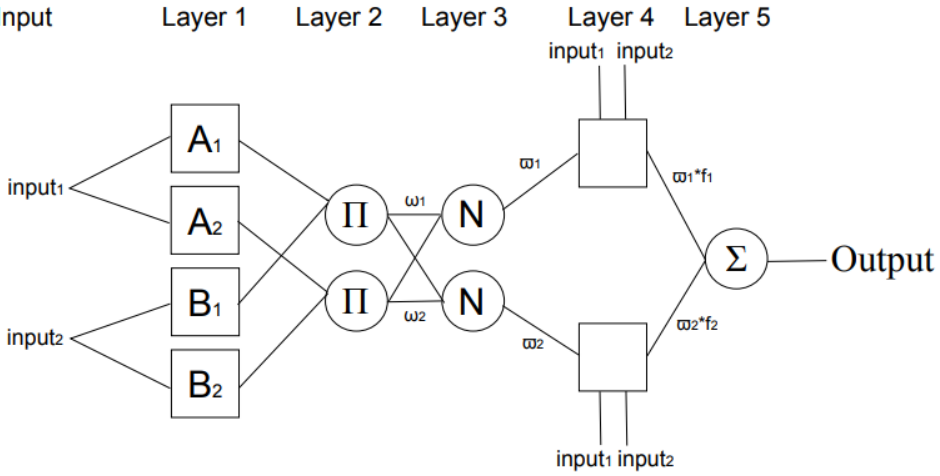

Source: Jang (1993).

- The first layer is composed of adaptive neurons, each one representing a fuzzy membership function for each input. In the case of this thesis, the generalized bell pertinence function.
- The second layer is composed of neurons with the product operator and its output is the product of all input signals. This represents the firing strengths for the fuzzy rules.
- The third layer is the normalization layer, its output is the normalized weighted sum of all input signals divided by the total firing strength.
- The fourth layer represents the consequent part of the inference system, where each neuron is of the adaptive type and implements the rules of the Takagi-Sugeno Model. The output of each neuron is obtained by evaluating the polynomial of the rules with the original inputs of the network multiplied by the normalization weight given by the previous layer.
- The fifth layer computes a sum of all input signals.

This structure, coupled with the learning algorithms of ANN, allows for the reproduction of complex input/output relationships. For the adjustment of the precedent parameters, Jang (1993) proposes backpropagation technique for the antecedents and least-squares for the consequent paramters. For a comprehensive description of ANFIS architecture, refer to the original papers Jang (1993) and Jang, Sun, and Mizutani (1997) or even the Master's thesis of Salazar (2020).

Despite being the first proposed neuro-fuzzy network found in the literature, there is recent research that attributes good results for ANFIS. The work of William Chicaiza Salazar et al. (2022) uses ANFIS to reproduce the behaviour of a absorption chiller high temperature generator, in such a way that allows for constant updating of the model, as a digital twin. J. M. Escaño et al. (2021) uses the neuro-fuzzy structure to estimate temperatures on a PTC field and Suhail et al. (2021) uses ANFIS as a controller for energy management of a plug-in hybrid electric vehicle.

FINAL REMARKS

This chapter presented a review of concepts relevant to this thesis. The contributions already made in this doctorate will be presented on the following chapters. These deal with optical modelling of a fresnel collector, predictive control of a solar field using the focus of the collectors as a manipulated variable and the potential uncertainties introduced by this manipulated variable, and finally two proposals for computing the mirror configuration for implementing the defocus proposed by the controllers.

3 CONTRIBUTIONS: MODEL PREDICTIVE CONTROL OF SOLAR FIELDS WITH DEFOCUSING

This chapter will present some of the contributions to model predictive control of solar fields. The proposal presented is for a hybrid predictive controller for HTF overheating prevention. The results of the work presented in this section were presented at the Solar World Congress 2019 and can be found at Brandão, Costa Mendes, Elias, et al. (2019). The main contributions of this chapter are:

- Development of an Hybrid Model Predictive Control strategy for CSP control with defocusing;
- Comparison of three proposals of Hybrid Model Predictive Control for CSP control with defocusing.

3.1 PREVENTION OF OVERHEATING IN SOLAR FIELDS WITH HYBRID MPC

This work focuses on the control of a solar collector field, which is composed of several parallel collector loops. A solar collector loop is composed of several solar energy collectors connected in serial configuration. Each collector is composed of a reflector that focuses the sun irradiation on an absorber tube. Inside the absorber tube, a Heat Transfer Fluid flows through the collector loop and recieves the thermal energy from the absorber tube. The amount of energy that the HTF has at the output of the loop is directly related to the amount of solar irradiation at the reflectors, which is both the main source of energy for the process and its main disturbance, and the degree of focus of the reflector. Typical control structures only manipulate the HTF flow as it changes the amount of energy absorbed per unit of time, but the defocusing of the reflector mirrors introduces a degree of freedom to the control structure and allows for faster lowering of the HTF temperature.

The control strategy applied to this process must be capable of maintaining the process under operational constraints, such as the maximum temperature allowed for the HTF, while maintaining the power generation (SÁNCHEZ et al., 2018). This type of process has very few degrees of freedom for the control actions as the HTF flow is typically the only manipulated variable and the collectors are only defocused for safety concerns. In a previous work, Araújo Elias et al. (2019) proposed two defocusing strategies in order to keep the HTF temperature under the operational constraints while maintaining the desired energy output: on/off and partial defocusing of the collectors. This work aims integrating both defocusing strategies in a centralized Nonlinear Model Predictive Control (NMPC) framework in order to obtain the best aspects from both previous controllers.

3.1.1 Proposed formulation for the controller

The proposed hybrid control structure aims to manipulate the HTF flow within its operational range to achieve the reference tracking objective. The controller should also defocus the solar collectors when the maximum HTF temperature is to be reached in a predictable future horizon while considering the future reference trajectory for the HTF temperature and the disturbances of ambient temperature, irradiation, and inlet temperature. These control objectives are accomplished using Practical Nonlinear Model Predictive Control (PNMPC) and are expressed on Equation (25).

$$J = J_1 + J_2 + J_3. \tag{25}$$

The terms J_1, J_2 and J_3 represent three conflicting goals of the controller: Tracking a reference for the solar field output temperature, given by Equation (26a); Minimizing the motion of the manipulated variables, given by Equation (26b); and Maximizing the HTF volume flow rate and focus value to indirectly maximize the process energy output, given by Equation (26c).

$$J_1 = \sum_{k=1}^{H_p} (T_{out,field}(k) - T_{ref}(k))^2 Q_T, \tag{26a}$$

$$J_2 = \sum_{k=1}^{H_c} \sum_{i=1}^{n_l} (\Delta v_i(k))^2 R_v + \sum_{k=1}^{H_c} \sum_{j=1}^{n_c} \sum_{i=1}^{n_l} (\Delta \varphi_{i,j}(k))^2 R_\varphi, \tag{26b}$$

$$J_3 = -\sum_{k=1}^{H_c} \sum_{i=1}^{n_l} (v_i(k))^2 Q_v - \sum_{k=1}^{H_c} \sum_{j=1}^{n_c} \sum_{i=1}^{n_l} (\varphi_{i,j}(k))^2 Q_\varphi, \tag{26c}$$

With:

$$\Delta v_i(k) = v_i(k) - v_i(k-1), \qquad k \in [1, \ldots, H_c],$$
$$\Delta \varphi_{i,j}(k) = \varphi_{i,j}(k) - \varphi_{i,j}(k-1), \qquad k \in [1, \ldots, H_c].$$

$T_{out,field}$ and T_{ref} are the predicted and reference outlet temperatures of the solar field for the prediction horizon, Δv_i the changes on the flow of each loop of the solar field for the control horizon of this variable,$\varphi_{i,j}$ the focus variable for all collectors of each loop of the field for the control horizon of this variable and $\Delta \varphi_{i,j}$ the changes on $\varphi_{i,j}$ for the same control horizon. The square matrices Q_T, Q_v, Q_φ, R_φ ans R_v are weights of appropriate size. The prediction horizon is given by H_p while the control horizon is given by H_c. The number of loops and collectors at each loop are given by n_l and n_c respectively.

The two control strategies that are combined in this thesis will be called On/Off, in which the controller must completely defocus one or more manifolds in the loop if the outlet temperature of any collector in this loop is above the upper limit in the controller's prediction horizon; and Partial, in which the controller combines flow manipulation and partial collector defocusing in order to achieve the control objectives with reduced control effort when compared to the On/Off case. The reduced control effort is desirable as it provides longer life for actuators such as valves and pumps.

In order to implement the proposed integrated strategy, it is necessary to introduce the binary variable $\Lambda_{i,j}$ which indicates if a collector should be focused ($\Lambda_{i,j}=1$) or completely defocused ($\Lambda_{i,j}=0$). The constraints presented in Equation (28) and (29) determine the possible values of the focus $\varphi_{i,j}$ and its change rate $\Delta\varphi_{i,j}$.

$$0 \leq \varphi_{i,j}(t+k) \leq 10\Lambda_{i,j}. \qquad i \in [1, n_l], \quad j \in [1, n_c], \quad k \in [1, H_c], \tag{28}$$

$$-\Lambda_{i,j}(t+k)-10(1-\Lambda_{i,j}(t+k)) < \Delta\varphi_{i,j}(t+k) < \Lambda_{i,j}(t+k)+10(1-\Lambda_{i,j}(t+k)),$$
$$i \in [1, n_l], \quad j \in [1, n_c], \quad k \in [1, H_c]. \tag{29}$$

If the collector should be in focus ($\Lambda_{i,j}=1$), the focus value will have a full range between 0% focus ($\varphi_{i,j}=0$) and 100% focus ($\varphi_{i,j}=10$) and the change in focus is limited to ± 10% ($-1 < \Delta\varphi_{i,j} < 1$), but if the collector is to be completely defocused ($\Lambda_{i,j}=0$), the focus value is forced to zero and the change in focus can vary from -100% to 100%, as it must be able to go from completely focused to completely defocused and vice versa.

As stated Araújo Elias et al. (2019), there are operational limits on the HTF flow rate (v_{MAX} and v_{MIN}) and in order to prevent the controller from manipulating the flow rate when the collector is defocused, the constraints presented in eqs. (30) and (31) are applied, which forces the applied flow rate to stay at the upper bound when the collector is defocused ($\Lambda_{i,j}=0$).

$$v_i(t+k) \leq v_{MAX}, \qquad i = 1..n_l, j = 1..n_c, k = 1..H_c, \tag{30}$$
$$v_i(t+k) \geq v_{MIN}\Lambda_{i,j}(t+k) + v_{MAX}(1-\Lambda_{i,j}), \quad i \in [1, n_l], \quad j \in [1, n_c], \quad k \in [1, H_c]. \tag{31}$$

To determine whether a collector should be defocused, the binary variable $\alpha_{i,j}$ is introduced to indicate whether, at a given period in the forecast horizon, the HTF temperature at collector *j* would exceed the maximum allowed temperature ($\alpha_{i,j}=0$) or not ($\alpha_{i,j}=1$). This condition is expressed in Equation (32):

$$\alpha_{i,j}(t+k-1) = 1 \leftrightarrow \hat{T}_{out_{i,j}}(t+k|t) \leq T_{max}, \qquad i \in [1, n_l], \quad j \in [1, n_c], \quad k \in [1, H_c]. \tag{32}$$

Where $\hat{T}_{out_{i,j}}$ is the prediction for the outlet temperature of collector j of loop *i*. This condition can be rewritten according to the inequalities presented in eqs. (33)

and (34) by considering that the flow rate is at the upper bound when the collector is defocused.

$$\alpha_i(t+k-1)\,\hat{T}_{out_{i,j}|v=v_{MAX}}(t+k|t)-T_{max},\leq 0 \quad i\in[1,n_l], \quad j\in[1,n_c], \quad k\in[1,H_c], \tag{33}$$

$$\hat{T}_{out_{i,j}|_v=v_{MAX}}(t+k|t)-(1-\alpha_{i,j}(t+k-1|t))\,T_{max}\geq 0, \quad i\in[1,n_l], \quad j\in[1,n_c], \quad k\in[1,H_c]. \tag{34}$$

The decision to completely defocus a collector ($\Lambda_{i,j}=0$) should be made if, at any instant in the prediction horizon, the predicted outlet temperature of the collector is above the upper limit of the HTF, as expressed in the inequalities in (35):

$$\begin{aligned} -\alpha_{i,j}(t)+\Lambda_{i,j}(t)&\leq 0,\\ -\alpha_{i,j}(t+1)+\Lambda_{i,j}(t)&\leq 0,\\ &\vdots\\ -\alpha_{i,j}(t+N_\alpha-1)+\Lambda_{i,j}(t)&\leq 0,\\ \alpha_{i,j}(t)+\alpha_{i,j}(t+1)+\ldots+\alpha_{i,j}(t+N_\alpha-1)-N_\alpha+1&\leq 0. \end{aligned} \tag{35}$$

All the controllers presented in this section were implemented in Yalmip, a Matlab toolbox for optimization and modelling. All optimization problems were solved using IBM's Cplex solver. Each of the tuning matrices of the objective function can be defined as a multiplication of a scalar by an identity matrix of appropriate size. These scalars are presentded in Table 1.

Table 1 – Tuning parameters of the controllers.

	Q_T	Q_v	Q_φ	R_v	R_φ
On/Off	1e-5	1e-3	0.1	1e2	1e-3
Partial	1e-5	1e-3	0.1	1	1e2
Hybrid	1e-5	5e-3	0.1	1e4	1.13

Simulation results

To evaluate the performance of the hybrid controller and compare it with the On/Off and partial defocusing controllers, three simulation scenarios were created:

- High irradiance scenario: irradiance profile for the morning of the day with high peak irradiance and some clouds;
- Pump failure scenario: An irradiance profile for the early afternoon without clouds. At two points in the simulation, a pump malfunction is simulated for loop 1 of the solar field and the flow rate is fixed. Between t=36 min and t=54 min the flow rate

is fixed at $8.10^{-3} m^3 s^{-1}$ and between $t = 132$ min and $t = 156$ min the flow rate in loop 2 was fixed at $12.10^{-3} m^3 s^{-1}$.

- Pump failure scenario with modeling error: Same as previous case, but considering a 10% error in the optical efficiency parameter.

The applied profiles for ambient temperature and irradiance are presented in Figures 16 and 17. To evaluate the simulated results, three performance indices were considered: amount of heat absorbed by the HTF, the integral of the squared error of reference tracking (ISE) for the solar field output temperature, and the calculation of the average runtime for the controllers. The results are presented in table 2.

Figure 16 – Ambient temperature used for all cases.

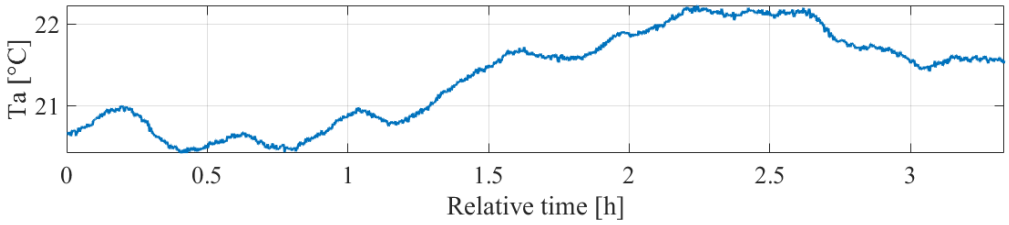

Source: The author.

Figure 17 – Irradiance profiles: (a) High irradiance; (b) Pump failure.

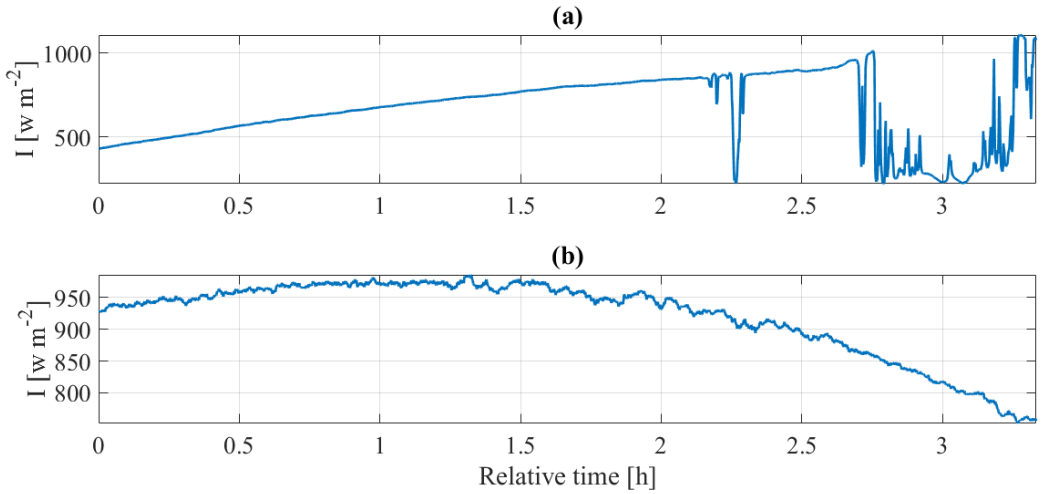

Source: The author.

The simulation results for the high irradiance scenario are shown in figures 18, 19 and 20. These figures show the output temperature of the entire field and the reference, the focus value for each collector, and the HTF flow rate for the two loops. Since the partial defocus controller kept the flow rates high when compared to the other controllers, the amount of thermal energy absorbed by the HTF is higher for this controller (see Table 2). The hybrid controller showed small changes in flow rate, which resulted in higher output HTF temperature variability and high ISE values. In this case, the hybrid controller presented less aggressive compared to the other MPC, which

Table 2 – Performance criteria for the simulated cases.

		On/Off	Partial	Hybrid
1 - High irradiance scenario	Heat [J]	3.8723e+09	4.6064e+09	3.5178e+09
	ISE	5.8366e+04	4.4523e+04	9.2163e+04
	Average time [s]	0.6728	0.0617	0.1367
2 - Nominal case with pump failure	Heat [J]	4.8853e+09	3.7994e+09	4.8700e+09
	ISE	3.5497e+04	4.3240e+04	3.7473e+04
	Average time [s]	0.7406	0.1178	0.0967
3 - Case with modelling errors and pump failure	Heat [J]	5.3123e+09	3.9164e+09	5.3761e+09
	ISE	4.6513e+04	3.9734e+04	4.3900e+04
	Average time [s]	0.6461	0.1128	0.1227

is desirable to reduce actuator wear, but may result in losses in energy absorption efficiency. The partial and hybrid controllers presented lower computation times when compared to the On/Off controller, because the optimization problem solved by this controller is more complex.

The results for the pump failure scenario are shown in figures 21, 22 and 23. As shown in Figure 23, it can be seen that the hybrid controller generates smaller deviations from the reference temperature when compared to the other MPCs during the pump failure. It is also notable that during both pump malfunctions, the hybrid controller was able to converge the proposed control action to the set flow rate values. This did not happen in the other controllers, with the On/Off (fig. 21) proposing different flow rate values during the first pump failure, and the partial controller (fig. 22) proposing different flow rate values during the second pump failure. It is important to note that the switching observed in the On/Off controller (fig. 21) is undesirable and results from the failure to obtain a feasible online solution to the optimization problem. The partial controller defocuses two collectors in both loops for almost the entire simulation, as can be seen in fig. 22. This is not desirable because, if there is no risk of overheating, defocusing the collector decreases the amount of energy that can be absorbed by the HTF, as can be seen by comparing the amounts of heat absorbed in table 2. For this simulation case, the computation times behaved similarly to the previous case, with the On/Off controller taking longer to compute the control actions.

The results of the pump failure scenario with model mismatch are presented in Figures 24, 25 and 26. In this simulation case, it can be seen that the partial focus controller (Fig. 25) uses lower flow values during the simulation, resulting in less energy being absorbed by the HTF (Tab. 2). The On/Off and hybrid controllers showed similar amounts of absorbed energy, but with much shorter computation times and worse reference tracking when compared to the partial focus controller. The defocusing frequency shown in the hybrid controller (Fig. 26) is considerably higher than that calculated by the On/Off controller (Fig.24), because the latter has constraints to avoid excessive switching.

Figure 18 – Simulation results for the nominal case with On/Off controller and high irradiance.

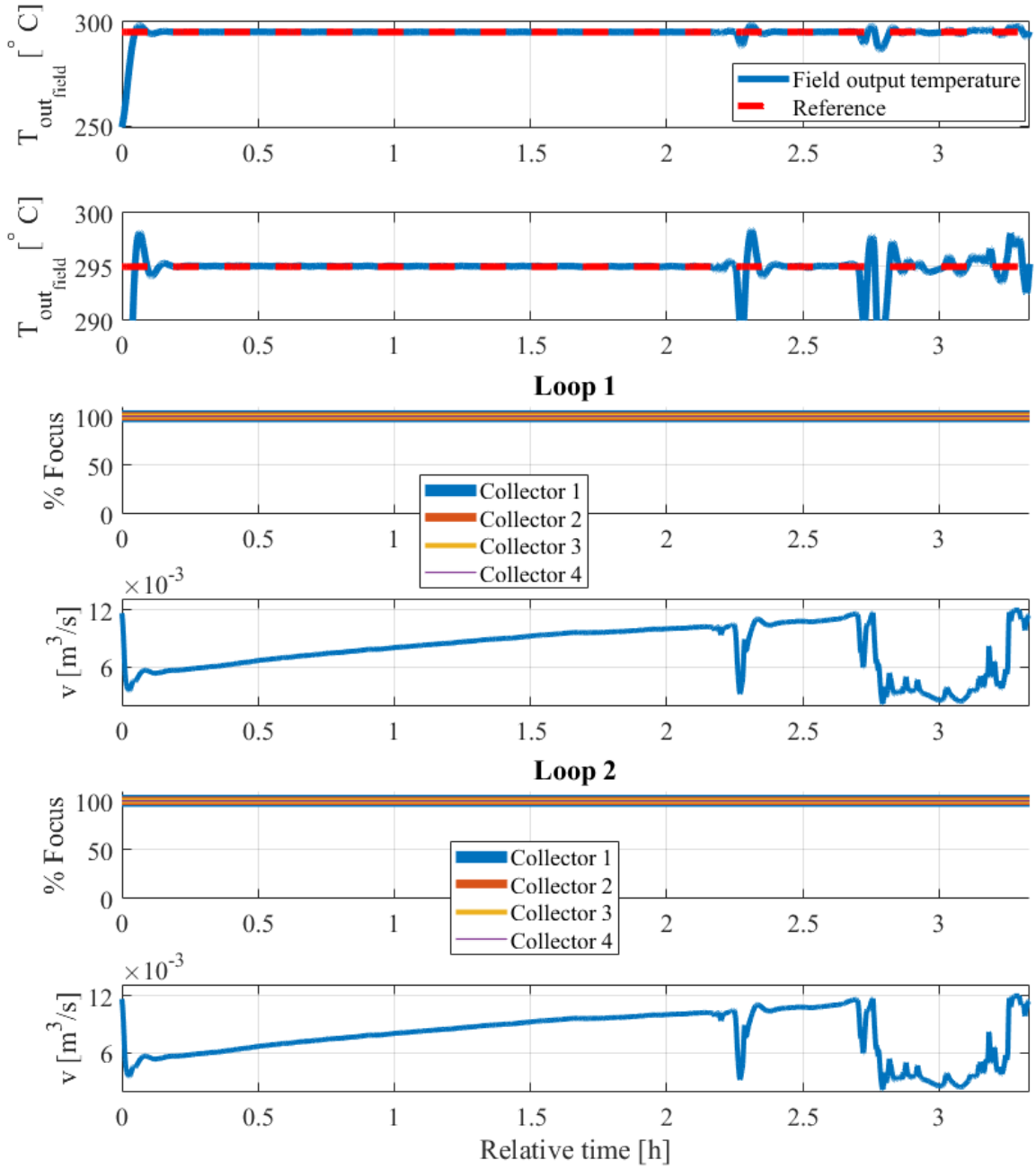

Source: The author.

Importantly, the behavior of the MPC controllers is highly dependent on the tuning parameters. The tuning of the controllers analyzed in this thesis was complex, especially for the hybrid controller, because its objective function contained several conflicting objectives with several variables that have very different ranges of possible values.

Figure 19 – Simulation results for the nominal case with partial focus controller and high irradiance.

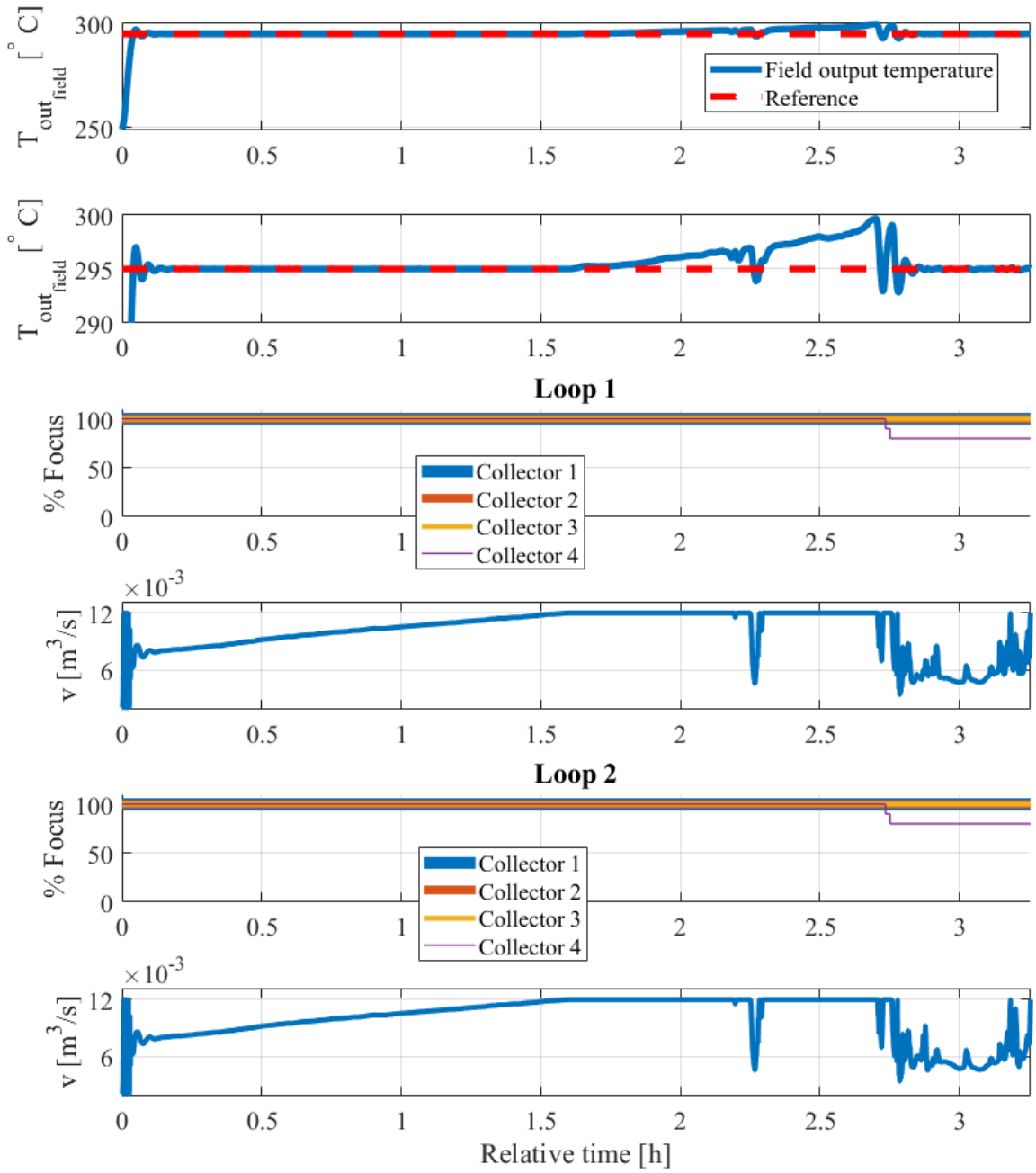

Source: The author.

Figure 20 – Simulation results for the nominal case with hybrid controller and high irradiance.

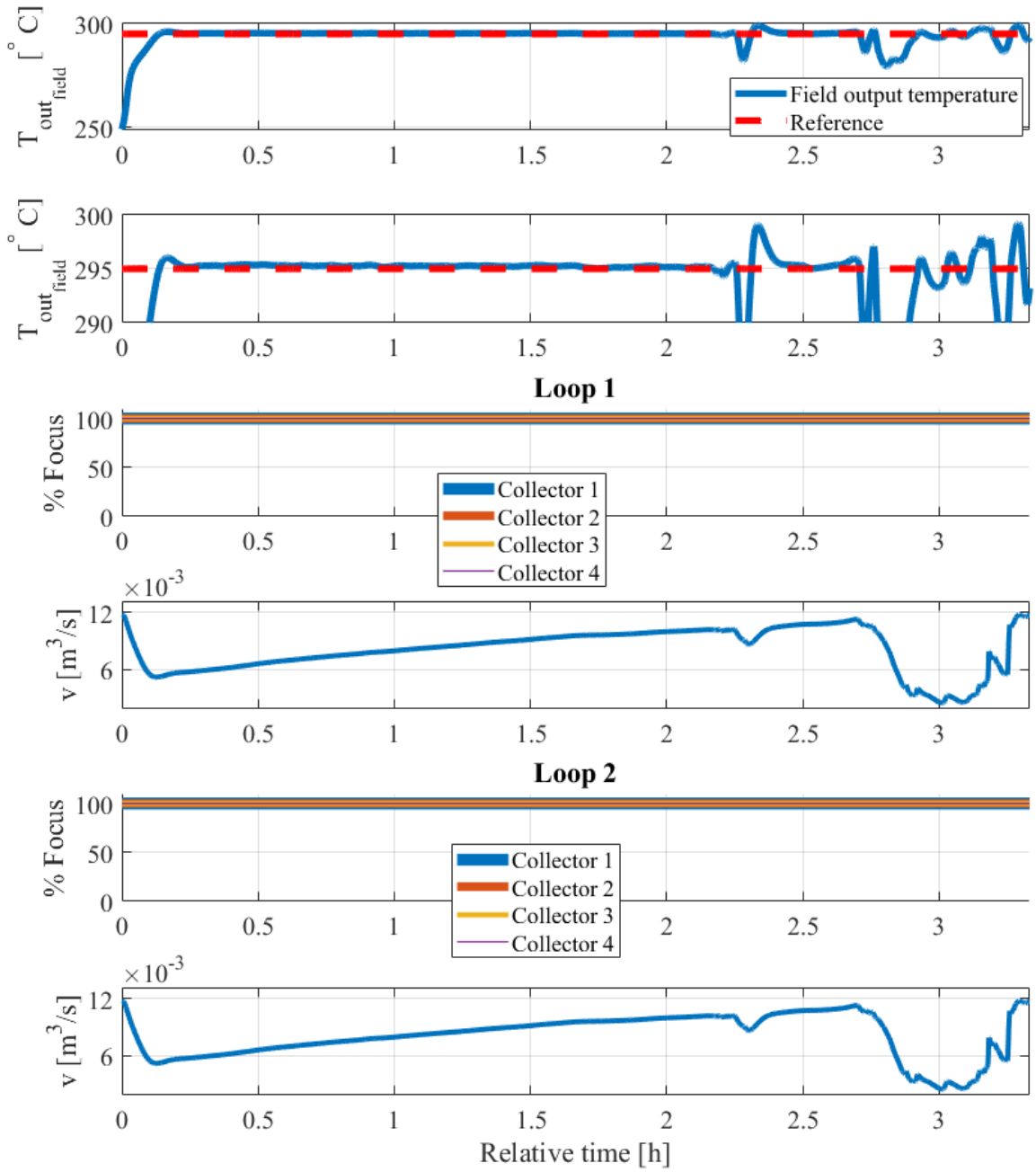

Source: The author.

Figure 21 – Simulation results for the nominal case with pump failure with On/Off controller and high irradiance.

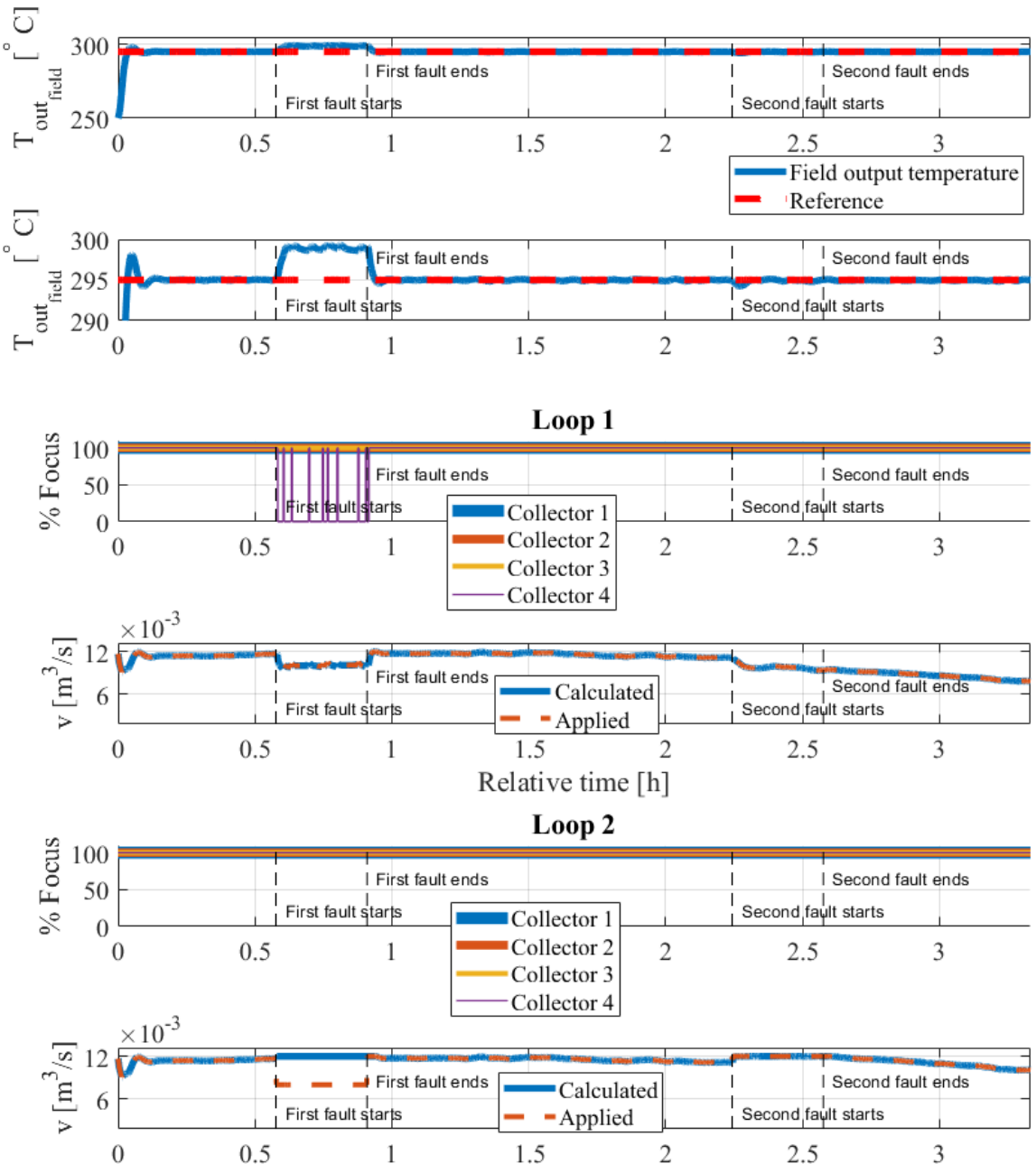

Source: The author.

Figure 22 – Simulation results for the nominal case with pump failure with partial focus controller and high irradiance.

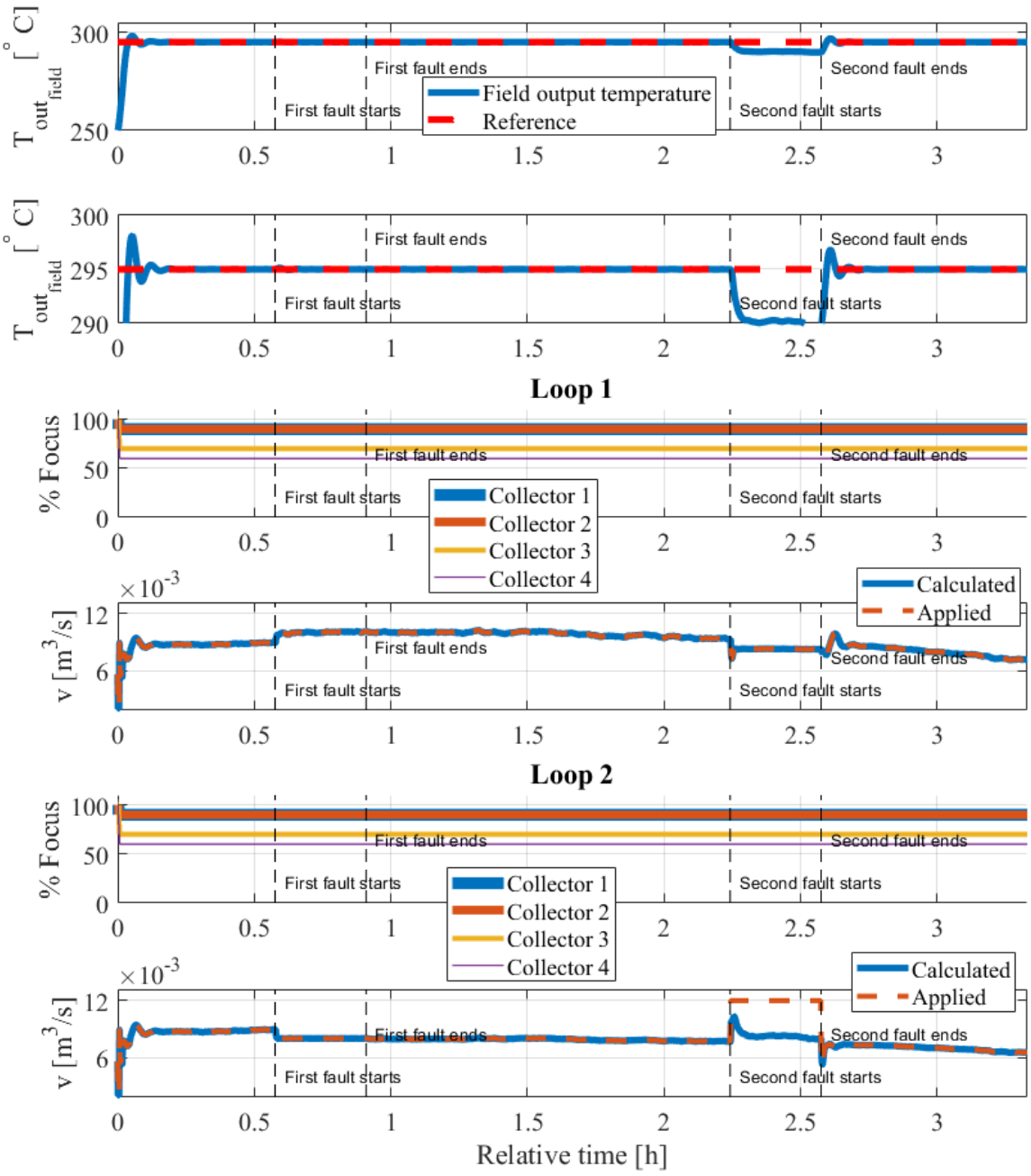

Source: The author.

Figure 23 – Simulation results for the nominal case with pump failure with hybrid controller and high irradiance.

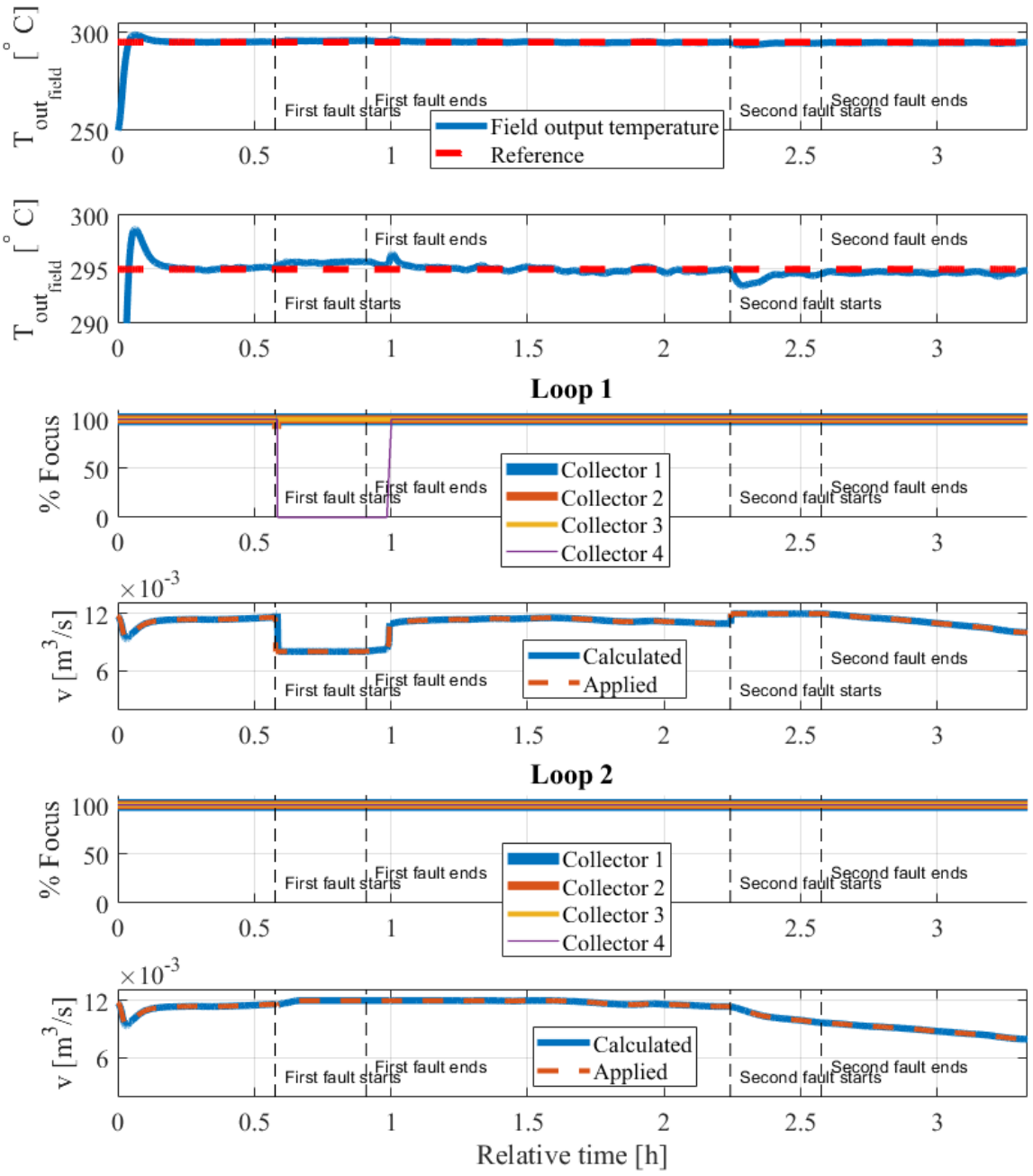

Source: The author.

Figure 24 – Simulation results for the case with parameter error, pump and on/off controller failure and high irradiance.

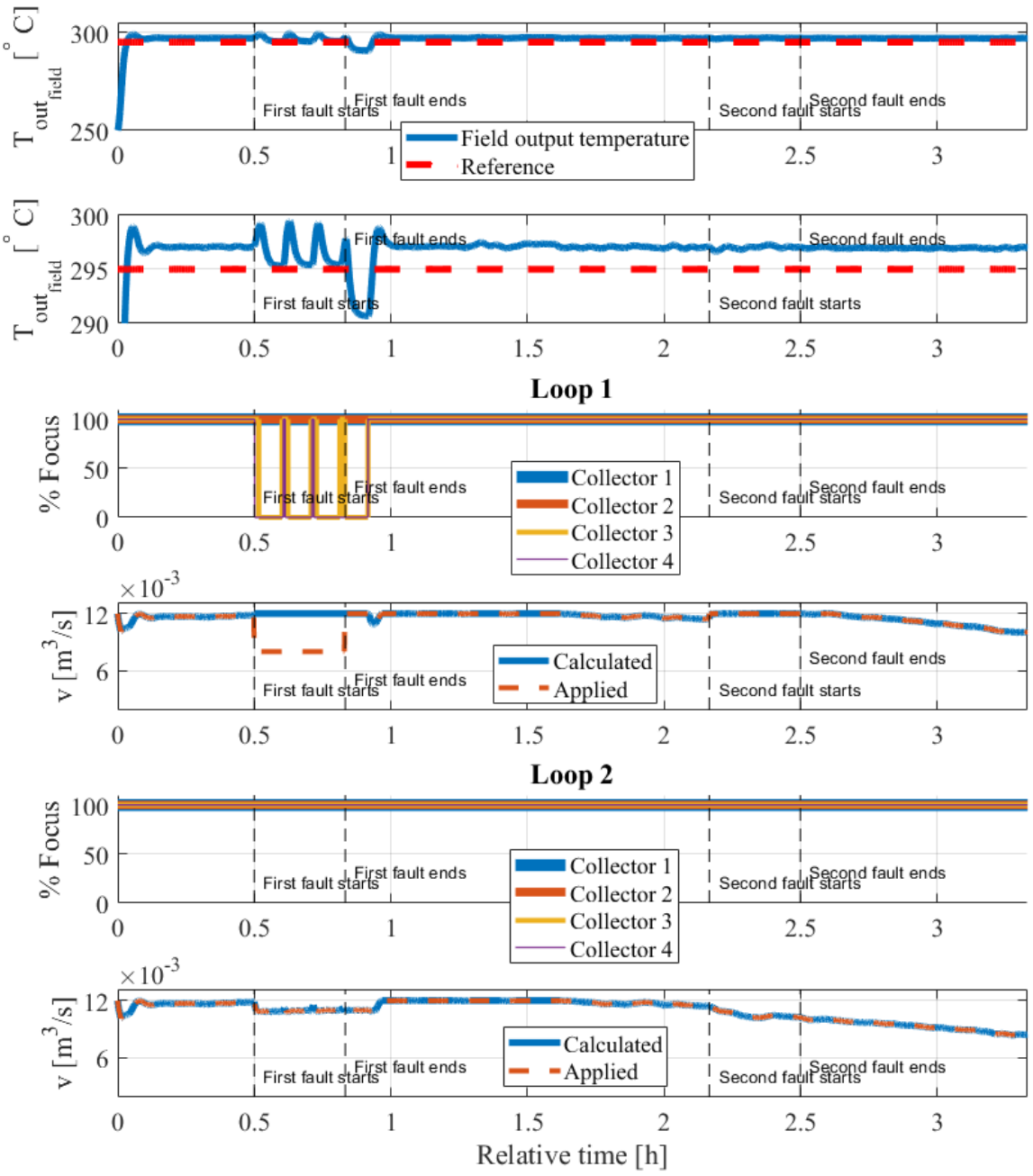

Source: The author.

Figure 25 – Simulation results for the case with parameter error, pump failure and controller with partial focus and high irradiance.

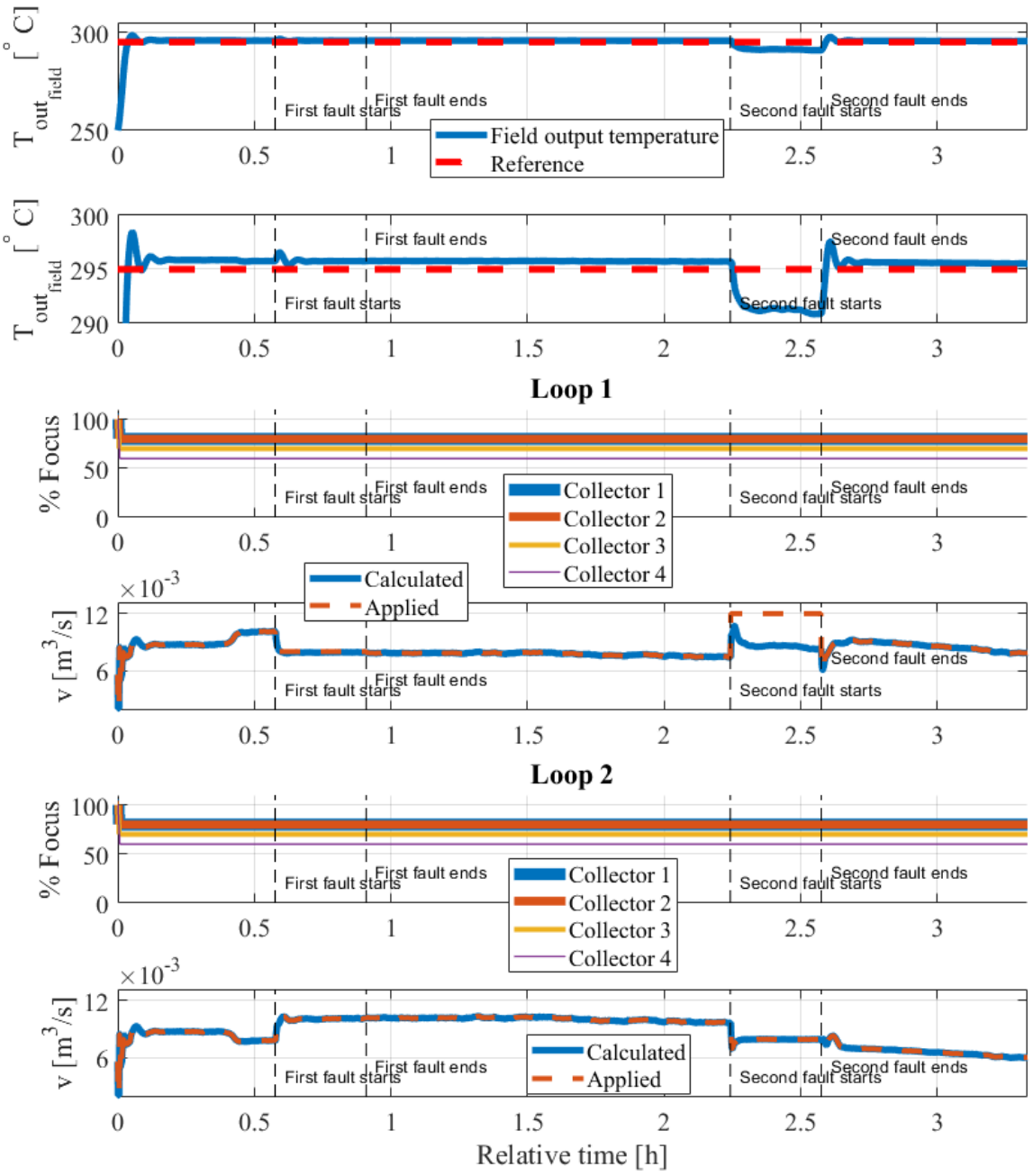

Source: The author.

Figure 26 – Simulation results for the case with parameter error, pump failure and hybrid controller, and high irradiance.

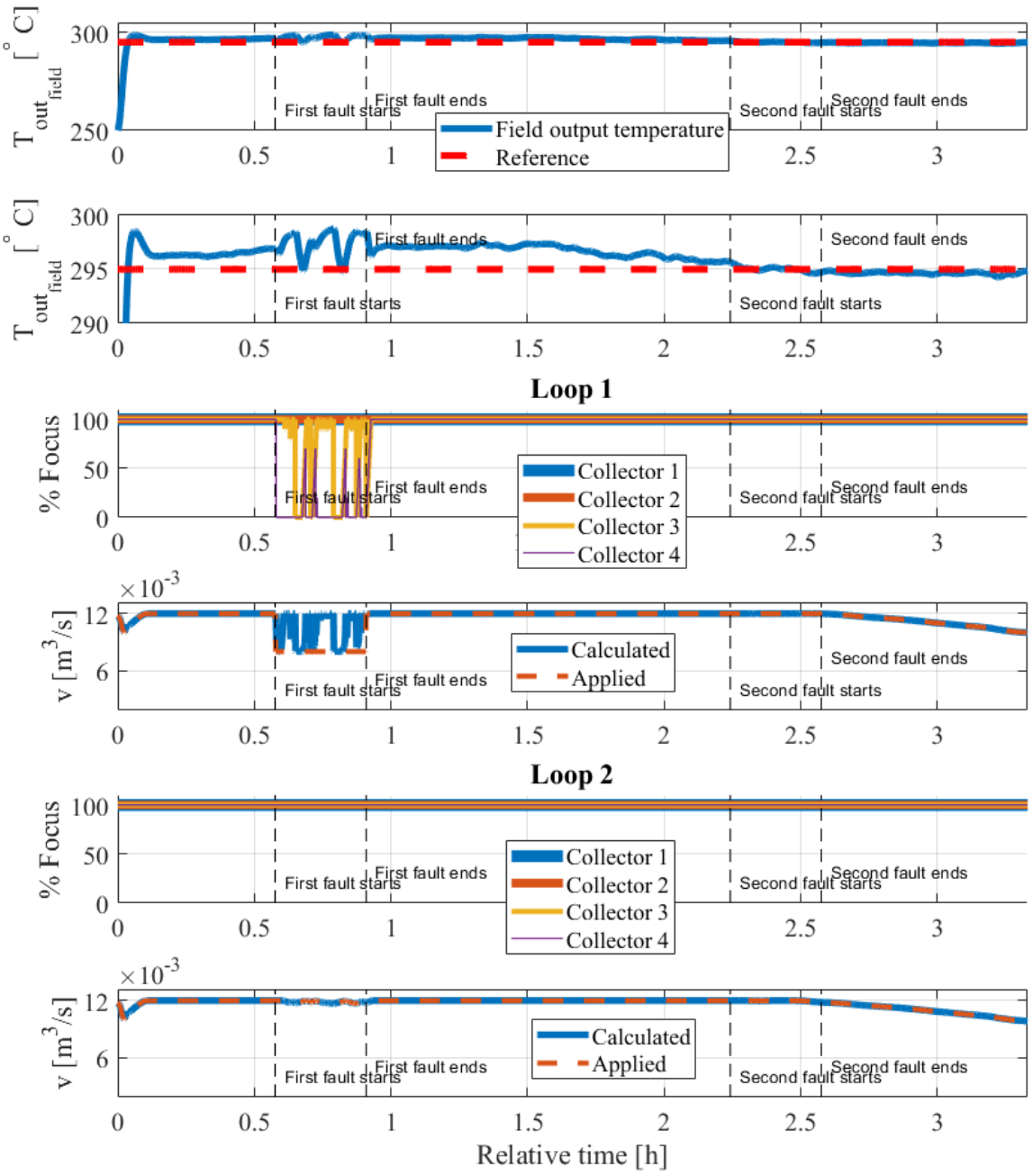

Source: The author.

3.2 FINAL REMARKS

This chapter presented a hybrid MPC algorithm for overheating prevention in a solar collector field that manipulates flow rate and focus values. The controller combined two previous MPC formulations that apply partial defocusing and On/Off of the collectors and is based on the PNMPC controller. The resulting mixed integer optimization problem is then solved at each controller iteration to obtain the optimal control actions. The controllers were compared by simulating a field of two-loop solar collectors with a validated process model. The irradiance and ambient temperature profiles used in the simulation were obtained from experimental data. Three simulation scenarios were evaluated to assess the performance of the controllers in situations that facilitate heat transfer fluid overheating.

The results showed that the On/Off controller presents satisfactory performance in all analyzed cases, but presents higher computation time when compared to the Partial and Hybrid controllers. The Partial controller presented the worst performance in general, with behaviors that often decreased the amount of energy absorbed by the HTF. Despite presenting similar behavior to the On/Off controller, in cases of pump failure the Hybrid controller proposes flow values that converge to the actual values in the loop where the failure occurs, which is desirable because it shows that the controller does not propose too many impossible actions during the failure. Also, when compared to the On/Off controller, the Hybrid controller showed lower computation times.

With the conclusion of the work presented in thesis chapter, the matter of how to implement the proposed defocus values in fresnel collectors must be adressed. In order to do so, the next chapter presents a simplified optical model for a fresnel collector. This model is later used to study how to implement some defocusing strategies and also the effects of uncertainties in this new actuator and how these uncertanties can affect the control system.

4 CONTRIBUTIONS: OPTICAL MODEL AND AIMING ALGORITHM FOR FRESNEL COLLECTORS

With the study of predictive controllers that use focus as a manipulated variable presented in Chapter 3, the issue arose as to how this defocusing of solar collectors can be implemented. To answer this question, it is necessary to study the optical characteristics of the solar collector in order to develop a strategy for implementing the defocusing. This chapter is dedicated to the development of a simplified optical model for a fresnel collector, so that, from the available information about the position of the Sun and Direct Normal Irradiance (DNI), the energy contribution of each mirror of the collector is known. As the contribution of each mirror is conditioned to the logic used in their manipulation in order to concentrate the irradiation on the absorber throughout the day (referred to as solar aiming algorithm), these mechanisms will also be analyzed in this section.

In face of the complexity and computational cost of the models available in the literature, the main contributions of this chapter are:

- Development of an optical model for a Fresnel collector with simplifications that allows its use in model-based control algorithms like Model Predictive Control;
- Proposal of two original solar aiming algorithms based on the optical model;
- Evaluation of three aiming methods while considering the manipulation of each individual mirror of the Fresnel collector;
- Proposal of a simple binary defocusing strategy.

The results of this chapter were published in the Renewable Energy journal, and can be found at Brandão, Costa Mendes, and Normey-Rico (2022).

4.1 THE OPTICAL MODEL

The simplified model proposed in this chapter is built in four steps: first, an estimation of the shaded area on each mirror is calculated; then, an estimation of the area of the absorber illuminated by each mirror is done; the third part consists of a correction of the illuminated area of the absorber, considering the shadow cast by the absorber on the mirrors. At last, the irradiance flux on the absorber is calculated, as well as the Incidence Angle Modifier (IAM).

The model assumes some simplifying hypothesis: (i) The Sun is not considered as a point source and the sun's rays are considered all parallel; (ii) Although solar tracking is not assumed, shading between non-neighbouring mirrors is neglected because it would mostly occur on mirror configurations that are unusual to the expected operation of these collectors; (iii) No blocking of the reflected rays of a mirror by another mirror.

Shaded area estimation

With the transversal angle of reflection $\theta_{t,i}$ defined, considerations on the amount of sunlight to be reflected by each mirror can be done by calculating the shaded region of the mirrors. Shadows in the mirrors can appear for several reasons, such as:

- Some structure in the vicinity of the collector projects a shadow. In urban areas, buildings can cause this kind of shadow.
- The absorber projects a shadow over the mirrors. This occurs when the sun is in the highest position on the day (for h_t values close to zero). On these moments the DNI is at its highest value, so this type of shading greatly impairs the performance of the collector.
- The positions of the collector's mirrors cause a shadow in the neighboring mirrors. This occurs mainly at the beginning and at the end of the day (for h_t values close to -90^o and 90^o).

In the proposed model, we consider the shadows caused by mirrors in other mirrors and the shadow caused by the absorber on the mirrors. In this section, a model for calculating the shadow between mirrors will be presented (illustrated in item c of Figure 27). The effect of the shadow cast by the absorber will be considered only when calculating where the reflected beam effectively intersects the absorber plane, on section 4.1.

A situation with an effect similar to the shading of a mirror is the case when some part of the reflected beam is blocked by a neighboring mirror (as shown in item b of Figure 27). This blocking situation will not be addressed in this model because it was considered to be insignificant for the situations in which a Fresnel solar thermal collector operates.

Figure 27 – Illustration of three situations of interactions between sunbeams and mirrors in Fresnel collectors.

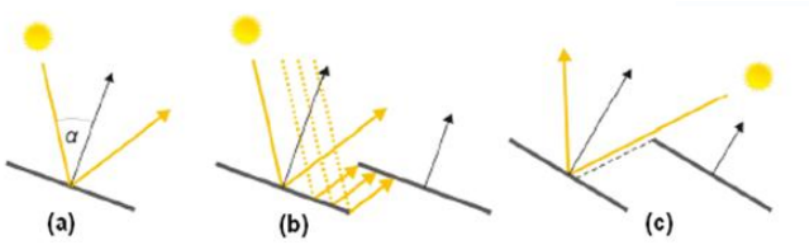

Source: Eddhibi et al. (2017).

An assumption made for this model, that simplifies the number of situations in which shading between mirrors occurs, is the existence of some tracking mechanism. When considering the effect of tracking possibilities (i.e. making some part of the beams

reflected by the mirrors hit the absorber), it is reasonable to consider that the following situations can be ignored:

- Mirror i shaded by a non-neighboring mirror.
- Mirror i shaded by a neighboring mirror j, tilted to the opposite inclination of mirror i (i.e. β_i sign different from the β_j sign).

Therefore, only three shading situations for a mirror i are considered:

1. Mirror i is not shaded;
2. Mirror i is shaded by mirror $i+1$, where $\beta_i \geq \beta_{i+1} \geq 0$ and $h_t \leq 0$ (represented in Figure 28 a);
3. Mirror i is shaded by mirror $i-1$, where $\beta_i \leq \beta_{i-1} \leq 0$ and $h_t \geq 0$ (represented in Figure 28 b).

Figure 28 – Illustration of the mirror shading situations considered on the model. Yellow line represents the solar ray that delimits the shaded area of mirror i.

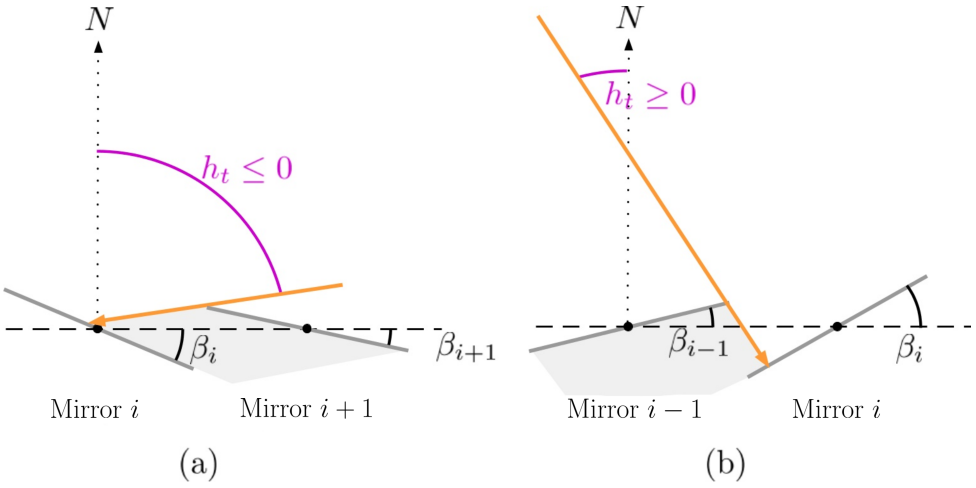

Source: The author.

Given these three possibilities, the proposed model calculates the shaded section on the mirror (S_i) and limits it so that:

1. If $S_i > L_{mirr}$ (the calculated shadow is greater than the width of the mirror), then it is limited to the width of the mirror ($S_i = L_{mirr}$) and there is complete shading of mirror i.
2. If $S_i < 0$ (the calculated shadow is smaller than the width of the mirror), then there is no shadow on mirror i, therefore S_i is set (corrected) to zero.
3. Otherwise, the value of S_i is maintained.

The handling of the S_i value described above allows differentiating the case with the absence of shadow. To differentiate between situations 2 and 3 and to calculate the S_i value, it will be necessary to analyze the geometry of the problem as follows.

Figure 29 represents situation 2 when there is a shadow bigger than half the width of the mirror. Analysing Fig. 8, five points can be highlighted:

Figure 29 – Important variables for calculating shadow in a mirror. Solar morning and shade greater than half of the mirror.

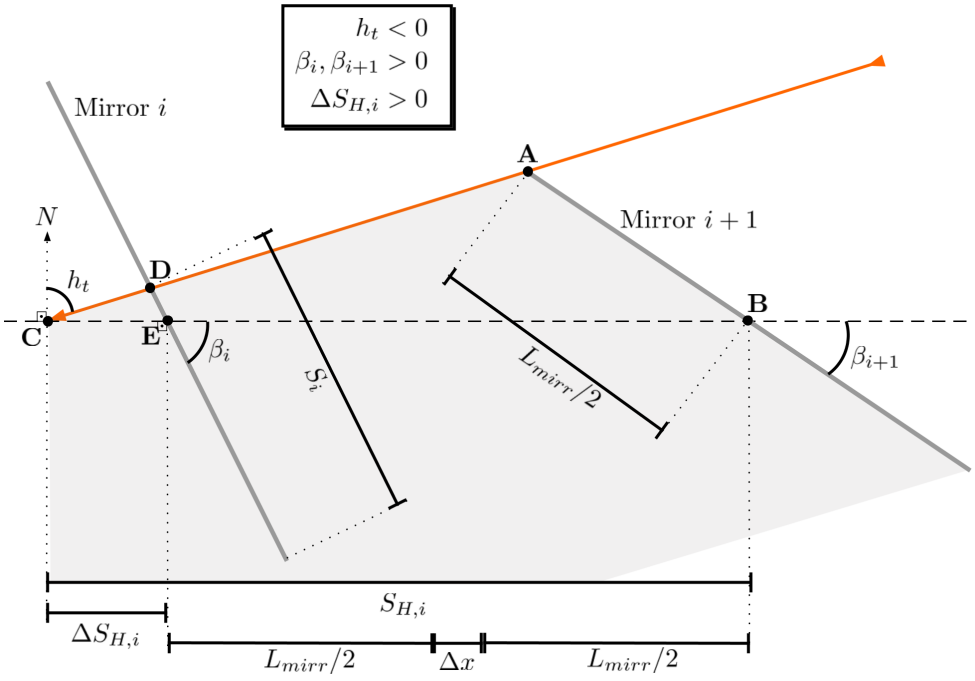

Source: The author.

- **A**: Point where the solar ray that limits the shadow in mirror i touches mirror $i+1$;
- **B**: Rotation axis of mirror $i+1$;
- **C**: Point where the solar ray that limits the shadow in mirror i intersects (or would intercept if it does not hit mirror i) in the plane of the mirrors;
- **D**: Point where the solar ray that limits the shadow in mirror i intersects mirror i;
- **E**: Rotation axis of mirror i.

Also in Figure 29, the following variables are defined:

- $S_{H,i}$: Width of the shadow that mirror $i+1$ casts on the plane of the mirrors, ignoring other mirrors;
- $\Delta S_{H,i}$: Position of point **C** subtracted from position of point **E**. It will be negative if the shadow in mirror i is less than half the width of the mirror.

The analysis of Figure 29 evidenciates the connection between $S_{H,i}$ and $\Delta S_{H,i}$ which given by:

$$\Delta S_{H,i} = S_{H,i} - (L_{mirr} + \Delta x). \tag{36}$$

The proposed model calculates the shaded region S_i from the connections between the scalene triangles $\angle$**ABC** and $\angle$**CDE** as illustrated in figures 30 and 31, both scalene.

Figure 30 – ABC triangle. Solar morning and shadow greater than half of the mirror.

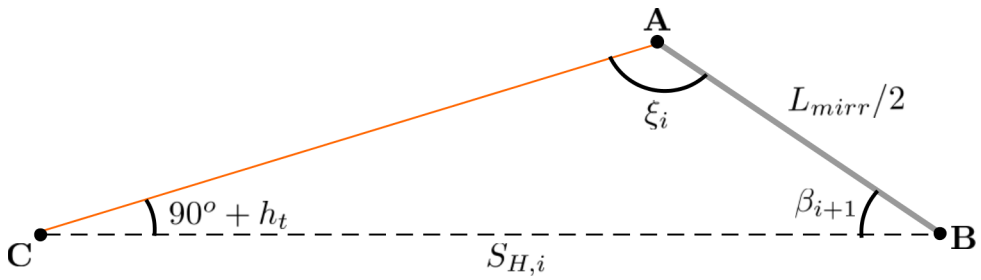

Source: The author.

Triangle $\angle$**ABC** has two angles that can be defined as a function of h_t and β_{i+1}, i.e. it is possible to determine the value of the angle ξ_i by adding the inner angles of the triangle:

$$\xi_i = 90^o - h_t - \beta_{i+1}. \tag{37}$$

As the opposite angle to the $\overline{\mathbf{BC}}$ side of the triangle is now known, it is possible to calculate $S_{H,i}$ from the law of sines:

$$S_{H,i} = \frac{L_{mirr}}{2} \frac{sin(\xi_i)}{sin(90^o + h_t)}. \tag{38}$$

With the calculated value of $S_{H,i}$, it is possible to obtain the value of $\Delta S_{H,i}$ from Equation (36). With this value, the triangle $\angle$**CDE** can be analyzed.

Figure 31 – CDE Triangle. Solar morning and shadow greater than half of the mirror.

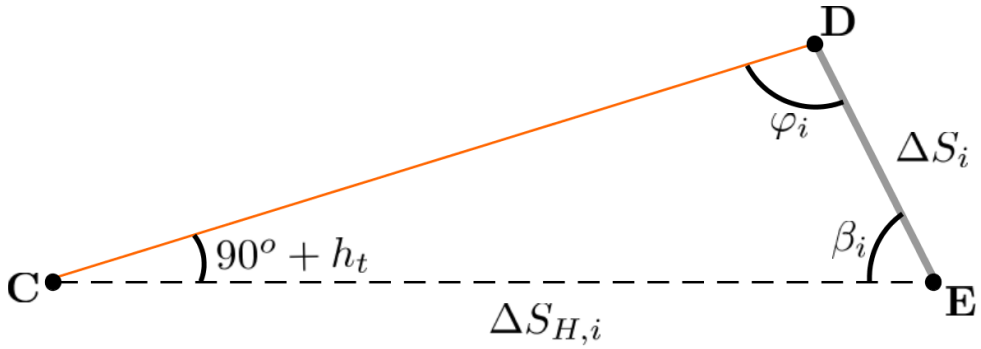

Source: The author.

This triangle helps to determine the value of ΔS_i. In a similar way to the procedure adopted in triangle $\angle$**ABC**, the value of φ_i from the sum of the internal angles of

the triangle can be obtained, resulting in Equation (39):

$$\varphi_i = 90^o - h_t - \beta_i. \tag{39}$$

Using the law of sines:

$$\Delta S_i = \Delta S_{H,i} \frac{sin(90^o + h_t)}{sin(\varphi_i)}. \tag{40}$$

With the value of ΔS_i it is possible to calculate the value of S_i from Equation (41):

$$S_i = \Delta S_i + \frac{L_{mirr}}{2}. \tag{41}$$

The value of S_i, calculated for the case exposed in Figure 29, allows to analyze if the relations obtained for this case apply when the shadow in mirror *i* is less than half the width of the mirror (i.e., if $S_i < L_{mirr}/2$, or equivalently, if $\Delta S_i < 0$). This situation is illustrated in Figure 32.

Figure 32 – Important variables for calculating shadow in a mirror. Solar morning and shade smaller than half of the mirror.

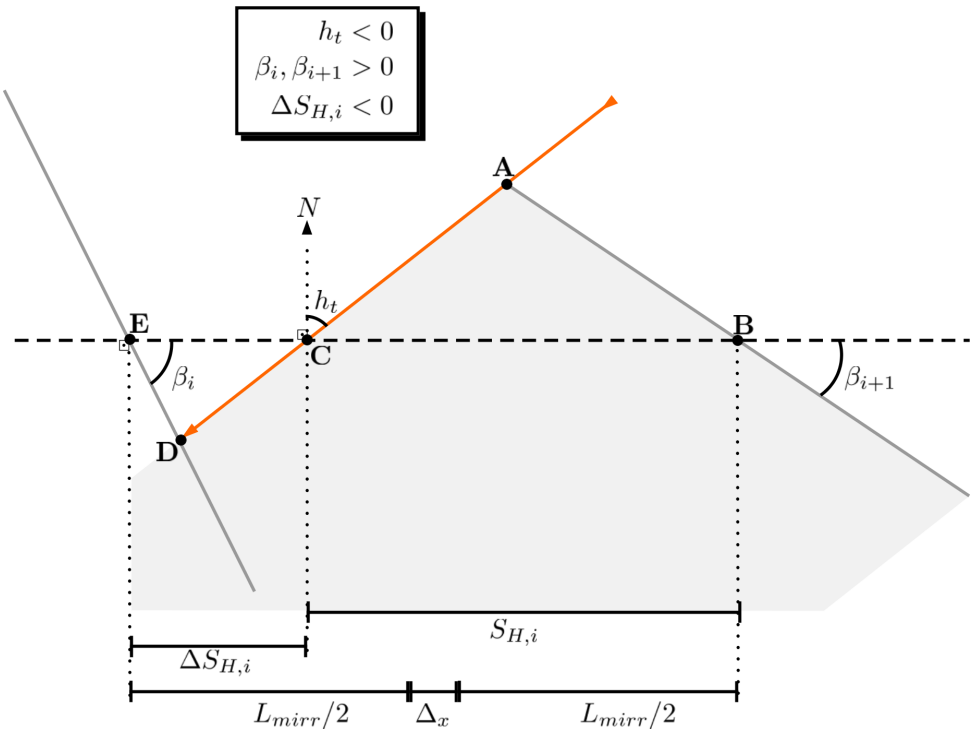

Source: The author.

Mounting the triangles ∠**ABC** and ∠**CDE**, and performing the same procedures described above, it is possible to obtain the same expressions. Therefore, these equations are valid for situation 2 ($\beta_i \geq \beta_{i+1} \geq 0$ and $h_t \leq 0$).

For situation 3 ($\beta_i \leq \beta_{i-1} \leq 0$ e $h_t \geq 0$), it is necessary to know mirror *i*–1 projecting shadow in mirror *i*. This situation is illustrated in Figure 33.

Figure 33 – Important variables for calculating shadow in a mirror. Solar evening and shade greater than half of the mirror.

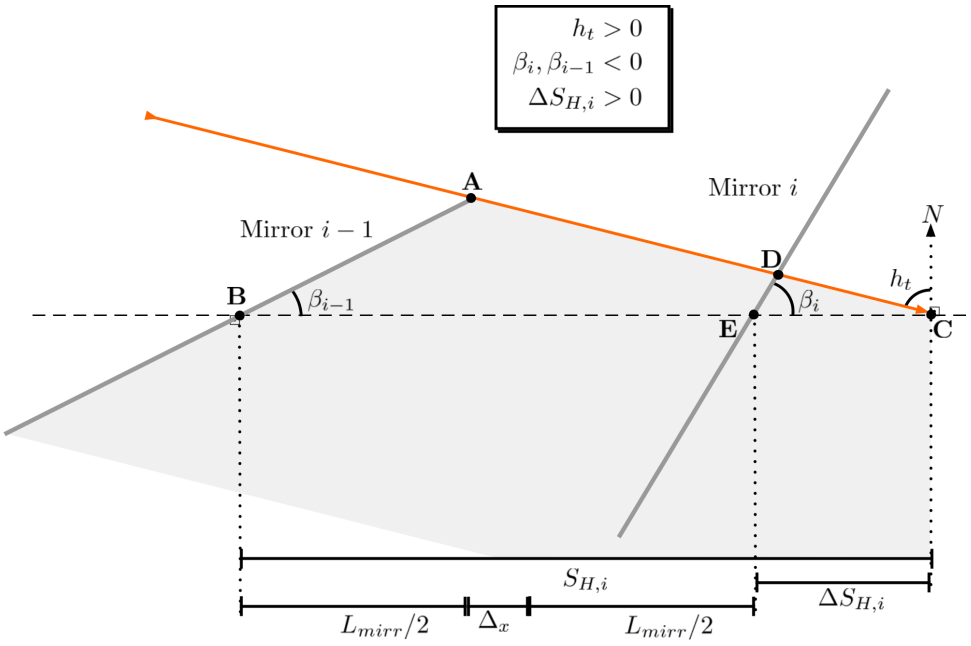

Source: The author.

Mounting the triangles ∠**ABC** and ∠**CDE** for this case and aware of the sign changes, procedures similar to those performed for situation 2 can be used, resulting in the following equations:

$$\xi_i = 90^o - h_t - \beta_{i-1}, \tag{42}$$

$$S_{H,i} = \frac{L_{mirr}}{2}\frac{sin(\xi_i)}{sin(-90^o + h_t)}, \tag{43}$$

$$\Delta S_{H,i} = S_{H,i} - (L_{mirr} + \Delta x), \tag{44}$$

$$\varphi_i = -90^o - h_t - \beta_i, \tag{45}$$

$$\Delta S_i = \Delta S_{H,i}\frac{sin(-90^o + h_t)}{sin(\varphi_i)}, \tag{46}$$

$$S_i = \Delta S_i + \frac{L_{mirr}}{2}. \tag{47}$$

With all cases evaluated, it is now possible to calculate the shadow appendix of the mirror for the considered situations. Hereafter, Algorithm 2 presented on A summarizes the calculation procedure developed in this section. It is important to note that in situation 2 the last mirror will never be shaded, while in situation 3 the first mirror will never be shaded.

Having the shaded region established, it is now possible to determine where the light beam reflected by the mirrors will reach the plane of the absorber. These equations will be presented in the following section, as well as the consideration of the absorber's shadow.

Absorber illuminated area estimation

When a collector mirror has a shaded region, only part of this mirror reflects the incident sun rays in the direction of the absorber. To be able to determine whether these beams intercept the absorber, it is necessary to know where these beams intercept the absorber's plane, as illustrated in figures 34 and 35, which represents the case $h_t < 0$.

Figure 34 – Illustration of variables used for calculating the incidence band on the absorber's plane.

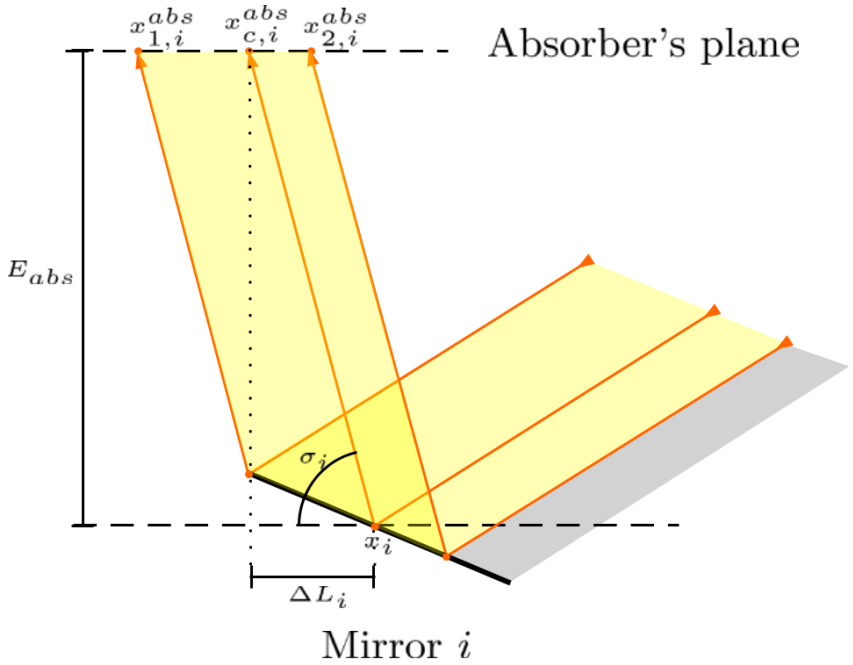

Source: The author.

In this figure, some important variables are illustrated to express where the beam reflected by the mirror falls on the plane of the absorber:

- $x^{abs}_{1,i}$: Position on the x axis of the most extreme point of the range reflected by the mirror i, when intercepting the plane of the absorber, in the west direction.
- $x^{abs}_{2,i}$: Position on the x axis of the farthest point of the band reflected by the mirror i, when intercepting the plane of the absorber, in the east direction.
- $x^{abs}_{c,i}$: Position on the x axis where a radius reflected at the center of the mirror i would intercept the plane of the absorber.
- δx_i: projection of the width of the mirror i in the plane of the mirrors (or absorber), in the direction of the reflected beams.
- δS_i: Projection of the shaded area S_i of the mirror i in the plane of the mirrors (or absorber), in the direction of the reflected beams.

Figure 35 – Illustration of variables used for calculating the incidence band on the absorber's plane.

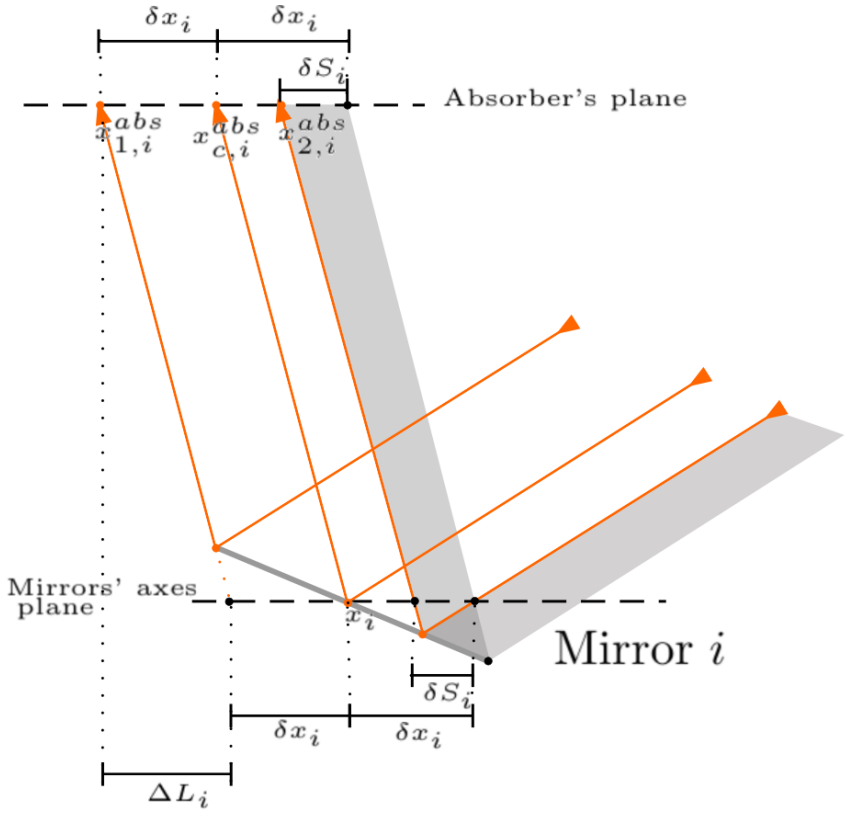

Source: The author.

- ΔL_i: difference between x_i and $x^{abs}_{c,i}$. It will be negative if the reflected rays are in the west direction (left of the figure).
- σ_i: Angle between the reflected rays in the mirror i and the plane of the mirrors' axes.

The observation of Figure 34, as well as the definitions of h_t and $\theta_{t,i}$ presented previously allows to obtain the following expression for the calculation of σ_i:

$$\sigma_i = -2\theta_{t,i} + 90^o + h_t. \tag{48}$$

Consequently, knowing the value of the absorber elevation (E_{abs}), it is possible to calculate ΔL_i through the relations between angles and sides in a rectangle, resulting in the expression:

$$\Delta L_i = \frac{E_{abs}}{tan(\sigma_i)}. \tag{49}$$

From the definition of ΔL_i and with its value calculated by the Equation (49) (note that in this case $\Delta L_i < 0$), it is possible to write an expression to determine $x^{abs}_{c,i}$:

$$x^{abs}_{c,i} = x_i + \Delta L_i. \tag{50}$$

For the same situation, more useful variables can be defined, as shown in Figure 35. Note that to determine the region where the reflected band falls in the plane of the

absorber, given by the pair ($x_{1,i}^{abs}$, $x_{2,i}^{abs}$), it is necessary to know the values of $x_{c,i}^{abs}$, δx_i and δS_i. To calculate the value of δS_i, an analisys of the relationships between incidence angles, reflection, and inclination in mirror *i* must be carried out. A ilustration of these variables for the case evaluated is presented in Figure 36.

Figure 36 – Detailment of the triangle and relevant angles for obtaining the projection of the shaded area of mirror *i* on the direction of the reflected rays on the plane of the mirrors' axes.

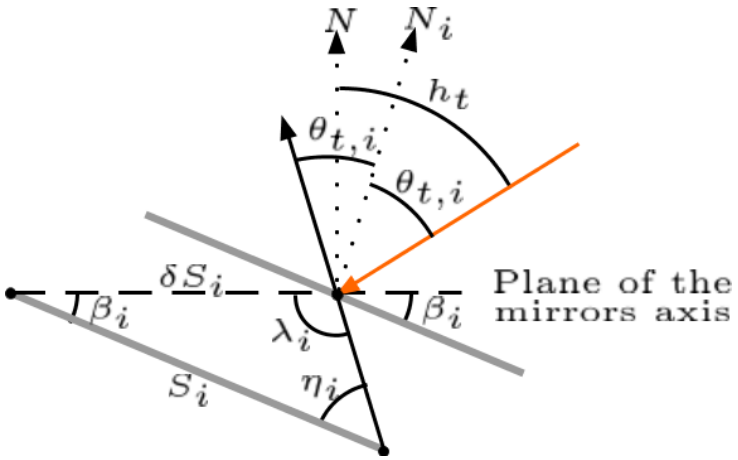

Source: The author.

Analyzing the angles and the triangle shown in the figure, the derivation of an expression to obtain η_i is straightforward as follows:

$$\eta_i = 2\theta_t - h_t + 90^o - \beta_i. \tag{51}$$

With this value and knowing the values of S_i and λ_i ($\lambda_i = 180^o - \sigma_i$), it is possible to calculate the value of δS_i through the law of sines applied to the triangle shown in Figure 36, resulting in the Equation (52).

$$\delta S_i = S_i \frac{sin(\eta_i)}{sin(\lambda_i)}. \tag{52}$$

And, in a similar way:

$$\delta x_i = \frac{L_{mirr}}{2} \frac{sin(\eta_i)}{sin(\lambda_i)}. \tag{53}$$

With the value of δS_i calculated and the previously established relationships, we can obtain the incident range in the plane of the absorber is defined by:

$$x_{1,i}^{abs} = x_{c,i}^{abs} - \delta x_i, \tag{54}$$

$$x_{2,i}^{abs} = x_{c,i}^{abs} + \delta x_i - \delta S_i. \tag{55}$$

With the incident range calculated, the shadow effect of the absorber into the mirrors is introduced. This compensation takes place in a few steps, illustrated in Figure 37:

- Projection of the incident range in the absorber plane ($x_{1,i}^{abs}$, $x_{2,i}^{abs}$) at the angle of incidence in the absorber, resulting in ($x_{1,i}^{mirr}$, $x_{2,i}^{mirr}$);
- Projection of the absorber shadow in the plane of the mirrors' axes in the direction of the transverse solar incidence angle (h_t), resulting in ($x_{1,abs}^{mirr}$, $x_{2,abs}^{mirr}$);
- Comparison of intersections between ($x_{1,i}^{\prime mirr}$, $x_{2,i}^{\prime mirr}$) and ($x_{1,abs}^{\prime mirr}$, $x_{2,abs}^{\prime mirr}$), determining the values for the range reflected in the plane of the absorber ($x_{1,abs}^{\prime mirr}$, $x_{2,abs}^{\prime mirr}$)

Figure 37 – Illustration of variables used for calculating the incidence band on the absorber's plane, considering the absorber's shadow.

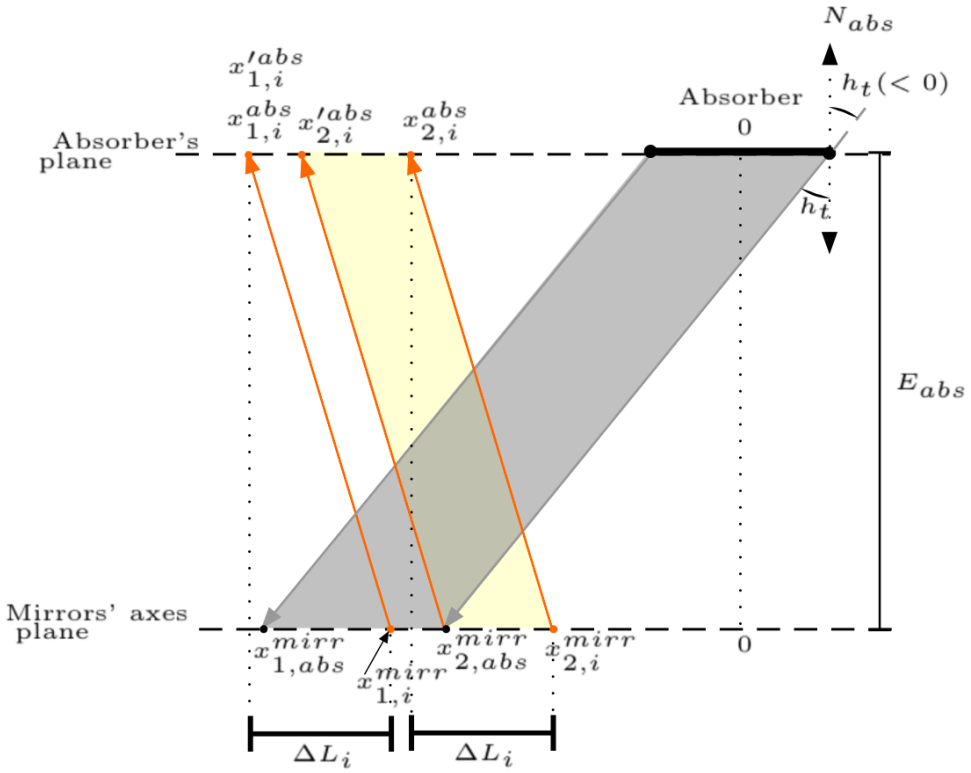

Source: The author.

As seen before, to obtain the projection of the illuminated band in the plane of the mirrors' axes, it is enough to have the knowledge of the value of ΔL_i (already calculated by the Equation (49)), resulting in

$$x_{1,i}^{mirr} = x_{1,i}^{abs} - \Delta L_i. \tag{56}$$

$$x_{2,i}^{mirr} = x_{2,i}^{abs} - \Delta L_i. \tag{57}$$

The values of ($x_{1,abs}^{mirr}$, $x_{2,abs}^{mirr}$) can be obtained from the relationship of the rectangle formed by the plane of the mirrors' axes, the direction of the shadow of the absorber, passing through the center of the absorber, and the elevation of the absorber,

resulting in

$$x_{1,abs}^{mirr} = \frac{E_{abs}}{tan(90^o + h_t)} - \frac{L_{abs}}{2}, \tag{58}$$

$$x_{2,abs}^{mirr} = \frac{E_{abs}}{tan(90^o + h_t)} + \frac{L_{abs}}{2}. \tag{59}$$

Finally, the binary variable S_i^{mid}, which has a value of 1 if the absorber shadow is contained within the illuminated range is defined.

With the projections in the plane of the mirrors' axes defined, it is possible to investigate if there is interception between them and make the assignments of the values to ($x_{1,i}^{\prime abs}$,$x_{2,i}^{\prime abs}$). This comparison can be described as follows:

- Case $x_{2,abs}^{mirr} > x_{1,i}^{mirr}$ and $x_{2,abs}^{mirr} < x_{2,i}^{mirr}$ implies in the intersection on the west side.
  - Case $x_{1,abs}^{mirr} < x_{1,i}^{mirr}$ and $x_{2,abs}^{mirr} > x_{1,i}^{mirr}$, the shadow of the absorber is in the middle of the illuminated band, therefore:

$$S_i^{mid} = 1, \tag{60}$$

$$x_{1,i}^{\prime abs} = x_{1,i}^{abs}, \tag{61}$$

$$x_{2,i}^{\prime abs} = x_{2,i}^{abs}, \tag{62}$$

    Otherwise:

$$S_i^{mid} = 0, \tag{63}$$

$$x_{1,i}^{\prime abs} = x_{1,i}^{mirr} + \Delta L_i + (x_{2,abs}^{mirr} - x_{1,i}^{mirr}) = x_{1,i}^{abs} + (x_{2,abs}^{mirr} - x_{1,i}^{mirr}), \tag{64}$$

$$x_{2,i}^{\prime abs} = x_{2,i}^{abs}. \tag{65}$$

- Case $x_{1,abs}^{mirr} < x_{2,i}^{mirr}$ and $x_{1,abs}^{mirr} > x_{1,i}^{mirr}$ results in the intersection on the east side.
  - Case $x_{2,abs}^{mirr} > x_{1,i}^{mirr}$ and $x_{2,abs}^{mirr} < x_{2,i}^{mirr}$, we have that the shadow of the absorber is in the middle of the illuminated band, therefore:

$$S_i^{mid} = 1, \tag{66}$$

$$x_{1,i}^{\prime abs} = x_{1,i}^{abs}, \tag{67}$$

$$x_{2,i}^{\prime abs} = x_{2,i}^{abs}, \tag{68}$$

    Otherwise:

$$S_i^{mid} = 0, \tag{69}$$

$$x_{1,i}^{\prime abs} = x_{1,i}^{abs}, \tag{70}$$

$$x_{2,i}^{\prime abs} = x_{2,i}^{mirr} + \Delta L_i + (x_{1,abs}^{mirr} - x_{2,i}^{mirr}) = x_{2,i}^{abs} + (x_{1,abs}^{mirr} - x_{2,i}^{mirr}). \tag{71}$$

Otherwise, there is no intersection of the absorber's shadow with the i mirror, therefore:

$$S_i^{mid} = 0, \tag{72}$$

$$x_{1,i}^{'abs} = x_{1,i}^{abs}, \tag{73}$$

$$x_{2,i}^{'abs} = x_{2,i}^{abs}. \tag{74}$$

This calculates the band in the plane of the absorber that is illuminated by mirror i, for $h_t < 0$. The case for $h_t > 0$ is obtained in a similar way. Algorithm 3 presented on A shows the complete process for calculating the illuminated range in the plane of the absorber for any situation.

With the values of the radiation incidence ranges reflected by the mirrors already known, it is possible to compute the flow received by the absorber, taking into account the radiance concentration promoted by the collector. This calculation will be presented in the next section.

Absorber Irradiance flux estimation

In order to obtain the flow that falls on the absorber, it is necessary to know how much of the flow that falls on the mirrors is redirected to the absorber, which portion of this flow hits the absorber and which types of effects can attenuate the incident flow. One of the main components that cause the decrease of the flow in the absorber is due to these losses by cosine. Figure 38 presents an illustration to present this concept.

Figure 38 – Illustration of losses by cosine.

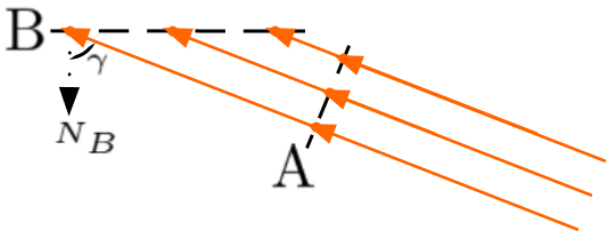

Source: The author.

Cosine losses occur when a flow (energy per area) is not perpendicular to a surface. In Figure 38, the three arrows represent a flow of energy similar to solar radiance. When one considers the distribution of the arrows of the figure along the plane **A** compared with their incidence in the plane **B**, one can notice that in the plane **B**, they are distributed in a larger area. Considering that each arrow carries an equal amount of energy, it is possible to conclude that the flow of energy through the **B** plan will be smaller, since the same amount of energy is focused on a larger area.

Due to the geometry of the problem, it is possible to notice that this decrease in the value of the flow is related to the cosine of the incidence angle in the analyzed

plane. Therefore, we have that, considering a flow f incurring in a surface **B** with angle γ, the value of the flow applied in this plane is given by:

$$f_{\mathbf{B}} = f\,cos(\gamma). \tag{75}$$

In the case of the Fresnel collector, the losses by cosine are different for each mirror and should be considered individually when calculating the flow in the absorber.

With the knowledge of the incidence ranges of the reflected rays by each mirror i ($x'^{abs}_{1,i}, x'^{abs}_{2,i}$), the calculation of the flow in the absorber consists in verifying which part of the reflected range hits the absorber and multiplying this value by the cosine of the incidence angle. These values are summed up and results in the incidence factor (τ_t), as presented in Algorithm 4.

With the execution of this algorithm, the value of τ_t is obtained, which when multiplied by the DNI provides the value of the irradiance flow, considering the geometry of the collector. Next, the concept of the Incidence Angle Modifier (*IAM*) will be presented and how to calculate it from the flow τ_t.

Incidence angle modifier

The incidence angle modifier is an interesting indicator to evaluate the optical behavior of collectors. It is defined as a ratio between the flow in the absorber at a given time and the flow in the absorber at the moment of maximum solar incidence, when $h = 0^o$. Therefore, it is a measure of when the flux at a given time compares with the flux at the moment of peak irradiation.

To facilitate the analysis of *IAM*, it can generally be divided into two components: transversal (IAM_t) and longitudinal (IAM_l), the relationship between them being given by:

$$IAM = IAM_t \times IAM_l.$$

The longitudinal component of the *IAM* can be calculated by analyzing the behavior of the collector for variations of h_l. Figure 39 presents an illustration of important variables for calculating transverse *IAM*.

Figure 39 – Illuminated longitudinal band and important angles for obtaining IAM_l.

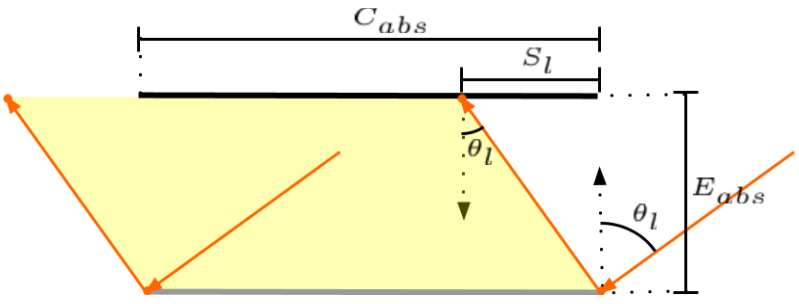

Source: The author.

When analyzing Figure 39, it is possible to notice that depending on the length of the absorber, the mirrors and the angle θ_l, part of the absorber does not receive solar irradiation reflected by the mirrors. This shadow on the absorber is the main component that affects the flow in the transversal direction. Another important component for the decrease of the flow in this direction are the losses by cosine. In this case, it is remarkable that the longitudinal angle of incidence in the mirrors (θ_l) is equal to the angle of incidence of the rays reflected in the absorber.

Considering these two components, the longitudinal incidence factor (θ_l) can be calculated by Algorithm 5 presented on A.

With all the elements of the optical model defined, one more development is still necessary: to establish narrow limits (β_i^{min} and β_i^{max}) for the inclinations of the mirrors. These restrictions will be necessary for one of the tracking proposals to present consistent results.

Mirror angle limits

The minimum and maximum inclination limits for each mirror and for a given time of day were obtained considering the situations in which the beam reflected by the mirror intercepts the absorber on the east side (β_i^{max}) and west side (β_i^{min}). These boundary conditions are illustrated in Figure 40.

Figure 40 – Illustration of the mirror inclination limits.To the right, the upper limit; To the left, the lower limit.

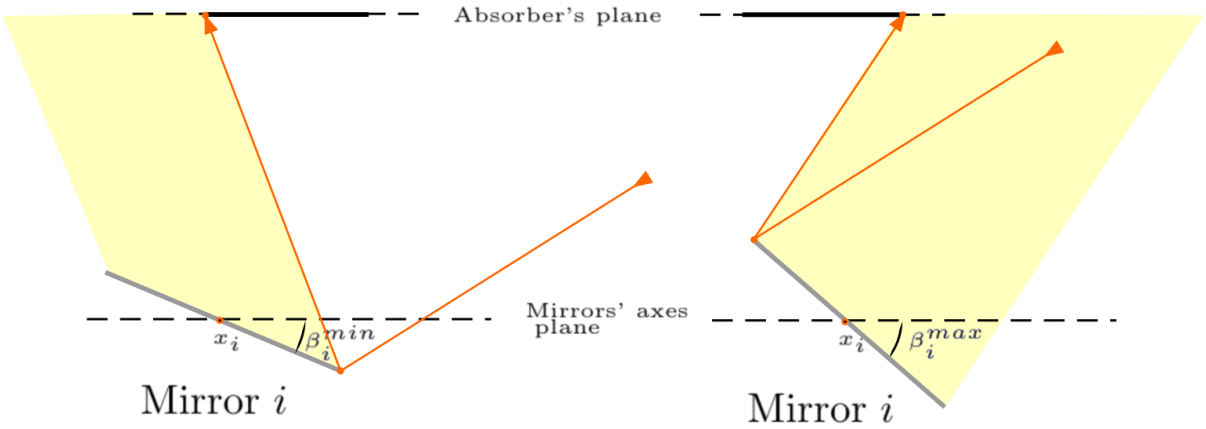

Source: The author.

To obtain the minimum inclination value (β_i^{min}), consider the situation described by Figure 41. In this case the incident rays come from the sunrise direction, so $h_t \leq 0$, besides, due to the mirror inclination, the angle $\beta_i^{min} \geq 0$. The points *A*, *B*, *C*, *D* and *E* are defined as:

- *A*: Rightmost point of the mirror, where the radius that will tangent the absorber will be reflected;
- *B*: Projection in the plane of the mirrors' axes of point *A*;
- *C*: Mirror axis rotation analyzed;
- *D*: Point projection *E* in the plane of the mirrors' axes;
- *E*: leftmost point of the absorber, where the radius reflected by the point *A* tangents it.

Figure 41 – Case of mirror with minimal inclination.

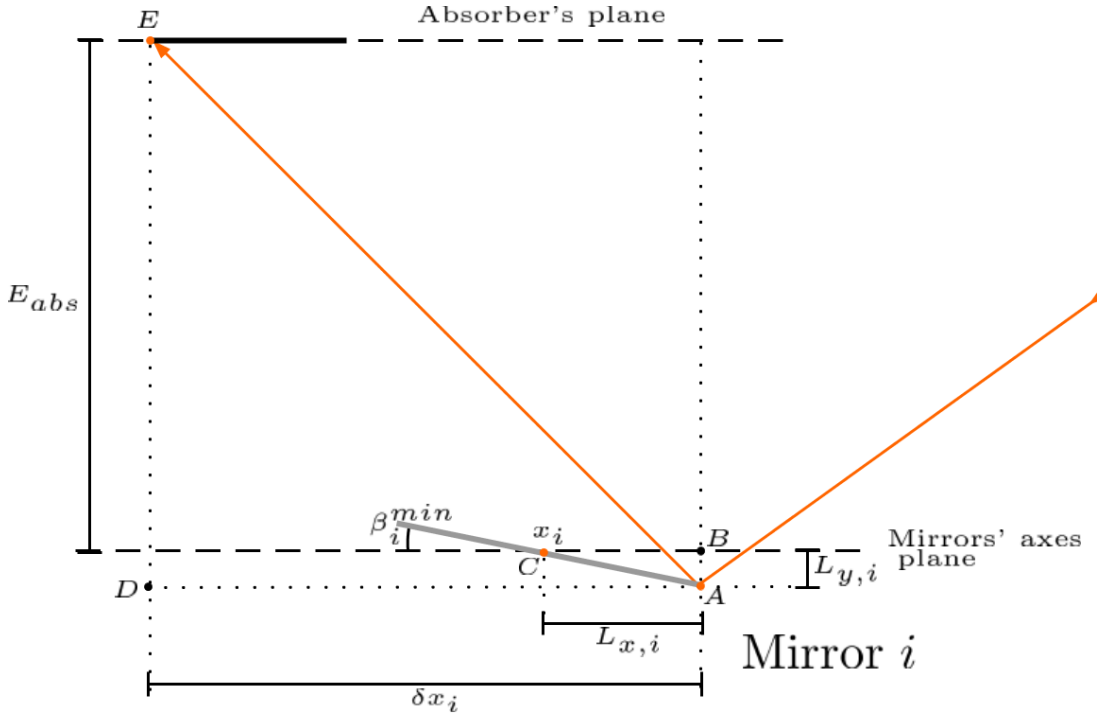

Source: The author.

The Figure 42 shows the $\angle ABC$ and $\angle ADE$ triangles, as well as showing how h_t and $\theta_{t,i}$ relate geometrically. Also in this figure are defined the angles ϕ_i and α_i, which will be calculated as follows

Figure 42 – Detailing of triangles on case with minimal mirror inclination and $h_t \leq 0$.

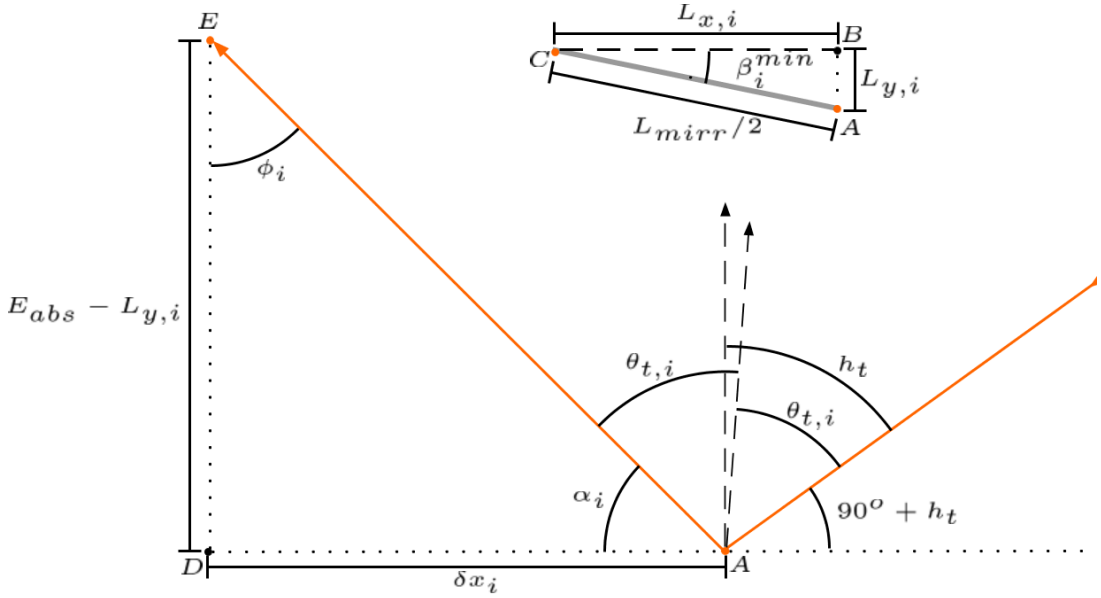

Source: The author.

From the equation 4:

$$\theta_{t,i} = h_t + \beta_i^{min}. \tag{76}$$

Analyzing the $\angle ABC$ triangle and the sine and cosine relations in a rectangle:

$$L_{y,i} = \frac{L_{mirr}}{2} sin(\beta_i^{min}), \tag{77}$$

$$L_{x,i} = \frac{L_{mirr}}{2} cos(\beta_i^{min}). \tag{78}$$

Analyzing the relationship between α_i, $\theta_{t,i}$ and h_t in the $\angle ADE$ triangle, results in $180^o = \alpha_i - 2\theta_{t,i} + 90^o + h_t$. Soon:

$$\alpha_i = 90^o + 2\theta_{t,i} - h_t. \tag{79}$$

From the sine relationship in the $\angle ADE$ triangle:

$$\delta_{x_i} = \frac{E_{abs} - L_{y,i}}{tan(\alpha_i)}. \tag{80}$$

With these variables defined, it is possible to notice that for the ray reflected at the point A to tangent the absorber at the point E, the following expression must be satisfied:

$$x_i + L_{x,i}(\beta_i) - \delta_{x_i}(\beta_i) + \frac{L_{abs}}{2} = 0. \tag{81}$$

Therefore, by numerically solving the Equation (81) for β_i, it is possible to obtain the value of β_i^{min} for $h_t \leq 0$. For the case of $h_t \geq 0$, building the same triangles $\angle ABC$ and $\angle ADE$ and establishing similar relations, its possible to realize that only the equations

(79) and (80) are changed, becoming:

$$\alpha_i = 90^o - 2\theta_{t,i} + h_t, \tag{82}$$

$$\delta_{x_i} = \frac{-(E_{abs} - L_{y,i})}{tan(\alpha_i)}. \tag{83}$$

Therefore, Algorithm 6 presented on Appendix A shows the complete procedure for the calculation of β_i^{min}. For the calculation of β_i^{max}, the situation exposed in Figure 43 must be analyzed. New triangles $\angle ABC$ and $\angle ADE$ are defined, as illustrated in Figure 44. Building relationships in a similar way to the one done for the calculation of β_i^{min}, it's possible to assemble Algorithm 7 presented on Appendix A for the calculation of β_i^{max}.

Figure 43 – Case of mmirror with maximal inclination.

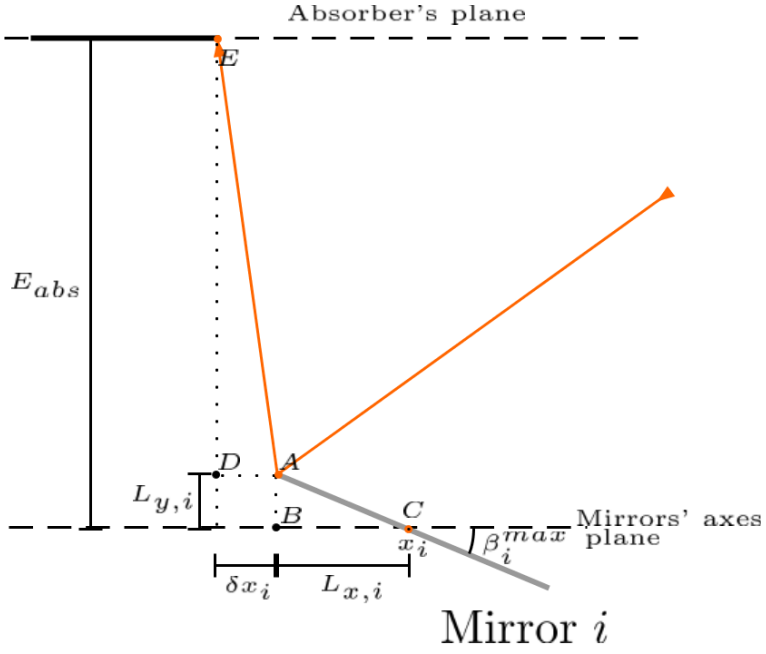

Source: The author.

Figure 44 – Detailing of triangles on case with maximal mirror inclination and $h_t \leq 0$.

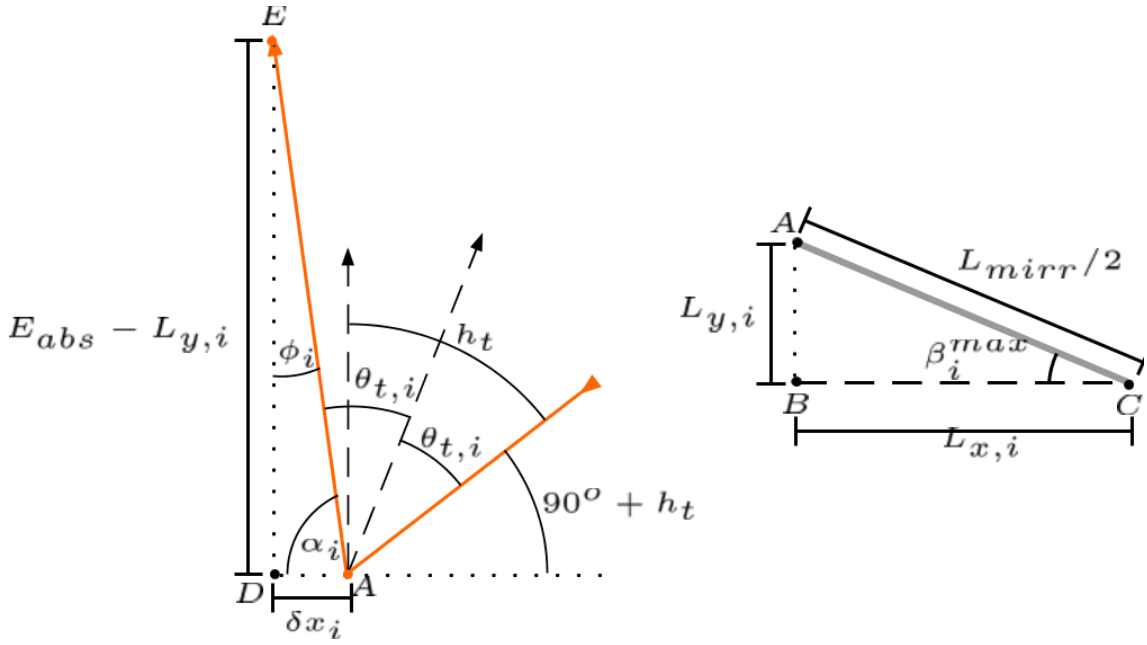

Source: The author.

4.2 VALIDATION OF THE OPTICAL MODEL

To validate the proposed model, a methodology based on (SÁ et al., 2018) was used, consisting of a comparison of the IAMs obtained in the proposed model with the values obtained in a software of ray tracing and from experimental data. In this work, (WENDELIN, 2003) was used as a reference model. This program is available for free and also has open source. Figure 45 presents a synoptic of the program, showing the collector's design and some solar ray traces.

Figure 45 – SolTrace interface.

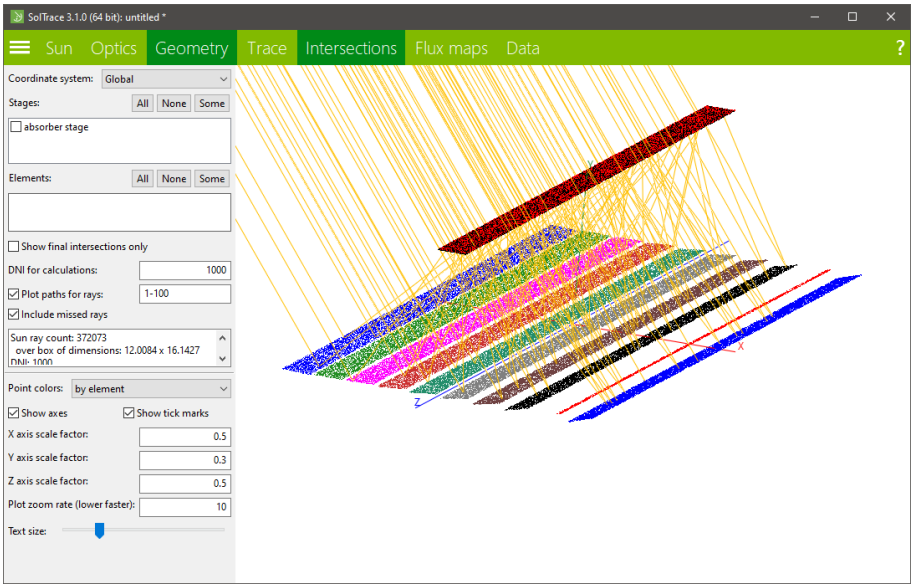

Source: Wendelin (2003).

Parameter	**Value**	**Unit**
n_{mirr}	11	-
Δx	0.2	m
L_{mirr}	0.5	m
C_{mirr}	64	m
L_{abs}	0.3	m
C_{abs}	64	m
E_{mirr}	4.00	m

Table 3 – Parameters of the collector used in the validation.

The parameters of the collector considered in this study were obtained from a commercial product by (SOLAR, 2007) and are presented on Table 3. The values of the solar angles were generated between 0^o and 90^o, to evaluate the behavior of the model in a wide range of values. To determine the inclinations of the mirrors for both simulations, a simple tracking scheme was used, which will be described in the next section.

In order to use the SolTrace software, a sun shape must be defined for the computations of the solar rays paths. The Buie distribution (BUIE et al., 2003) was selected, with the parametrization and modeling given by (WILBERT, 2014), which adjusted the data provided by Neumann et al. (2002) to fit the Buie model. This resulted on Equations (84), (85) and (86), with α being the radial distance, given in milliradians. The circumsolar ratio (CSR) considered for this sun shape was 0.3.

$$L_{Buie,rel}(\alpha) = \begin{cases} \frac{cos(0.326\cdot\alpha)}{cos(0.308)\cdot\alpha}; & \alpha \leq 4.65, \\ e^{k}\alpha^{\gamma}; & \alpha > 4.65, \end{cases} \tag{84}$$

$$\gamma = 2.2 \cdot ln(0.52 \cdot CSR) \cdot CSR^{0.43} - 0.1, \tag{85}$$

$$k = 0.9 \cdot ln(13.5 \cdot CSR) \cdot CSR^{-0.3}. \tag{86}$$

With the provided model, it is now possible to generate a sun shape profile curve, as shown on Figure 46. The 100 data points used to build Figure 46 were provided to Soltrace.

In order to validate the proposed model, two references were considered: SolTrace model and manufacturer data sheet IAM data. As the manufacturer IAM data does not consider an specific absorber, the proposed model must be slightly changed in order to compute a comparable IAM. This can be done by replacing lines 3-11 of Algorithm 4 presented on A to not consider if the absorber was hit by the reflected ray, thus $x_{1,i}^{\prime abs} = x_{inf}$ and $x_{2,i}^{\prime abs} = x_{sup}$. It is not possible to reproduce such characteristics of the manufacturer data on the SolTrace software (i.e. disconsider of the reflected rays intercept the absorber while considering the effects of the absorber's shadow over the

Figure 46 – Buie sun shape profile.

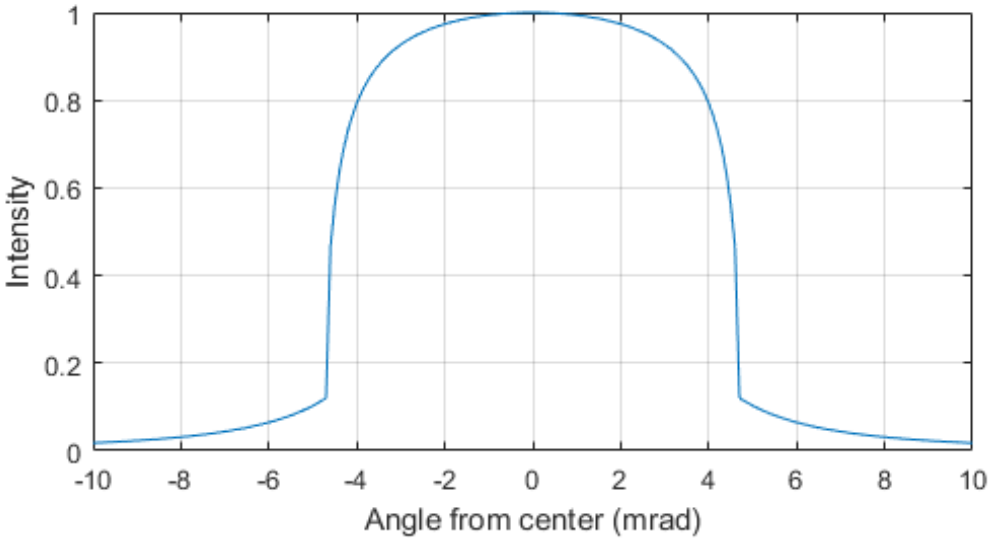

Source: The author.

mirrors), thus the results comparing the proposed model with the manufacturer's data and the SolTrace results are presented separately.

The comparison of IAM with the SolTrace results for IAM_t and IAM_l are presented on figures 47 and 48. It is notorious from the analysis of the figures that the proposed model is able to reproduce the geometric behavior obtained by SolTrace with little deviation. It is also evident the important effect that the absorber's shadow has on the IAM_t, observable by the stagnate behaviour at smaller values of transversal solar hour angle.

Figure 47 – Comparison of IAM_t from SolTrace and the proposed model.

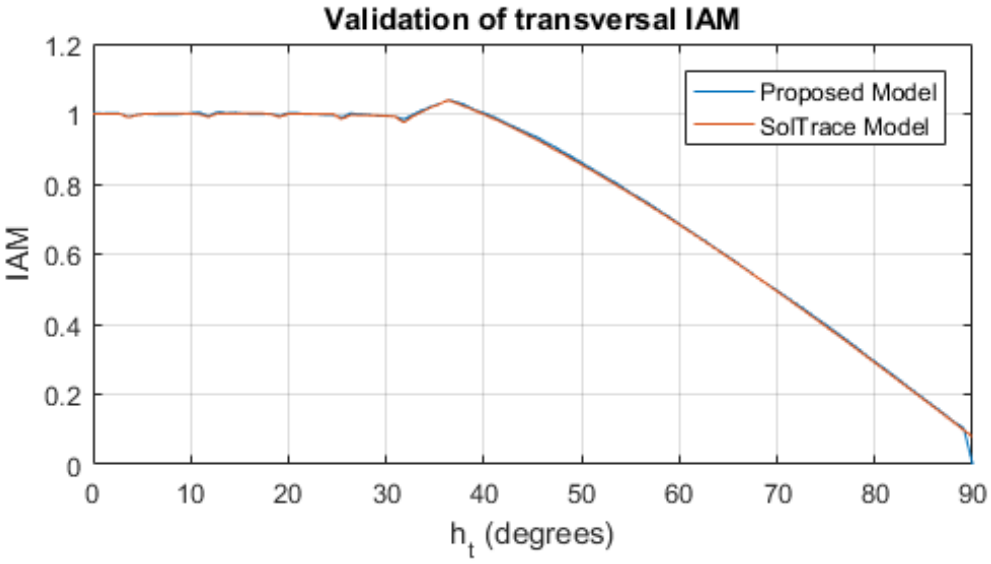

Source: The author.

The results comparing the proposed model with the manufacturer's data are

Figure 48 – Comparison of IAM_l from SolTrace and the proposed model.

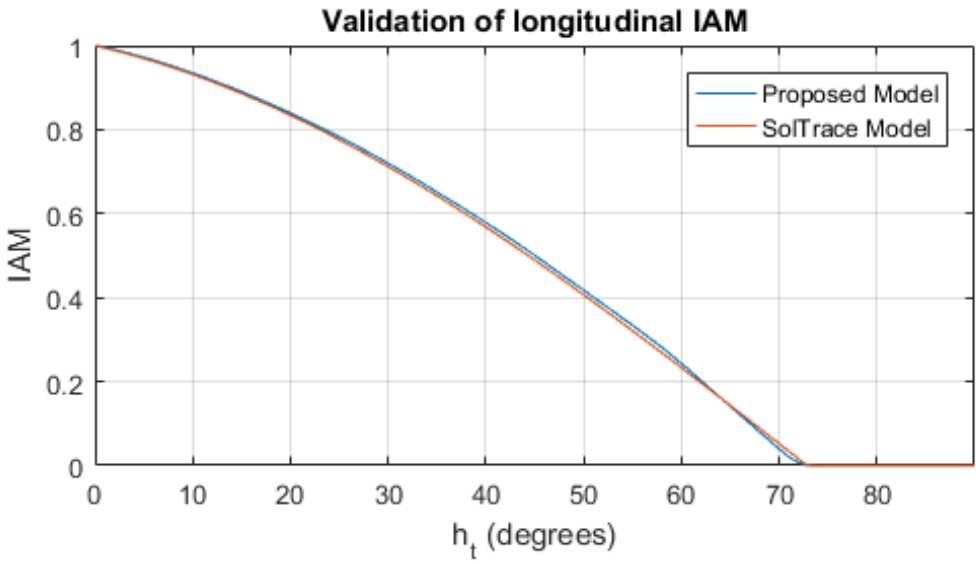

Source: The author.

presented in Figures 49 and 50. These also show similar results when comparing the transversal and longitudinal results, although it is evident that the accuracy of the proposed model seems to be smaller for small values of hour angle. This can be significant as small transversal hour angles typically represent the moments of the day with the highest solar irradiance, and in this case reached maximal deviation of 5.7% over the manufacturer's data. The oscillatory behaviour shown for transversal incidence angles smaller than 50^o is given by the absorber's shadow passing through the mirrors. As the shadow passes from one mirror to the other, the amount of irradiance on the absorber oscillates.

Figure 49 – Comparison of IAM_t from data sheet and the proposed model.

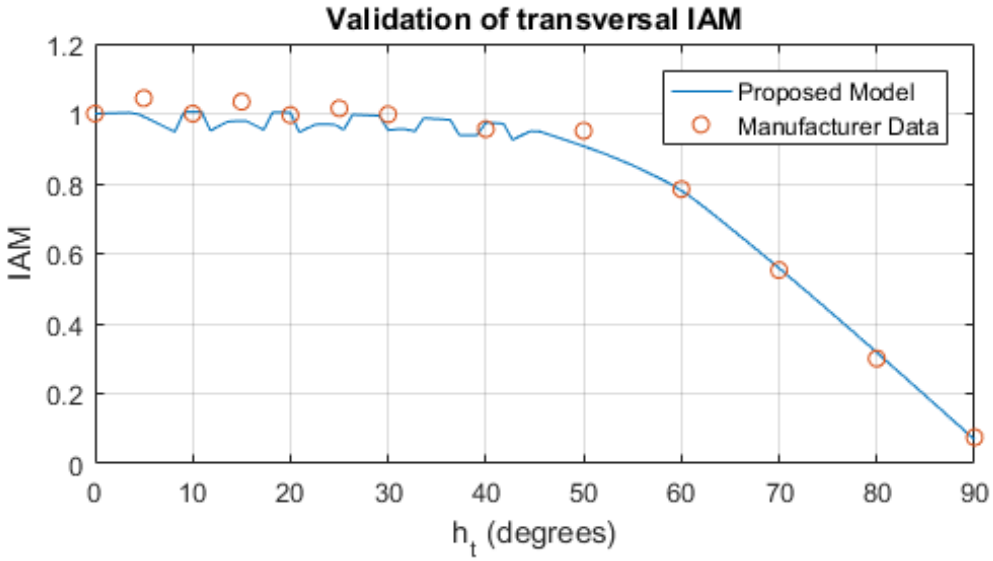

Source: The author.

Figure 50 – Comparison of IAM_l from data sheet and the proposed model.

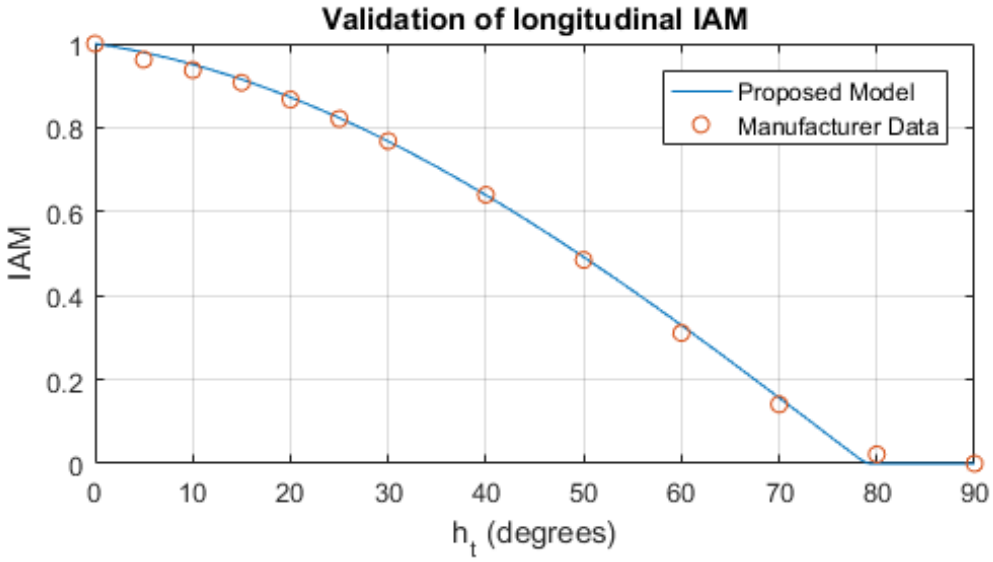

Source: The author.

4.3 SOLAR TRACKING ALGORITHMS

With the completion of the optical model, it is possible to evaluate how the Fresnel collector concentrates the incident irradiation flux on the collector's absorber. This concentration is highly dependent on how the mirrors are manipulated along the day, as the direction of the solar irradiation is always changing. Most tracking algorithms are composed of a simple logic that makes the solar ray that incides on the center of each mirror intercept the center of the absorber. The contributions of this chapter are tracking algorithms that try to maximize the energy directed to the absorber in some way while considering physical constraints. The following subsections present three strategies for solar tracking algorithms on Fresnel collectors.

To evaluate the different proposals and tracking, simulations were carried out with values of h_t referring to the path of the sun on a specific day, between 08:00 and 17:00 hours and each simulation has 100 points. The condensed DNI was constant and equal to 1000 $w.m^{-2}$.

4.3.1 Simple tracking

The simplest tracking system for Fresnel collectors is that which aims to make the sun's rays that pass through the center of the mirrors reach the center of the absorber. Figure 51 shows the desired geometry for this type of tracking of the Sun.

From the analysis of the relationships between the angles described in Figure 51, it is easy to derive an analytical expression that associates the inclinations of the mirrors (β_i) with the position of the Sun, being given by the following equation:

$$\mu_i + \beta_i + \theta_{t,i} = 90^o. \tag{87}$$

Figure 51 – Representation of simple tracking for some solar hour angle. The orange line represents the trajectory of the solar ray that is reflected at the center a mirror.

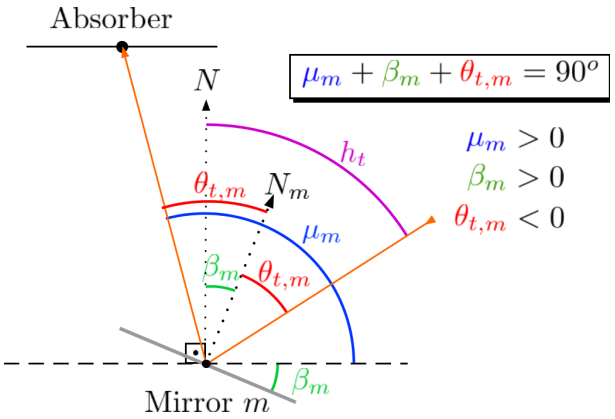

Source: The author.

Substituting $\theta_{t,i}$, calculated by Equation (4), and rearranging the terms, we arrive at a simple expression:

$$\beta_i = \frac{90^o + h_t + \mu_i}{2}. \tag{88}$$

The simplicity of this expression allows this type of tracking to be implemented mechanically, with only one actuator on all mirrors, as proposed in (PIGOZZO, 2019). The figures 52 and 53 illustrate the slopes calculated for the mirrors and the incident and reflected rays in the center of each mirror.

Figure 52 – Representation of the simple tracking for $h_t = -67.162^o$.

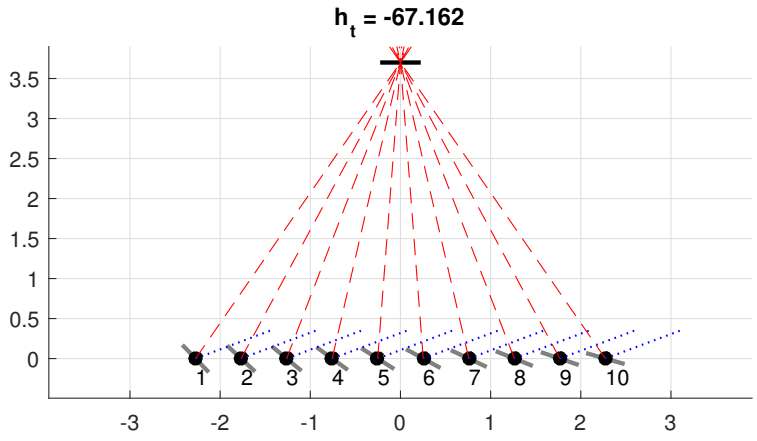

Source: The author.

Figure 53 – Representation of the simple tracking for $h_t = 13.292^o$.

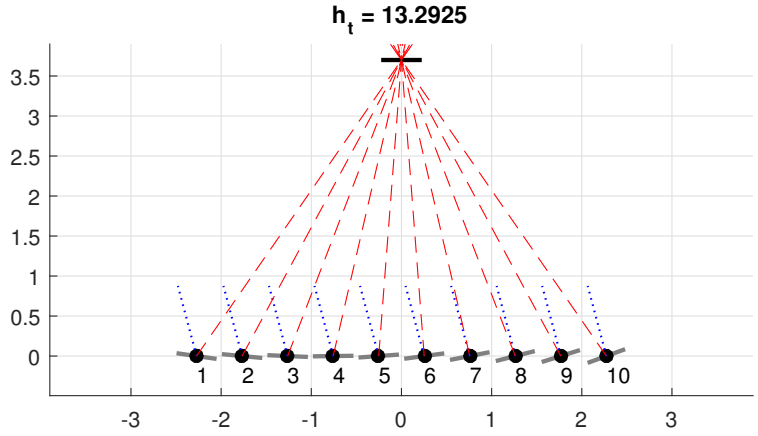

Source: The author.

Figure 54 – Illustration of two aiming strategies: (a) represents the usual aiming strategy and (b) represents an aiming strategy that makes the center of the reflected beam coincide with the center of the absorber.

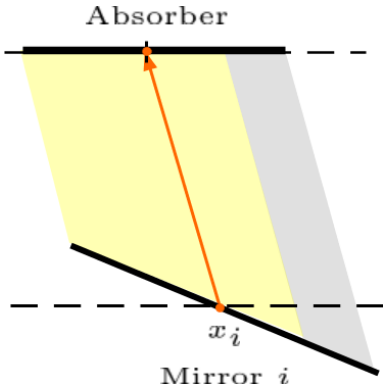

Source: The author.

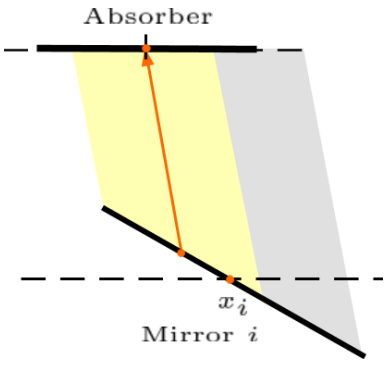

Source: The author.

4.3.2 Tracking with the center of the illuminated area

In order to make the incidence on the absorber more symmetrical, a new strategy for tracking was devised: Instead of making the rays reflected on the center of each mirror reach the center of the absorber (as illustrated on Figures 52 and 53), the new proposal is to make the center of the beams reflected on each mirror incide on the center of the absorber. This strategy is illustrated on Figure 54.

Since the proposed model already calculates the illuminated band in the absorber's plane ($x'^{abs}_{1,i}$, $x'^{abs}_{2,i}$), the calculation of the center of the illuminated region of

the absorber is given by:

$$x_i'^{abs,C} = \frac{x_{1,i}'^{abs} + x_{2,i}'^{abs}}{2}. \tag{89}$$

Since the calculation of $(x_{1,i}'^{abs}, x_{2,i}'^{abs})$ involves multiple steps and non-linearities, it is not possible to find an analytical expression that relates $x_i'^{abs,C}$ and β_i, but it is necessary to use a numerical method to obtain the mirror inclination values that take $x_i'^{abs,C}$ to zero (absorber center).

4.3.3 Tracking maximizing the absorbed solar irradiation flux

The algorithm presented here is a original proposal of this work and it's tracking objective is to maximize the solar irradiance flow in the absorber. As the flow can be calculated by the proposed model from the τ_t incidence factor, no major development is necessary to implement this calculation. In this proposal, it is necessary to formulate a highly non-linear optimization problem, which demanded the use of derivative-free solvers such as Particle Swarm Optimization (PSO) and has a high computational cost. The result of the previous proposal was used as an initial estimate for the optimization problem, in order to make the solution of the problem easier. A condensed version of the optimization problem that is solved is presented below:

$$\begin{aligned} \max_{\beta_i} \quad & \tau_t \\ \text{subject to} \quad & \tau_t = \Phi_{model}(\beta_i, h_t) \\ & \beta_i^{min} \leq \beta_i \leq \beta_i^{max} \qquad i = 1...n_{mirr} \end{aligned} \tag{90}$$

Problem (90) presents the objective to maximize the incidence factor τ_t with the manipulation of the inclination of the mirrors (β_i). In order to compute the value of τ_t, the equality constraint is imposed, where Φ_{model} represents the optical model presented in this work. The inequality constraints offer tight constraints on the inclinations of the mirrors.

4.4 COMPARISON OF THE TRACKING ALGORITHMS

The results for the simulation of the three algorithms are presented on Figure 55, where the total irradiance flux on the absorber at each simulation instant is presented. For all simulations, the irradiance was considered constant at 1000 $w.m^{-2}$ and only the solar incidence angle changes. The figure shows that the simplest aiming strategy results in similar irradiance flux on the absorber when compared with the two proposed strategies. It is noticeable that the strategies of aiming with the center of the illuminated beam and maximization of irradiance flux generate slightly higher irradiance flow in the absorber, which can also be seen on Table 4. The flattening of the curve, observed on all cases between 10:00 and 15:00 is given by the absorber's shadow passing through

the mirrors, thus diminishing the illuminated area of the mirrors, causing oscillations and a smaller flux on the absorber.

Figure 55 – Simulation results for all aiming strategies.

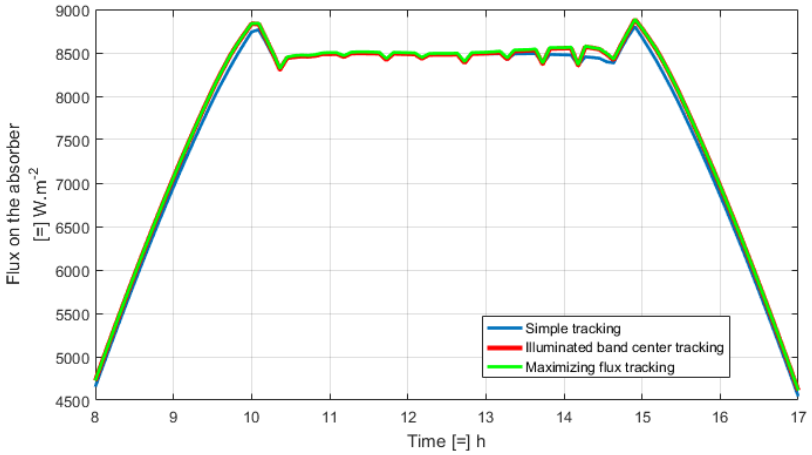

Source: The author.

	Mean time per iteration	**Summation of flux**
Simple aiming	6.74 10^{-5} *s*	100 %
Illuminated band center aiming	0.04 s	100.7 %
Maximizing flux aiming	0.42 s	100.8 %

Table 4 – Performance indicators for all evaluated aiming strategies.

Table 4 presents two parameters for comparing the results for each of the proposals: Total irradiance that intercepted the absorber's area over the simulation (shown in percentages in relation to the simple aiming strategy) and the average computation time. As expected, the first proposal has a very small computation time because it does not require computations of complex components of the collector's optical model. As expected, the proposal that maximizes the flow obtained a summation value of the flow greater than the other proposals, but not much higher.

Having the optical model and aiming strategies defined, it is now possible to study how to implement partial defocusing on Fresnel collectors. This is possible because the aiming strategy defines the inclinations of the mirrors and the proposed model is able to provide the individual contributions of each mirror to the performance of the collector. The next section presents an initial study on this regard.

4.5 DEFOCUSING STRATEGY

The proposed strategy for partial defocusing of Fresnel collectors consists on using each mirror on two possible states: following the inclination (β_i) provided by the aiming strategy (referred here as focused mirrors) or; with an inclination that minimizes it's effects on the concentration (defocused mirror). This minimal interference inclination is illustrated on Figure 56, with the variable ϱ_i, representing the focus status of each mirror i. Assuming that defocusing is occurring prevalently near noon, when the solar irradiance is at its greatest values during the day, the shading between focused and unfocused mirrors is ignored, being considered only the shading already considered on the optical model (neighboring focused mirrors).

Figure 56 – Illustration of the behaviour of a defocused mirror.

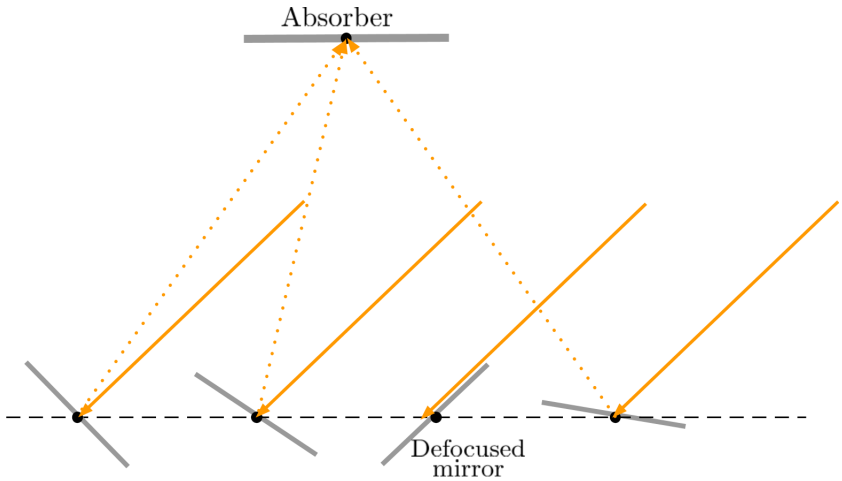

Source: The author.

With these two possible states for each mirror, an the knowledge of how much irradiance is reflected to the absorber, an algorithm can be developed to compute which combination of focused or defocused mirrors results on a desired focusing level (δ) for the whole collector. In order to implement this algorithm, it is necessary to calculate the relative incidence factor (τ_i^*) for each mirror i. This is done by Equation (91).

$$\tau_i^* = \frac{\tau_i}{\tau_t} \tag{91}$$

The values of incidence factor for each mirror and the whole collector are calculated on Algorithm 4 presented on A. The goal of the proposed defocusing algorithm is to make the current equivalent focus value of the collector ($\sum_{i=1}^{n_{mirr}} \tau_i^* \cdot \varrho_i$) be the closest to some desired focus value (δ), which can be achieved by minimizing the result of Equation (92).

$$J_{bin}^{def} = (\delta - \sum_{i=1}^{n_{mirr}} \tau_i^* \cdot \varrho_i)^2 \tag{92}$$

It can be shown that the minimization of this J is equivalent to the mixed-integer quadratic programming presented on Problem 93.

$$\begin{aligned} \min_{\varrho} \quad & 0.5 \cdot \varrho' \cdot H \cdot \varrho + f' \cdot \varrho \\ \text{subject to} \quad & \varrho_i \in [0,1], i \in [1, n_{mirr}] \end{aligned} \tag{93}$$

With

$$\begin{aligned} T &= [\tau_1^*, \tau_2^*, \ldots, \tau_{n_{mirr}}^*]' \\ \varrho &= [\varrho_1, \varrho_2, \ldots, \varrho_{n_{mirr}}]' \\ H &= T \cdot T' \\ f &= -\delta \cdot T' \end{aligned}$$

The solution of Problem 93 should yield values of ϱ_i such the equivalent focus of the collector is close to the desired. In order to evaluate this algorithm, this problem was solved for various values of transversal solar hour (h_t), for eleven desired focus values. These results are presented on Figure 57, which shows on dashed lines the desired collector focus value and in continuous lines the equivalent focus value obtained for the optimal combination of mirrors obtained on each case.

It is possible to see that, as expected, it is not possible to always obtain the precise desired focus value, as the combination of focused and defocused mirrors have a discrete and finite number of possibilities for each incidence angle. Although it is not possible to obtain exact focus values on some cases, it is noticeable that on the worst cases (e.g. $\delta_6^{ref} = 0.5$), the maximal deviation did not exceed a range of 5% deviation over the desired value. This indicates that it can be possible to implement such defocusing strategy if the structure that proposes the defocusing takes into account this level of imprecision on the actuator.

Figure 57 – Simulation results for partial defocusing of a Fresnel collector.

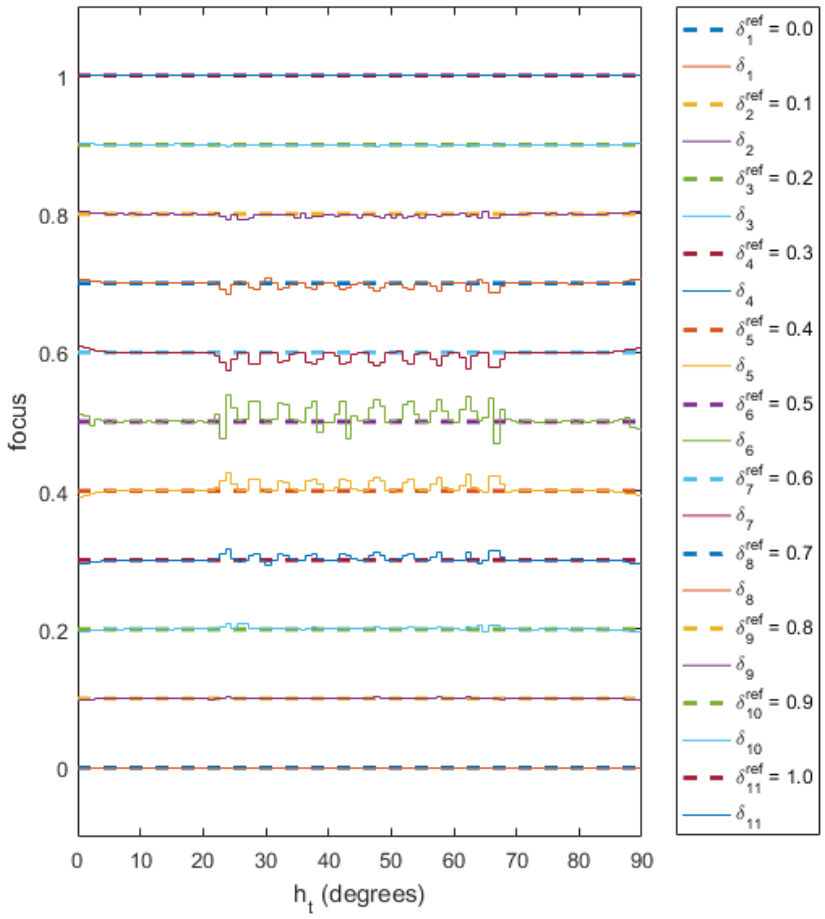

Source: The author.

4.6 FINAL REMARKS

This chapter presented an simplified optical model for a Fresnel collector, which was compared with data from a well established Ray Tracing optical modeling software and experimental data. The model was used to evaluate three different solar aiming strategies for this type of collector. The results show that the simple aiming algorithm has a good performance even when compared with more complex proposals. Further study is necessary for assessing if these new proposals, such as maximizing irradiation distribution over the absorber, will have effects on the long term durability of the absorber. This chapter also evaluated a possible algorithm for computing partial defocusing on Fresnel collectors. The model and tracking algorithms presented allow for future works with predictive controllers that manipulate the collector's mirrors to control the temperature of the thermal fluid. This is possible because the model presents data on the contribution of each mirror to the overall performance of the collector. In order to implement this strategy, it appears that the model should not be directly Incorporated

on the controller's prediction model, as the nonlinearities of the optic characteristics of the system introduce much complexity for a optimization solver that is supposed to be executed in real-time. The hierarchical concept appears as and interesting option for control structure, which involves a higher-level master controller that determines the focus value and a lower-level optimization problem that calculates the inclination of the mirrors given the desired focus. This concept is explored in the next chapter.

5 CONTRIBUTION: MPC WITH OPTICAL COLLECTOR MODEL

In Chapter 4 it was proposed a simplified model for the concentration ratio of the controller to be used on defocusing computations but it was not incorporated into a control structure that defines the amount of necessary defocusing. This chapter presents a control structure for defocusing control of Fresnel collectors that considers how the collector implements the defocusing and analyzes some possible performance issues that may arise from the incorporation of solar tracking manipulation on the sampling time of the proposed MPC controller. The proposed control structure incorporates the optical model of the fresnel collector on an intermediary layer between the MPC and the collector's mirror's actuation, thus separating the problem of defining the amount of defocusing to be applied and the computation of each mirror's inclination angle, given the solar position and the desired defocusing value. Thus, the main contributions of this chapter are:

- A new control structure is proposed for the solar collector system, based on a two-layer nonlinear MPC strategy;
- An optical model is used in the control structure to design a control law that achieves the desired defocus;
- A sensitivity analysis for the defocusing structure is performed;
- Simulations are performed considering a Ray-Tracing optical model of the Fresnel collectors.

The rest of this chapter is divided as follows: Section 5.1 describes the CSP field, the fresnel collector, and the models utilized. Section 5.2 describes the two Model Predictive Control structures used in this work. Section 5.3 describes the solar aiming and the defocusing strategy utilized to implement the desired defocus level proposed by the controllers. Section 5.4 presents the simulation results in closed loop for the proposed controllers and the tracking error analysis.

5.1 SOLAR THERMAL FIELD AND FRESNEL COLLECTOR

Each fresnel collector, as seen in Chapter 2, is composed of a reflector that focuses the sun irradiation on an absorber tube. Inside the absorber tube, a Heat Transfer Fluid flows through the collector loop and receives the thermal energy from the absorber tube. The amount of energy that the HTF has at the output of the loop is directly related to the amount of solar irradiation at the reflectors, which is both the main source of energy for the process and its main disturbance. Typical control structures only manipulate the HTF flow as it changes the amount of energy absorbed per unit

of time, but the defocusing of the reflector mirrors introduces a degree of freedom to the control structure and allows for a faster actuation for lowering the HTF temperature (MACHADO et al., 2022).

This work considers two models for the fresnel collector. The first is presented in detail in Chapter 4, which consists of a simplified optical model built on Matlab that, given the solar position angles (h_t and h_l) and the mirrors' inclination angles (β), provides the irradiance flux on the collector's absorber (I_{abs}), as illustrated by Equation (94). This model is used to compute the inclination of the mirrors that implement the desired focus value. It has low computational complexity, allowing its use on optimization problems in real-time. How to obtain the mirrors' inclinations on the presence of defocusing while tracking the sun will be presented in section 5.3 of this work.

$$I_{abs}(t) = f_{model}(h_t(t), h_l(t), \beta(t)) \tag{94}$$

The second model considered is developed on SolTrace software (WENDELIN, 2003), which uses Ray-Tracing technology to obtain the same output as the first model. This second model is more accurate and is used as the actuator on the MPC simulations performed in this work. It is also used to evaluate the errors due to the discrete actuation of the tracking algorithm, as will be presented later. Differently from the previous optical model, the SolTrace model is not built directly with equations but is created by providing a geometric description of the collector, which substantially increases the computational effort in order to evaluate the model. This increased computational cost makes this kind of model impractical for Real-Time applications with relatively small sampling time, such as MPC or other optimization-based algorithms.

Both the Matlab and SolTrace models are parametrized with the the collector's number of mirrors (n_{mirr}), length (C_{mirr}) and width (L_{mirr}) of the mirrors, length (C_{abs}), width (L_{abs}) and elevation (E_{abs}) of the absorber, and also the distance between mirrors (d_{mirr}). The azimuth angle of the central axis of the collector is also considered. The solar thermal field considered in this work is composed of n_c fresnel collectors associated in series, composing a collector loop, and these n_l loops are configured parallel to each other. The resulting HTF flow from all the parallel loops gives the total flow for the solar field and the temperature at the output of the field (T_{out}^{field}) is affected by the output temperature of each loop.

The model utilized in this work to represent the heat exchanges that occur in the solar field is a lumped parameter model for each collector is the one described in Chapter 2, expressed in Equation (5).

The output temperature of the field is modeled with a weighted average of the output temperatures of each loop, using the volumetric flow rates, as expressed on Equation (95).

$$T_{out}^{filed}(t) = \frac{\sum_{i=1}^{n_p} T_{out,i,n_c}(t) v_i(t)}{\sum_{i=1}^{n_l} v_i(t)} \tag{95}$$

5.2 OPTIMAL CONTROL OF SOLAR FIELD WITH DEFOCUSING

The proposed control structures aims to manipulate the HTF flow within its operational limits in order to achieve the reference for the output temperature for the solar field. The controllers should defocus the solar collectors when the maximum HTF temperature is to be reached in a predictable future horizon while considering the future reference value for the HTF temperature and the disturbances of ambient temperature, irradiation, and inlet temperature. This control structure is described in Figure 58.

Figure 58 – Diagram of the proposed control structure for a generic solar field. The outputs of the MPC are only shown for loop 1 for simplicity but are present on all loops and collectors.

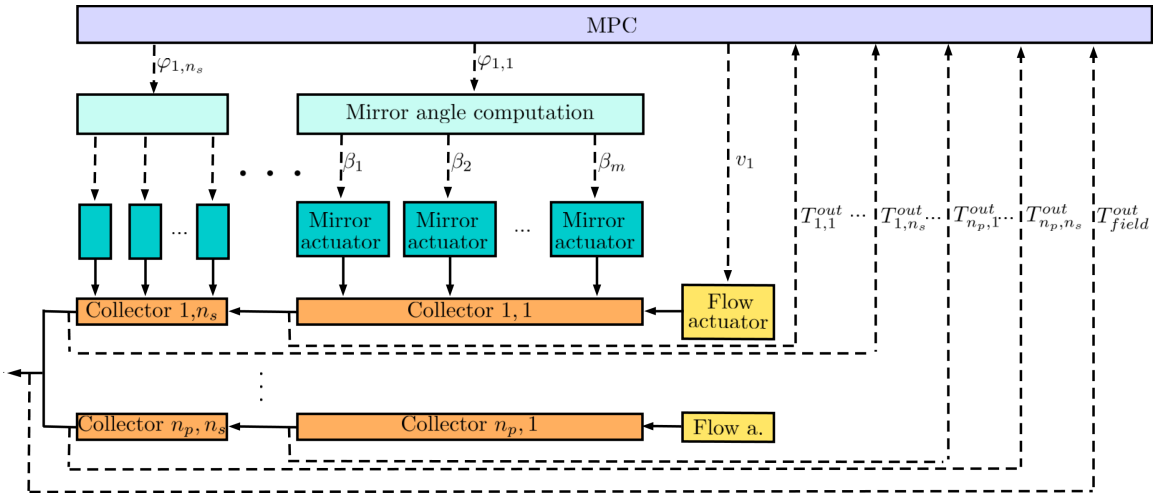

Source: The author.

The MPC controller solves an optimization problem that yields values for the HTF flow (v_i) and focus ($\varphi i,j$) which are passed down to some actuation structure. The actuators for the flow are not explicitly modeled on this work as it is assumed that these have fast actuation given the sampling time of the controller. The focus values obtained for each collector are passed to an intermediary layer between the MPC and the mirror's actuators. Given the desired focus value, this layer will calculate the angular position of each mirror on the respective collector while considering the solar tracking. The procedure for computing these mirror inclination angles is detailed in section 5.3 and considers the optical model described in Chapter 4. In summary, the MPC controllers used in this work measure all the collectors' output temperatures, manipulate the flow on each loop and focus level on each collector of the field.

In the scope of this work, two nonlinear model predictive control were considered, referred to as NMPC and PNMPC, and are described in the following sections.

5.2.1 Nonlinear Model Predictive Control (NMPC)

The first proposal is to use the nonlinear process model directly as the prediction model of the MPC controller, as shown in Chapter 2 in problem (96) (here repeated):

$$\min_{u} \sum_{k=1}^{H_p} J_d(x(k), u(k)), \tag{96a}$$

Subject to

$$x(k+1) = f_d(x(k), u(k)), \qquad k \in [0, H_p - 1], \tag{96b}$$
$$x(k) \in \mathscr{X}, \qquad k \in [1, H_p], \tag{96c}$$
$$u(k) \in \mathscr{U}, \qquad k \in [1, H_c]. \tag{96d}$$

Where H_p is the prediction horizon, H_c the control horizon, f_d the dynamic model of the process, x_k are the predicted variables and u_k the manipulated variables. For the solar field control, this work considers the manipulated variables as the flow on each loop i ($v_i(k)$) and the focus value on collector j of loop i ($\delta_{i,j}(k)$), thus u_k is given by:

$$u_k = \left[v_1(k), v_2(k), ..., v_{n_p}(k), \delta_{1,1}(k), ..., \delta_{1,n_c}(k), ..., \delta_{n_p,n_s}(k) \right]^T$$

The predicted variables for this controller are the output temperatures of each collector and the effective focus applied on the collector, given the actuation dynamics:

$$x(k) = \Big[T_{out,1,1}(k), T_{out,1,2}(k) ..., T_{out,1,n_s}(t), ... T_{out,n_p,n_s}(t), \\ \delta_{out,1,1}, \delta_{out,1,2}, ..., \delta_{out,1,n_s}, ... \delta_{out,n_p,n_c} \Big]^T$$

The cost function J_d (as seen on Equation (25)) has terms penalizing three aspects of the process: the tracking error for the reference of the output temperature of the field (T_{ref}), as seen on Equation (26a); the discrepancy between the flow and focus value to their respective maximal values (v^{max} and 1 respectively), as seen on Equation (26b); and the movements of the manipulated variables, as seen on Equation (26c).

With:

$$\Delta v_i(k) = v_i(k) - v_i(k-1), \qquad k \in [1, \ldots, H_c],$$
$$\Delta \delta_{i,j}(k) = \delta_{i,j}(k) - \delta_{i,j}(k-1), \qquad k \in [1, H_c].$$

The constraints (96c) and (96d) define relevant constraints on the manipulated and controlled variables, such as lower and upper limits for the flow, focus, and temperatures. It is also considered an upper limit for the sum of the flows of all loops. These constraints are expressed in equations (98), considering $i \in \{1, ..., n_p\}$ and $j \in \{1, ..., n_s\}$.

$$T^{min} \leq T_{out,i,j}(k) \leq T^{max}, \qquad k \in [1,...,H_p], \tag{98a}$$
$$0 \leq \delta_{i,j}(k) \leq 1, \qquad k \in [1,...,H_c], \tag{98b}$$
$$v^{min} \leq v_i(k) \leq v^{max}, \qquad k \in [1,...,H_c], \tag{98c}$$
$$\sum_{i=1}^{n_l} v_i(k) \leq v^{max,field}, \qquad k \in [1,...,H_c]. \tag{98d}$$

The MPC formulation presented in (96) is classified as a Nonlinear Programming (NLP) problem, which can be challenging to solve. One of the control proposals of this work is to use directly this kind of implementation, and the controller will be called nonlinear MPC (NMPC) This proposal utilises Multiple Shooting in order to compute the predictions during the optimization. The second proposal consists of a transformation of the NLP problem described by (96) through linearization of the prediction model at each execution of the controller and also considering the focus variable $\delta_{i,j}$ as an integer, representing fixed levels of possible focus values. This second proposal denominated Practical Nonlinear MPC (PNMPC) is described in the next section.

5.2.2 Practical Nonlinear Model Predictive Control (PNMPC)

The PNMPC controller used in this section is the partial defocusing controller proposed by Elias et al. (2018) and that was used in Chapter 3. It uses integer variables to model the partial defocusing of the collector in intervals of 10% and solves a Mixed-Integer Quadratic Programming (MIQP) problem at each sampling time. The following section presents details of the layer that computes the angles of the collector's mirrors given the desired focus value $\delta_{i,j}$ and the solar angle h_t. The tuning parameters for the controllers are presented in Table 5.

Table 5 – Tuning parameters of the controllers.

	Q_T	Q_v	Q_φ	R_v	R_φ
NMPC	10	1e4	1e2	1e2	1
PNMPC	1e-5	1e-3	0.1	1	1e2

5.3 DEFOCUSING STRATEGY

In order to describe the defocusing strategy, it is important to understand how the solar tracking is usually made, considering the collector is completely focused. The most simple tracking strategy consists of making the solar ray that would be reflected in the center of the mirror hit the center of the absorber, as described in Section 4.3.1 and illustrated in Figure 51.

Notice that, independently from the transversal projection of the solar hour angle (h_t), the angle between the reflected solar ray and the horizontal plane that passes through the centers of all the mirrors (μ_m) does not change. This angle μ_m is only dependent on the geometry of the collector, and more specifically, depends on the elevation of the absorber (E_{abs}) and the position of the mirror with respect to the absorber's position on the horizontal plane. For a given value for the inclination of mirror m ($\beta_m^{100\%}$) and a sun position angle h_t, it is possible to obtain the transversal incidence angle ($\theta_{t,m}$) of the solar rays on the mirror. This incidence angle is given with respect to the normal vector of the mirror, represented by N_m in Figure 51.

Through some trigonometric analysis of the angles when performing the solar tracking, as seen in Section 4.3.1, it is possible to arrive at a simple expression that defines the interactions of these angles in this case, as expressed on Equation (99). Therefore, it is very simple to compute the angle for all n_{mirr} mirrors of each collector given the solar position (h_t) and the geometry of the collector (μ_m).

$$\beta_m^{100\%} = 45^o - \frac{h_t + \mu_m}{2} \tag{99}$$

The proposed strategy for partial defocusing of Fresnel collectors consists of changing the focal point for the fresnel collectors, in such a way that the amount of irradiance incident on the absorber is equivalent to the percentage defined by the defocus value ($\delta_{i,j}$), with respect to the amount of irradiance that the absorber receives when operating the solar tracking with complete focus. This procedure is exemplified by Figure 59, where L represents the elevation of the new focal point under the absorber.

Figure 59 – Illustration of the defocusing strategy on the collector.

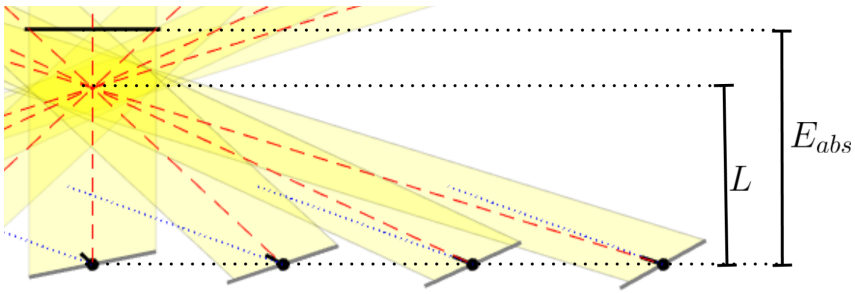

Source: The author.

The change in the focal point can be incorporated into the tracking algorithm by replacing μ_m on Equation (99) with a new angle μ_m^*, such that the reflected rays intercept at height L. This new μ_m^* is given by equation (100).

$$\mu_m^* = \arctan\left(\frac{L.\tan(\mu_m)}{E_{abs}}\right) \tag{100}$$

Thus, given the desired focus elevation L and the solar angle h_t, it is possible to compute the inclination angles for all the collector's mirrors, as presented on Equation

(101).

$$\beta_m^* = 45^o - \frac{h_t + \mu_m^*}{2} \tag{101}$$

Although helpful, Equation (101) is not sufficient to implement the defocusing strategy, as the MPC controllers provide focus values ($\delta_{i,j}$) in percentages and do not directly provide the elevation for the new focal point. It is possible to incorporate the computation of the elevation L directly into the MPC controllers, but this would introduce even more nonlinearities on the controller, making it more challenging to run the control structure in real-time, without evident benefits to the performance of the control.

This work proposes that in order to obtain the elevation that implements the desired focus value, the model proposed by (BRANDÃO; COSTA MENDES; NORMEY-RICO, 2022) (and here presented in generic form in Equation (94)) coupled with the tracking algorithm expressed in Equation (101) can be used to provide the correlation between the percentual focus value given by an elevation L, expressed as $F(h_t, L)$ and the desired focus value, generically expressed as F^{ref}. Thus, for the NMPC, $F^{ref} = \delta_{i,j}$, while for the PNMPC controller $F^{ref} = \delta_{i,j}/10$.

In order to compute the focus value as a function of h_t and L, it is necessary to first obtain the irradiance at the absorber considering 100% focus ($I_{abs}^{100\%}$), which is done by evaluating Equation (94) with the $\beta_m^{100\%}$, obtained by Equation (99), as seen on equation (102).

$$I_{abs}^{100\%} = f_{model}\left(h_t, \beta_m^{100\%}\right) \tag{102}$$

Then, it is possible to compute the irradiance at the absorber for a given value of elevation L (I_{abs}^*) with equation (103).

$$I_{abs}^* = f_{model}(h_t, \beta_m^*(h_t, L)) \tag{103}$$

At last, the focus value obtained with the elevation L can be obtained by dividing the irradiance level given L, by the irradiance level for complete focus, as expressed by equation (104).

$$F(h_t, L) = \frac{I_{abs}^*}{I_{abs}^{100\%}} \tag{104}$$

Now, it is only necessary to find which value of L results in the obtained focus value $F(h_t, L)$ to be equal to the reference focus F^{ref}. This can be implemented with many root-finding numerical methods, but as the proposed defocusing strategy requires that the new focus elevation to be under the absorber, it is necessary to incorporate this constraint on the solution, resulting in the optimization problem (105).

$$\min_L \left(F^{ref} - F(h_t, L)\right)^2 \tag{105a}$$

Subject to

$$0 \leq L \leq E_{abs} \tag{105b}$$

The structure of this optimization problem is also illustrated by Figure 60, which shows the main components of the problem and how they interact to obtain the value of elevation L that implements the desired focus value.

The reference optical models which are commonly used to design from solar collectors to whole CSP fields are based on Ray-Tracing techniques. These models use the Monte Carlo method to simulate solar ray paths and compute their trajectory while reflecting on mirrors and hitting opaque barriers, such as the absorber. Although it is desirable to use the Ray-Tracing models to solve the optimization problem, it is not practical as these models have relatively *high computation times* and the topology of the cost function has several local minima and maxima, therefore it is necessary to use heuristic techniques, such as Particle Swarm Optimization, in order to obtain a solution. These heuristic techniques require large amounts of calls to the objective function and to the Ray-Tracing model, making it impractical for real-time applications. Solving with SolTrace takes approximately 44 seconds per sample, which is impractical considering the sampling times of (SÁNCHEZ et al., 2018) and (ARAÚJO ELIAS et al., 2019) (30 and 6 seconds respectively). It would be necessary 22 days for computing the 44260 points mapping used later in this thesis.

The optical model proposed in Chapter 4 arises as a second option for this approach, as it has a small computational cost and was validated with SolTrace for solar tracking.

With the description of the defocus strategy complete, the following section presents some simulations and analysis regarding the studied MPC controllers and the effects of different kinds of errors on the defocusing strategy.

Figure 60 – Detailing of some of the collector's parameters.

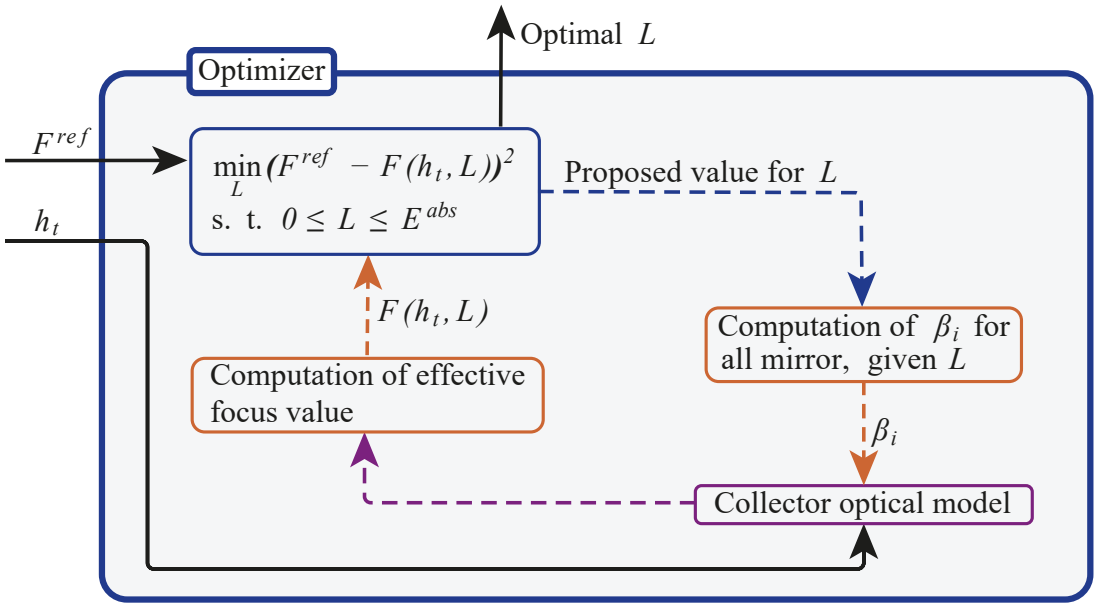

Source: The author.

5.4 RESULTS AND DISCUSSION

In order to compare the MPC described in section 5.2, the controllers were incorporated into a Matlab simulation that implements the structure present in Figure 58. The dynamic model and computation of the mirror's angles are all performed in this Matlab simulation, but in order to consider possible errors in the optical model proposed by (BRANDÃO; COSTA MENDES; NORMEY-RICO, 2022), which is used to compute the mirror's angles, this work also incorporates on the process model a ray-tracing model of the solar fresnel collector built on the SolTrace software. The organization of this simulation structure is presented in Figure 61, where it is possible to observe the inputs and outputs of the MPC controllers, the mirror angle computation layer, the SolTrace optical model, and the dynamic model of the collector.

The SolTrace model is used to calculate the effective focus value $\overline{\delta}_{i,j}$ that is to be applied to the dynamic model, and is considered to be more accurate than the focus value obtained considering the (BRANDÃO; COSTA MENDES; NORMEY-RICO, 2022) model, as it does not rely on approximations of geometric equations. Both MPC controllers are evaluated with this structure and are subjected to irradiance ($I(t)$) and ambient temperature ($T_a(t)$) signals as presented in Figure 62, which represents a cloudy day with high irradiation. The evaluated controllers have a sampling time of 6 seconds and the simulation runs for $N_{sim} = 2004$ iterations, resulting in 3.34 hours of simulated time. The solar transversal hour angle (h_t) was considered starting at -52^o and ending at 0.3380^o, emulating operation starting from 09:00 until 12:20.

Four quantitative performance indices were considered in order to evaluate the controllers, these being the mean computation time for each iteration of the controllers,

Figure 61 – Representation of the main structures involved in the simulations for evaluating the performance of the proposed MPC controllers.

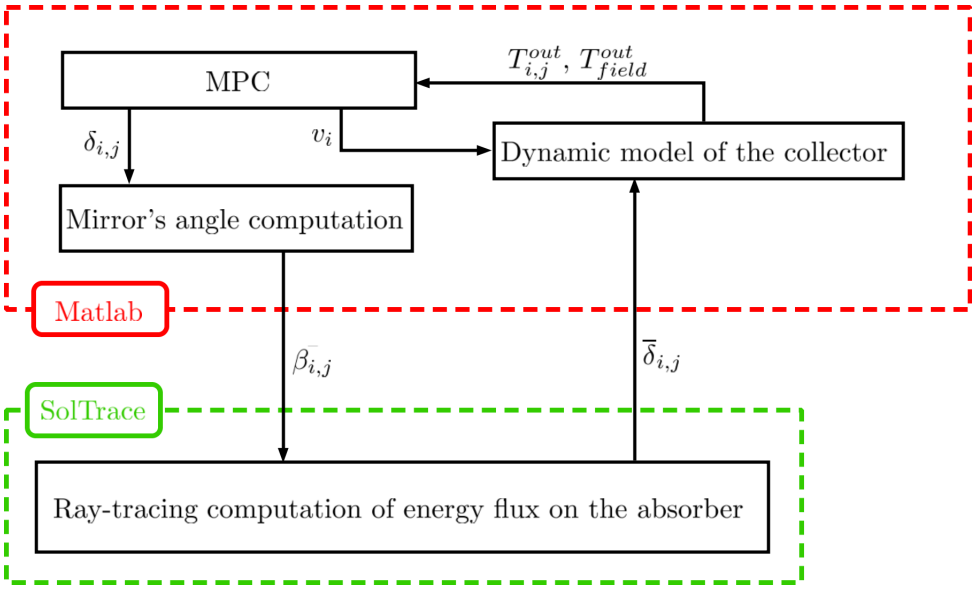

Source: The author.

the standard deviation of the same time data, and the integral set-point tracking error, defined by equation (106).

$$IAM = \sum_{k=1}^{N_{sim}} (T_{out}^{field}(k) - T_{ref}(k))^2 \tag{106}$$

The graphical results of these simulations are presented in Figure 63 for the PNMPC case and in Figure 64 for the NMPC case. It is possible to observe that the NMPC controller maintains the output temperature of the solar field more closely to the reference value of 295^oC, but also presents more oscillatory behavior for the manipulated variables. This excessive movement of the focus actuator can damage the equipment if present for long periods of time and can become a relevant issue. As the PNMPC controller can only apply defocusing action on 10% steps, it has more difficulty lowering the temperature when the flow value has already reached its upper limit but the temperature increase is not large. This shows that both strategies are capable of safely operating the process (as none of the controllers caused the temperature to surpass the upper limit of 300^oC), but the NMPC controller allowed for tighter reference tracking.

Although the graphical results may indicate a clear advantage for the NMPC controller, when analyzing the quantitative indices, presented in table 6, it is possible to note that the PNMPC controller presents a smaller and more consistent execution time, indicated by the smaller values of mean and standard deviation. This is due to the fact that solving the nonlinear optimization problem is more challenging and the computation time can vary greatly as the convergence can require more iterations in

Figure 62 – Irradiation and ambient temperature profiles considered for the simulations.

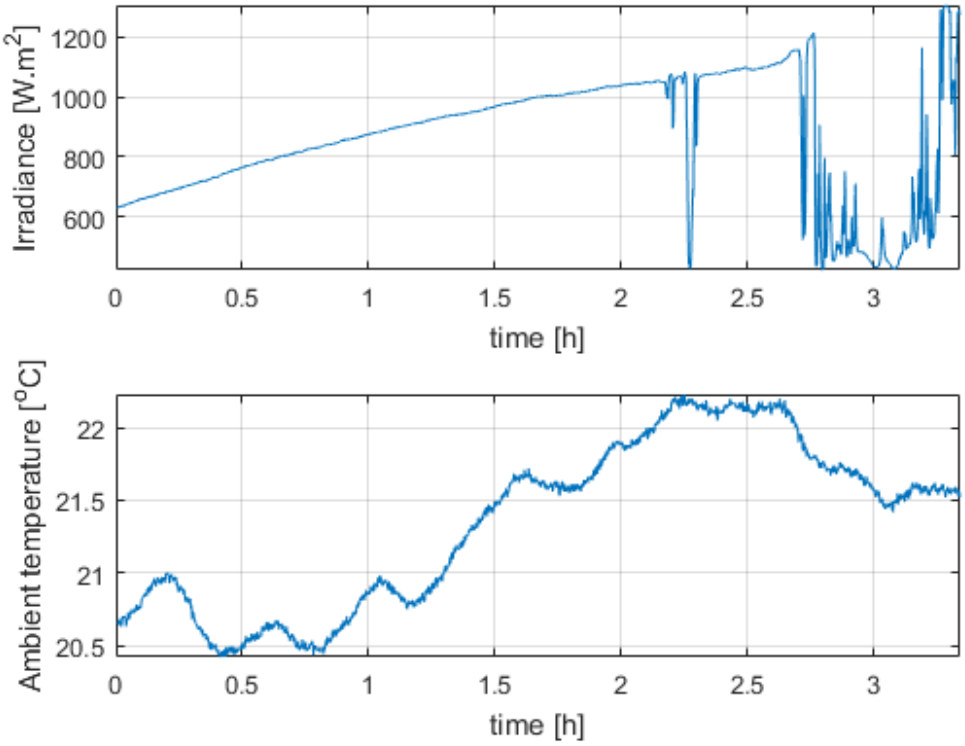

Source: The author.

Table 6 – Performance indices for the MPC simulations.

	PNMPC	NMPC
Generated Heat [*J*]	5.6880e+04	5.6824e+04
IAM	2.8719e+04	1.4769e+04
Average computation time [s]	0.0726	2.7266
Standard deviation of computation time [s]	0.0689	3.5431

certain situations.

It is also noticeable that the amount of thermal energy absorbed by the HTF is greater in the PNMPC case. This is due to the increase in the temperature in the high irradiation scenario when the HTF flow is at its upper limit, resulting in more energy being absorbed. Although absorbing more energy is desirable, it is important to note that this increase is obtained with temperature values very close to the upper limit. This index must be observed together with the IAM, as it indicates how well the controller is following the desired operational temperature.

5.4.1 Analysis of solar aiming and mirror inclination errors

Although inherently able to handle model uncertainties, the MPC controllers can be very affected in the presence of significant modeling errors. This section analyses the effects of errors in the values of solar angles and mirror inclination on the effective

Figure 63 – Results for the simulation with the PNMPC controller.

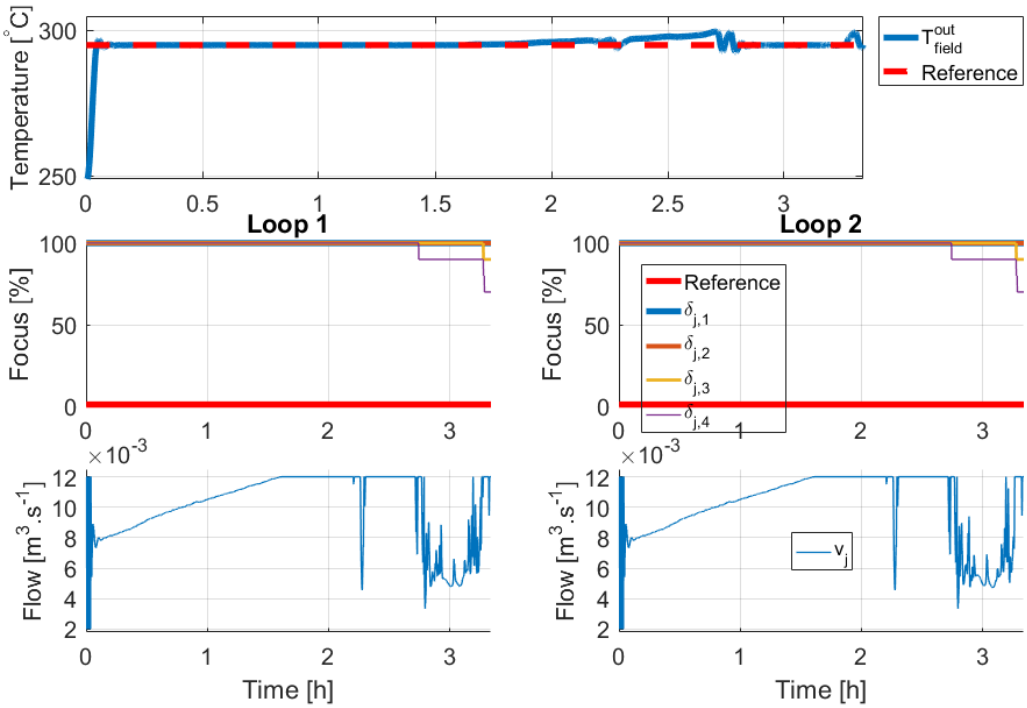

Source: The author.

focus value that affects the collector. This analysis was performed in three ways:

- Mapping the correlation between focal point elevation (L), solar hour angle (h_t), and desired focus value;
- Evaluating the effective focus resulting from the error in h_t that results from the sampling time of the control system;
- Evaluating the effective focus resulting from errors in the inclination of the collector's mirrors (β_i).

The mapping of the correlation between elevation, hour angle, and focus was performed by executing the defocus algorithm illustrated by Figure 60 for combinations of $h_t \in [0^o, 90^o]$ and $F^{ref} \in [0\%, 100\%]$. This mapping is presented in Figure 65, which allows the visualization of the highly nonlinear behavior of the defocusing implementation. It is also noticeable that for values of transversal solar hour angle h_t near 90^o (which usually represent sunset and sunrise situations), and focus values smaller than 10%, the solution seems degraded.

The behavior for high values of h_t can be explained by the optical model considered, which does not account for all shading between mirrors on these solar angles, but can be seen as acceptable when considering that a well-positioned collector will only be exposed to these solar angles at times when the solar field is not operational.

Figure 64 – Results for the simulation with the NMPC controller.

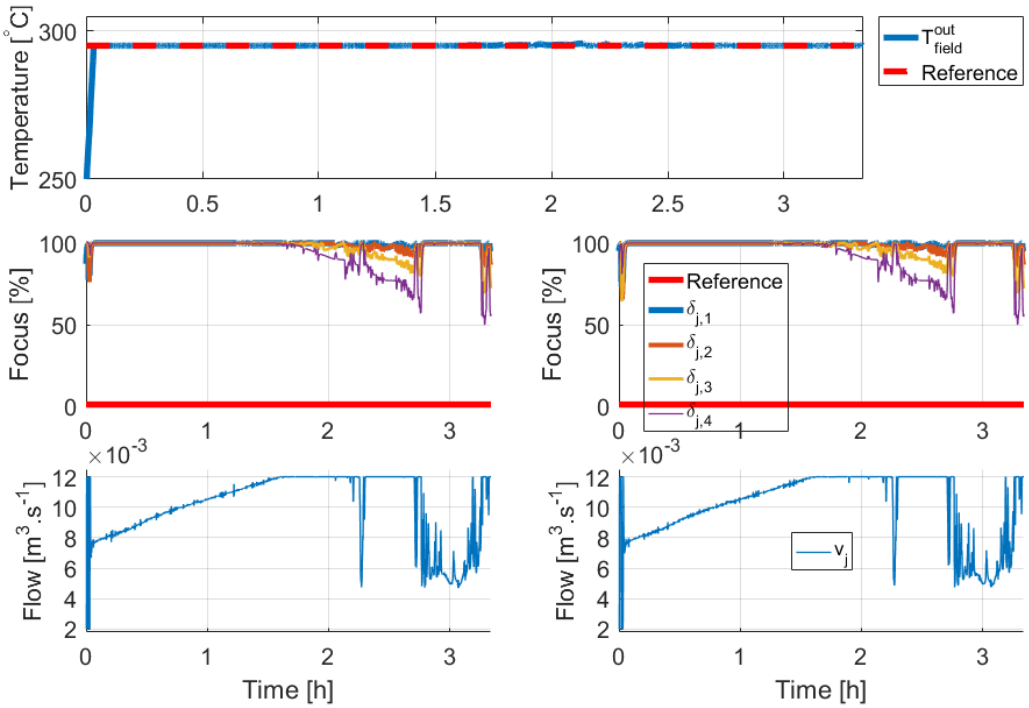

Source: The author.

The behavior for small values of focus is due to the effect of an odd number of mirrors on this solar aiming strategy. Having a centralized mirror implies that, independent of the proposed focal point elevation, the central mirror will always reflect upward, towards the absorber, as seen in Figure 66, which impossibilities defocusing of the collector for values equivalent to less than the energy reflected by this central mirror. This is a limitation of this simple defocusing strategy for the case with an odd number of mirrors. This limitation can be overcome by changing the defocusing strategy when only the central mirror is illuminating the absorber.

In order to improve the visualization of the behavior of the defocusing strategy on cases without this degraded result, Figure 67 presents the same defocusing data, but only for $h_t \in [0^o, 60^o]$ and $F^{ref} \in [10\%, 100\%]$. This range of values for the solar angle and focus value was also used in the next results presented in this work, and the values presented in Figure 67 were considered as references for the other analysis.

The next analysis consisted of running the defocus algorithm of Figure 60 for values of h_t added 0.022^o, which is approximately the transversal angular displacement of the sun for the sampling time of the controllers. These results are shown in Figure 68, which also shows the reference results considering no error on h_t. In Figure, the respective point with and without error is connected by a colored line to illustrate the magnitude of the impact of this error on the effective focus value that was obtained. The faint presence of the lines in Figure 68 shows the small scale of the impact of this

Figure 65 – Mapping of the defocus strategy with respect to solar angle, defocus value, and elevation of the focal point.

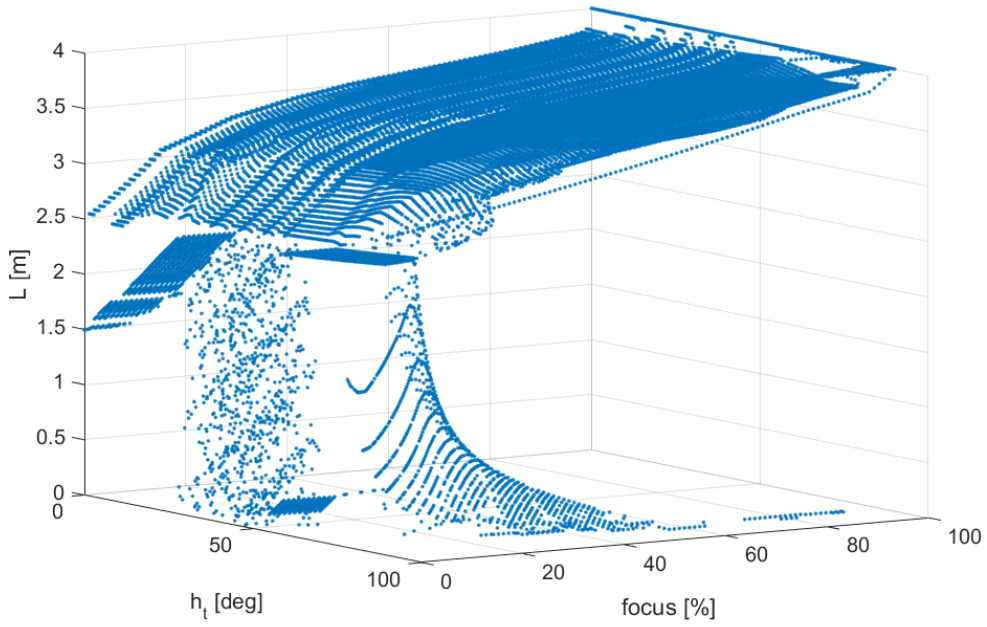

Source: The author.

Figure 66 – Defocusing case with an odd number of mirrors.

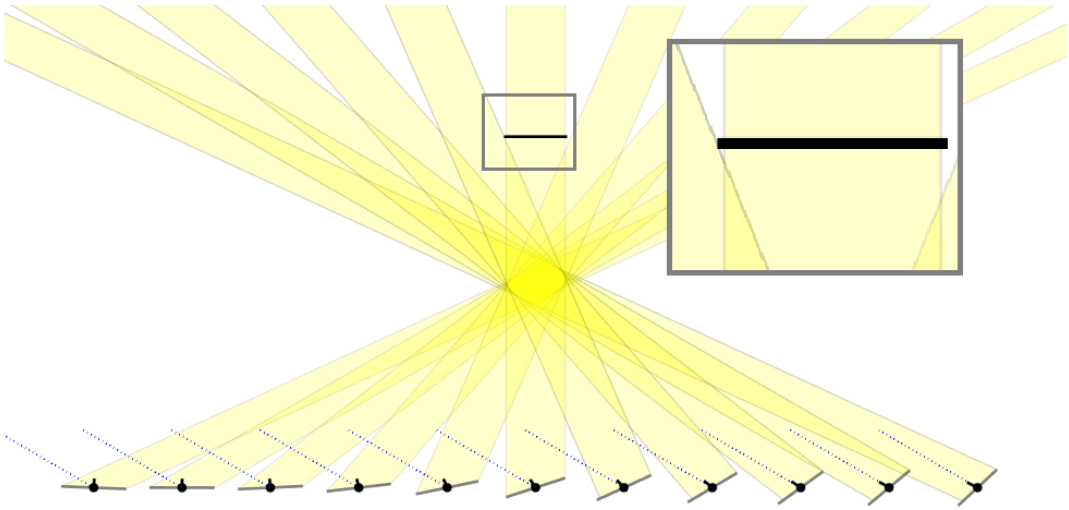

Source: The author.

sampling-induced tracking error, which was not greater than 0.1% for all considered points, indicating that the sampling time is appropriate.

With the effects of tracking errors due to the sampling time analyzed, the last evaluation of this work consists of introducing an error on the mirror's angles $\beta_{i,j}$ and verifying the effective focus value. Similarly to the previous case, the points representing the error on β_i are connected by a line to the reference value in order to accentuate the effect on the equivalent focus. For Figure 69, it was considered variations of $\pm 0.05^o$ on

Figure 67 – Mapping of the defocus strategy with respect to solar angle, defocus value, and elevation of the focal point, for a region without degenerate optimization results.

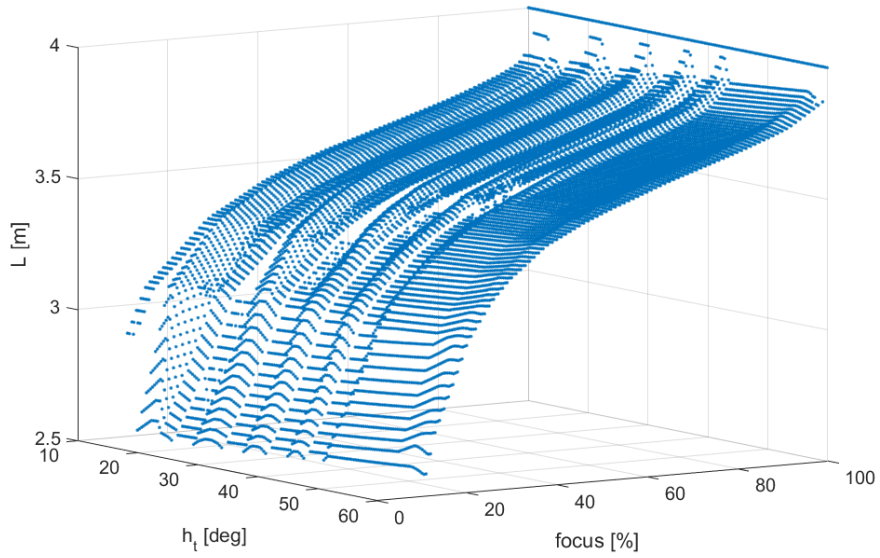

Source: The author.

Figure 68 – Results for evaluation of tracking error due to sampling time of the tracking structure.

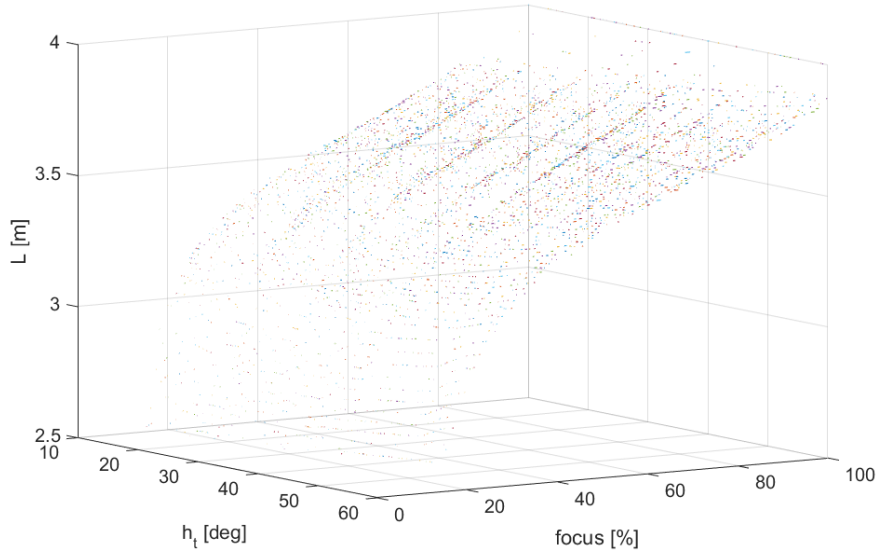

Source: The author.

all $\beta_{i,j}$ of the collector. The results show more representative errors, that in the worst case resulted in 1.3% variation on the focus value, which can still be considered to have a small impact on the performance of the defocusing control. The results of figures 70 and 71 show the effects of an error of 0.5^o in the mirror inclination angles. These latter results evidentiate that even relatively small errors for $\beta_{i,j}$ can result in important inconsistencies on the effective focus value, resulting in deviations as high as 18%

Figure 69 – Results for evaluation of effective focus discrepancy for variations of $\pm 0.05^o$ on the mirrors inclination angles.

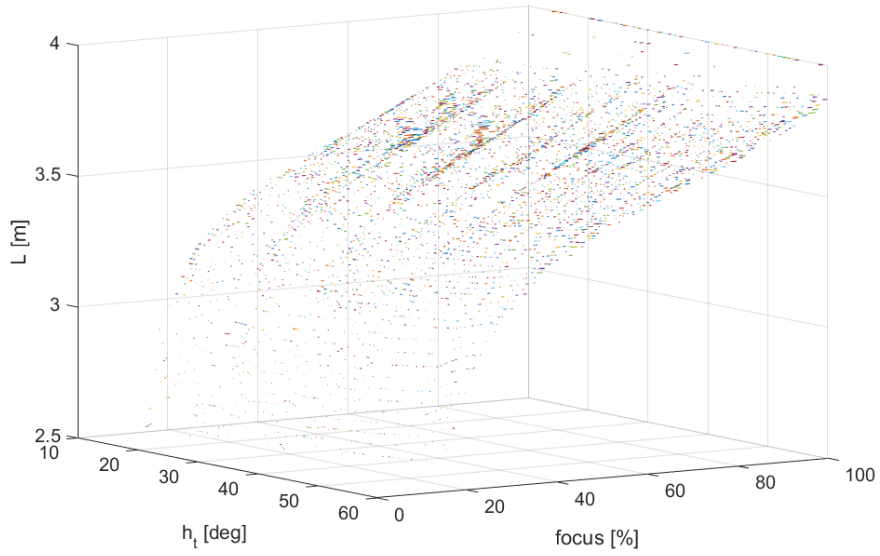

Source: The author.

in this case. The observation of the figures also allows noticing that the effect of the different errors considered in this work is highly nonlinear. These errors have more impact on the vicinity of some specific values of h_t.

Figure 70 – Results for evaluation of effective focus discrepancy for variations of 0.5^o on the mirrors inclination angles.

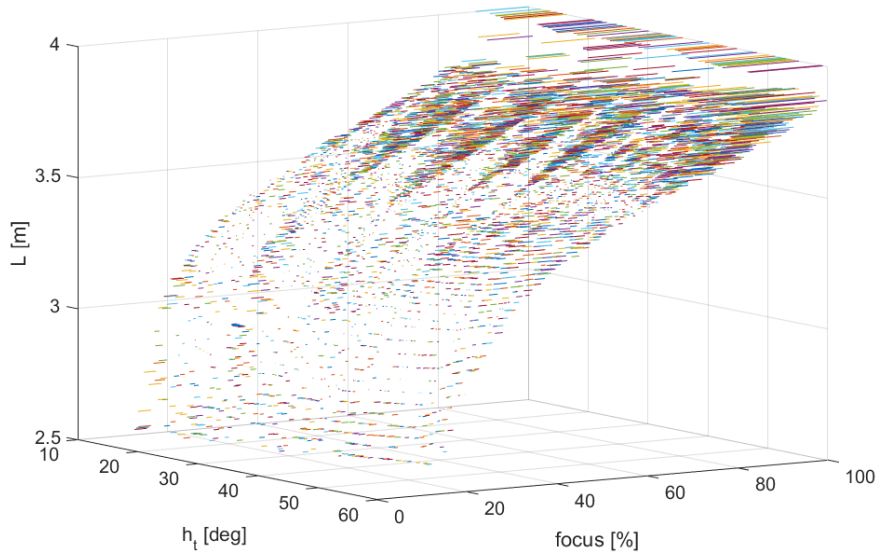

Source: The author.

The results presented in this section indicate that the implementation of defocusing strategies on fresnel collectors is subject to interferences from many sources, which can reduce the effectiveness of the control. A better understanding of the impacts of

Figure 71 – Results for evaluation of effective focus discrepancy for variations of 0.5^o on the mirrors inclination angles, side view.

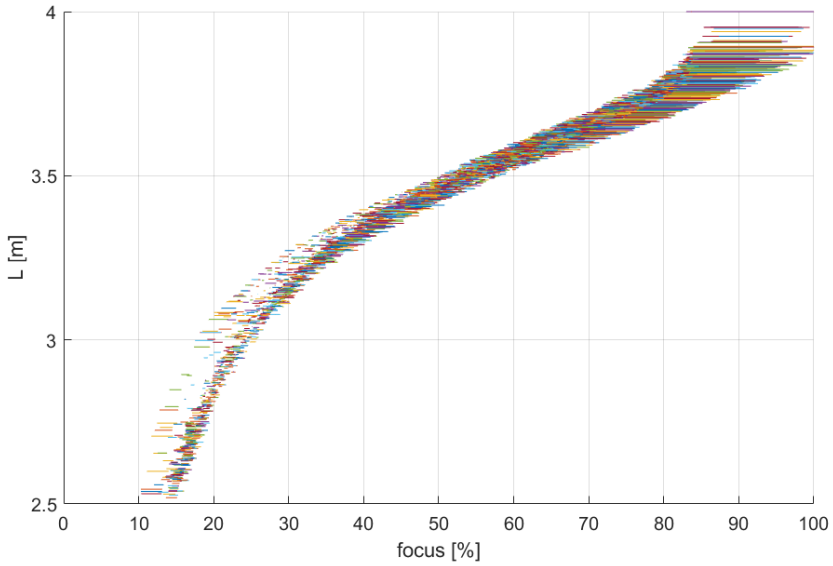

Source: The author.

uncertainties can be crucial for the effectiveness of solar field MPC applications.

5.5 FINAL REMARKS

This chapter presented an evaluation of two Model Predictive Control proposals for solar fields with defocusing fresnel collectors and analyzed the effects of different types of errors on the effectiveness of the proposed defocusing strategy. The dynamic simulations of the closed-loop systems operating with the proposed controllers showed that the NMPC controller was able to more closely track the temperature reference for the solar field albeit presented considerably greater and less coherent execution times and more aggressive control actions when compared to the PNMPC proposal. The error analysis showed that the sampling time has a small impact on the tracking accuracy but also showed that relatively small uncertainty on the inclination of the collector's mirrors can produce great inconsistencies between the desired focus value computed by the controller and the effective focus value affecting the process. The simulations also showed that the proposed defocusing strategy is limited when considering an odd number of mirrors on the collectors. Overall, the proposed control structure was able to operate the process within the operational constraints and with reasonable computation times.

6 CONTRIBUTION: IMPROVING DEFOCUSING WITH NEURO-FUZZY MODELS

One of the main operational issues for Concentrating Solar Power (CSP) plants is the overheating of the Heat Transfer Fluid (HTF), which frequently occurs as the solar collector fields are designed to provide multiples of the thermal energy necessary to operate. If overheating temperatures are reached, the HTF can degrade, generating numerous issues, reducing the system's performance, and compromising its safety. As such, avoiding the operational upper bounds for temperatures constitutes an interesting control problem, as the solar collector should provide the biggest energy output possible while maintaining the integrity of the process components.

Many works utilize the Neuro-Fuzzy techniques to model nonlinear of dynamic systems, control and estimation of solar concentration processes. ANFIS is a hybrid model introduced by (JANG, 1993) widely used. For example, in (ESCAÑO, Juan Manuel et al., 2020) developed a soft sensor to classify the behavior of drivers in real time. The algorithm consists of several NF systems in combination with PCA. Besides, a Neuro-Fuzzy estimator is developed in (ESCAÑO, J. M. et al., 2021) to estimate the non-observable states in a parabolic trough solar field. In addition, (SALAZAR, W. D. C. et al., 2021; SALAZAR, W. C. et al., 2022) a Neuro-Fuzzy model of a Fresnel solar field and high temperature generator (HTG) is developed, focusing on a rule-based model.

The work in this chapter proposes a defocusing strategy for fresnel collectors, considering the collector's optical geometry in order to calculate the mirror inclination angles that produce the required focus value. Two contributions to the proposed strategy are compared: the first uses the model proposed in Chapter 4 in an optimization problem to determine the mirrors' angles, as presented in the previous chapter, and the second consists of a Neuro-Fuzzy structure that is trained with a reference ray-tracing software. Both implementations are compared with simulations from a reference optical modeling software.

This Chapter is divided as follows: Section 6.1 describes the proposed defocusing algorithm. Section 6.2 presents the optimization based defocusing strategy. Section 6.3 presents the ANFIS defocusing stratetgy, as well as the training process and training results. Section 6.4 presents results where simulations comparing the proposed strategies and SolTrace are shown. Section 6.5 presents the final remarks of the chapter. The results of this paper were submitted to IFAC World Congress 2023.

6.1 DEFOCUSING STRATEGY FOR A FRESNEL COLLECTOR

The proposed strategy for defocusing of fresnel collectors consists of changing the focal point of the mirrors, in such a way that the amount of irradiance incident on the absorber is equivalent to the percentage defined by the desired focus value (F^{ref}), with respect to the amount of irradiance that the absorber receives when operating the

solar tracking with complete focus. This procedure was described in Section 5.3.

Although helpful, calculating the mirror inclination angles for a given focus elevation is not sufficient to implement the defocusing strategy, as there is no clear relationship between F^{ref} and the new elevation L. The next sections present two approaches to obtaining the desired focus value.

6.2 OPTIMIZATION-BASED DEFOCUS

The optimization-based approach fot defocusing of fresnel collectors is the one described in section 5.3, using the optical model presented in Chapter 4.

The reference optical models which are commonly used to design from solar collectors to whole CSP fields are based on Ray-Tracing techniques. These models use the Monte Carlo method to simulate solar ray paths and compute their trajectory while reflecting on mirrors and hitting opaque barriers, such as the absorber. Although it is desirable to use the Ray-Tracing models to solve the optimization problem, it is not practical as these models have relatively *high computation times* and the topology of the cost function has several local minima and maxima, therefore it is necessary to use heuristic techniques, such as Particle Swarm Optimization, in order to obtain a solution. These heuristic techniques require large amounts of calls to the objective function and to the Ray-Tracing model, making it impractical for real-time applications. Solving with SolTrace takes approximately 44 seconds per sample, which it may be a high sampling time regarding the overheating issue.

The optical model proposed by (BRANDÃO; COSTA MENDES; NORMEY-RICO, 2022) arises as a second option for this approach, as it has a small computational cost and was validated with SolTrace for solar tracking. With this model coupled with the proposed optimization problem, the first proposal for the implementation of the defocusing strategy is complete. The next section presents the other defocusing implementation proposal, now based on a Neuro-Fuzzy approach.

6.3 NEURO-FUZZY BASED DEFOCUS

This chapter proposes a structure based on an ANFIS to compute the collector focus point that results in a desired defocus value, as represented in Figure 74. In this case, several data points were obtained from SolTrace in order to train the neuro-fuzzy network. The SolTrace software was given a series of values for the solar position (h_t) and elevation (L) and, as described previously, equation 104 is used in order to obtain reference values for the focus ($F^{ref}(h_t, L)$). These values of h_t, L, and F^{ref} are then used to train the neuro-fuzzy structure, as described in the next section. The goal is to make this structure provide the correct values of L that implement the desired focus values F^{ref}, given a specific solar angle h_t.

6.3.1 Preparation of data

Preliminary work has been done on the data set to train the neuro-fuzzy based defocus. The data set is stored in a Matrix $\mathbf{D} \in \Re^{n \times m}$, where n is the total number of samples ($n = 44260$) and m represents the number of variables, which in this case are 3. The variables that compose **D** are shown in Table 7.

Table 7 – Variables composing the data set.

Symbol	description	Range		Unit
		Min	Max	
h_t	Transverse solar angle.	0	90	[^{o}]
F^{ref}	Desired focus	0	100	[%]
L	Focus point	0	4	[m]

First, from **D** the minimum and maximum of each variable are identified. Subsequently, the Matrix **D** is divided into three sets: training, checking, and validation as shown in Figure 72. The learning set is composed of the training and checking sets and has 35408 samples for the learning process and 8852 samples for validation.

Figure 72 – Organization of available data.

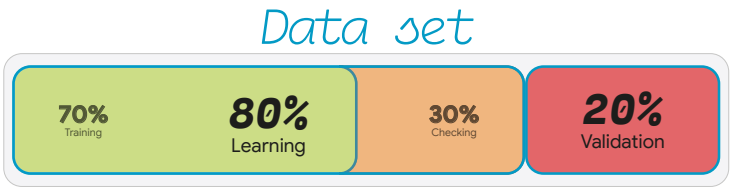

Source: The author.

A normalization process is added to the learning set using Min-Max feature scaling so that all values fall in the range [0, 1]. The values of each variable have a different scale, which can affect the learning process due to inconsistencies. It is solved by the normalization process, thus avoiding the different nature and magnitude of the variables, as noted in William D. Chicaiza Salazar et al. (2021) and William Chicaiza Salazar et al. (2022).

6.3.2 Neuro-Fuzzy model obtained

An ANFIS architecture is used to estimate the focus point (L), using the h_t and F^{ref} variables as inlet and (L) as outlet. Thus, a Fuzzy Inference System (FIS) was obtained to estimate the focus point of the collectors. In order to train the ANFIS network, a dataset covering different working points is needed. The learning process of the ANFIS architecture uses the training and test sets. In this process, the ANFIS looks at the normalized RMSE of the training and check set in order not to overfit only the first set, which would cause the obtained FIS to output inappropriate values for values

that have not been seen in the learning process. In this way, it seeks a middle ground where learning is general in both groups.

Initially, a subtractive clustering (SC) Chiu (1994) method is used to obtain the membership functions, i.e., the number and centers of the antecedent parameters of the fuzzy rules. A hybrid learning method is then applied; backpropagation (BP) to determine the *antecedent parameters* and least squares to estimate the *consequent linear parameters* for each epoch or sweep. The parameters of the ANFIS network obtained in the learning process are presented in Table 8.

Table 8 – ANFIS parameters.

Description	**ANFIS**
MF type:	*Gaussian*
Optimization method:	*hybrid*
Output MF type:	*linear*
FIS	Defocus
Number MFs:	5
Number rules:	5
Influence range	0.6
Epoch number:	2000

Each rule has *antecedents* and *consequent* parameters. The antecedent parameters consist of membership functions of the Gaussian type of each crisp input z_i that forms the fuzzy sets. Whereas a first-order polynomial function contains the consequent parameters. Both parameters were adapted in the learning process. The outlet of each rule is a linear combination of input variables added to a constant term. The final output of the Fuzzy Inference system is the weighted average of each outlet of the rule.

The learning process of the ANFIS network uses a few epoch numbers, and the training and checking sets present small errors (see Figure 73) The learning process of the ANFIS network uses a few epoch numbers, and the training and checking sets present small errors, indicating that the learning was general. The error indexes obtained in the learning process for each model are shown in Table 9.

Table 9 – nRMSE index obtained of the learning process for the ANFIS and its updating time.

RMSE min of **Training** & Checking	**ANFIS** obtained
FIS	Defocus
$nRMSE_{Train}(\times 10^{-3})$	8.1552
$nRMSE_{Check}(\times 10^{-3})$	8.8586
$t_{tw}(h)$	0.34

Figure 73 – Normalized Root Mean Squared Error (nRMSE) vs. epoch.

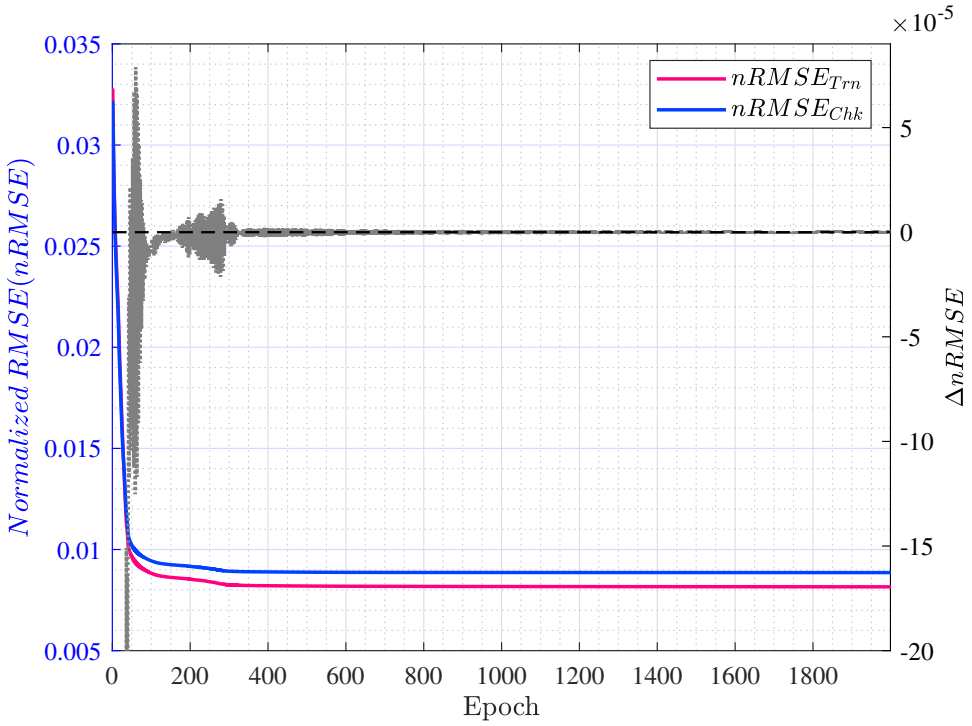

Source: The author.

This chapter develops a neurofuzzy structure that will be referred as **FIS**$_{defocus}$, which is based on ANFIS. The **FIS**$_{defocus}$ should describe the relationship between the focus elevation and a desired focus value for a Fresnel collector, as described in Fig.74. The inputs the variables mentioned in Table 7, with exception of (L) that is chosen as the model output and, therefore, the variable that the neuro-fuzzy network must learn.

Figure 74 – Neuro-Fuzzy based defocus.

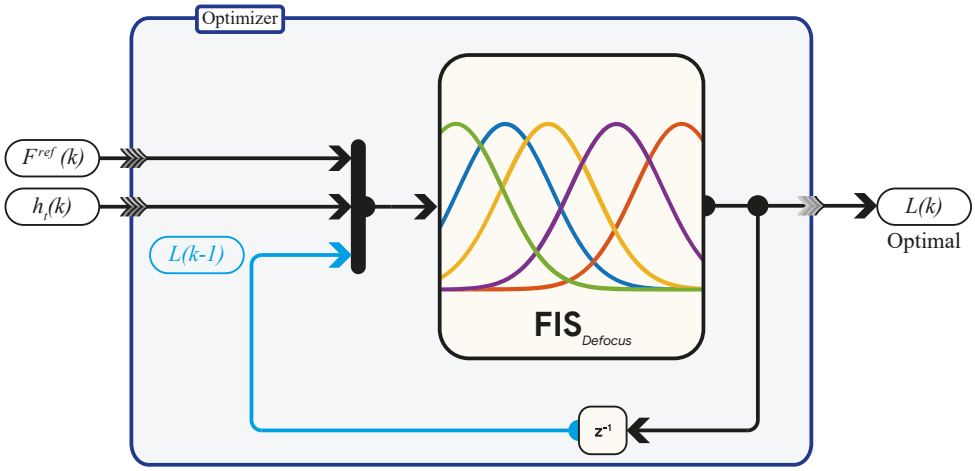

Source: The author.

6.3.3 Validation on Neuro-Fuzzy based defocus

The validation process compares the output $\mathbf{FIS}_{defocus}$ whit the validation data set, that is, a new data set whit 8852 input-output samples. The new data were not used in the learning process of the ANFIS network. Thus, five error indexes were used to compare the FIS output with the actual output data: the arithmetic error mean ($\bar{E}$), standard deviation (*Std*), Root Mean Square Error(*RMSE*), Mean Absolute Percentage Error (*MAPE*) and the coefficient of determination [1] R^2. The error indexes are given by the Equations (107)

$$RMSE = \sqrt{\frac{\sum_{i=1}^{N}(x_{i,j}-\hat{x}_{i,j})^2}{N}} \tag{107a}$$

$$MAPE = \frac{\sum_{i=1}^{N}\frac{|(x_{i,j}-\hat{x}_{i,j})|}{x_{i,j}}}{N} \times 100\% \tag{107b}$$

$$R^2 = 1 - \frac{x_{i,j}-\hat{x}_{i,j}}{x_{i,j}-\bar{x}_{i,j}} \tag{107c}$$

where N represents the number of samples N of validation data set, $x_{i,j}$ is the actual output value and $\hat{x}_{i,j}$ is the output $\mathbf{FIS}_{defocus}$ obtained and $\bar{x}$ is the mean value of the data. The error indexes provide information about precision, i.e, how much the error is dispersed.

Figure 75 shows that $\mathbf{FIS}_{defocus}$ is capable to follow the real value of focus point with an error of $0.45e^{-3} \pm 4.5e^{-4}$ [m] as shown in Table 10.

Table 10 – Validation index of $\mathbf{FIS}_{defocus}$.

Error indexes	**$\mathbf{FIS}_{defocus}$ model**
Mean	$0.45e^{-3}$
Std	$\pm 4.5e^{-4}$
RMSE	$4.5e^{-3}$
MAPE	0.08%
R^2	0.9998

[1] R^2 is a number between 0 and 1, that measures how well a statistical model estimates an outcome. If $R^2 = 0$, the model does not describe the outputs, if $0 < R^2 < 1$, the model partially estimates the outputs, and if $R^2 = 1$ the model perfectly estimates the outputs.

Figure 75 – (a) **FIS**$_{defocus}$ evaluation, FIS output data vs real data. (b) Validation zoom in the first region (orange rectangle). (c) Validation zoom in a second region (cyan rectangle).

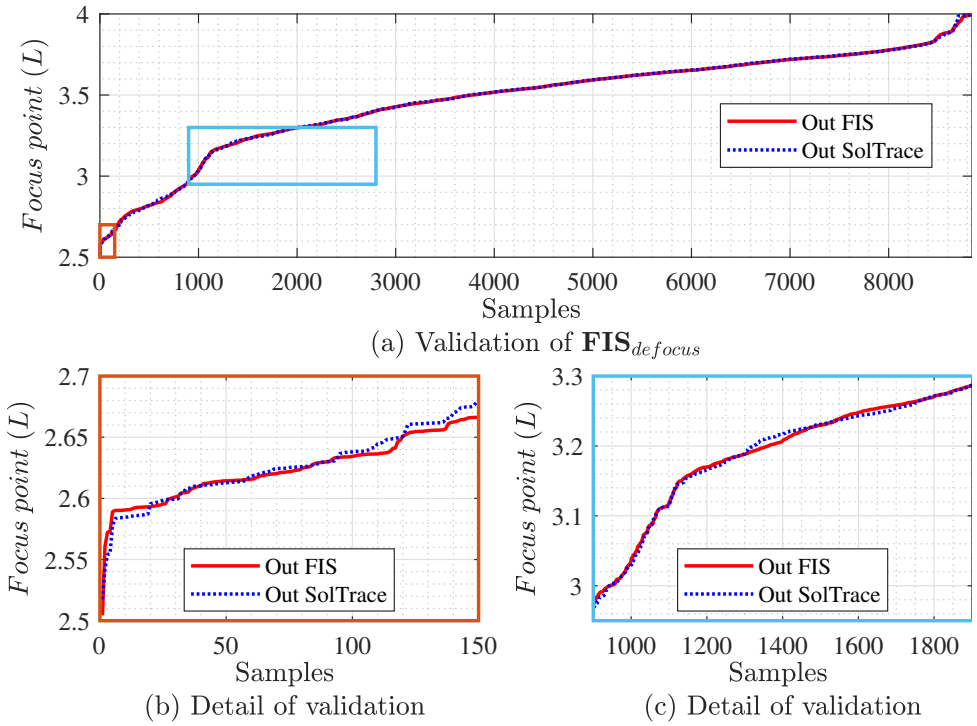

Source: The author.

6.4 SIMULATIONS AND RESULTS OF THE TWO APPROACHES

This section presents the results for comparing the two proposed defocusing structures when applied to the reference SolTrace model. The simulations were performed as follows. Firstly, reference values for focus point elevation (L^{ref}) and solar hour angle (h_t) was applied to the SolTrace reference model, resulting in values of reference focus values (F^{ref}). In order to evaluate the accuracy of the defocusing strategies, the reference focus values from SolTrace are used as inputs in both proposals and the focus point elevation proposed in both cases was compared with the original L^{ref} that contain 44200 samples.

The mapping of the optimization-based proposal is presented in Figure 76, which also presents color-coded information on the irradiance at the absorber. This color code was generated by associating a typical solar irradiation curve with the solar angle data, in order to estimate which points of the mapping represent high irradiation moments of the day.

Regarding the optimisation based strategy, it is noticeable some abnormal behavior for small values of focus, which is due to considering a fresnel collector with an odd number of mirrors. For small focus values, the central mirror will always reflect directly up, toward the absorber. Therefore, it will not be possible to have an effective focus that is smaller than the contribution of this central mirror. In this situation, the pro-

Figure 76 – Mapping of the solution of the defocusing problem for the optimization approach.

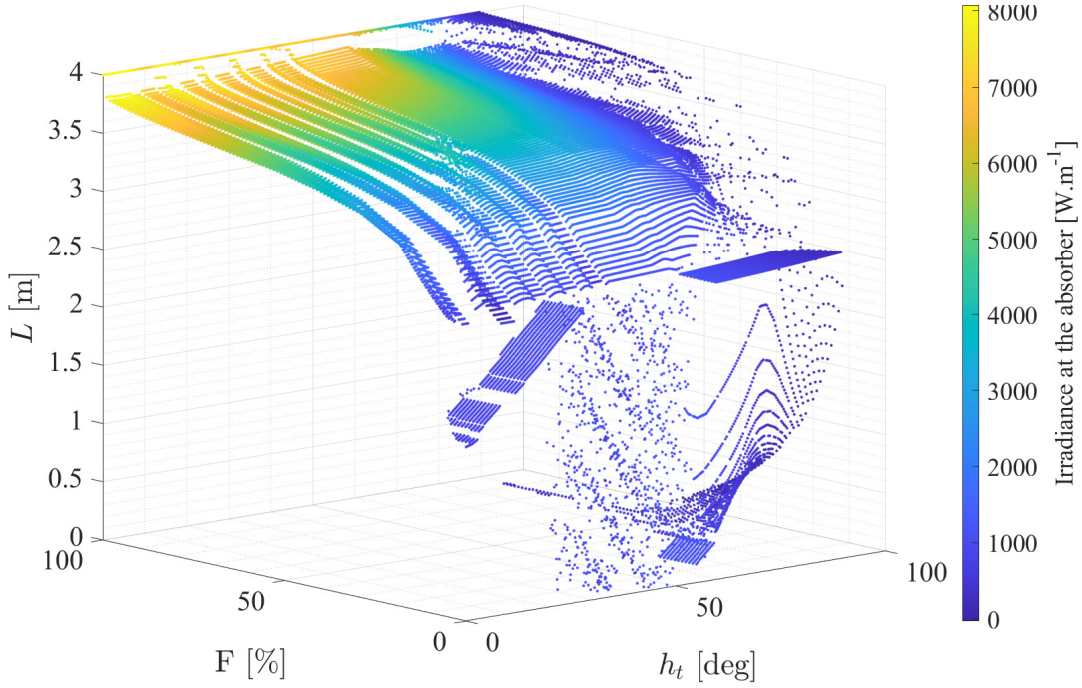

Source: The author.

posed defocsing strategy cannot find and L that implements the desired focus. As this solution is to be implemented in future works, the following analysis will only consider $h_t \in [0^o, 60^o]$ and $F \in [10\%, 100\%]$.

In order to evaluate the accuracy of the calculated elevations obtained from simulation, Figure 77 presents the results for both proposals and the reference values from SolTrace.

It is possible to see the highly nonlinear behavior of the defocusing in fresnel collectors. One can also notice that the ANFIS surface seems closer to the reference surface for all points when compared with the optimization-based approach. This becomes more evident in Figure 78, where the error for both proposals is shown. It is clearly seen that the ANFIS has, approximately, a flat and close to zero error in the whole range.

Some performance indexes were calculated and presented in Table 11, which reinforces the superior performance of the ANFIS proposal, even when comparing the average execution time for each sample. The error is reduced considerably with respect to the optimization based strategy and does not present problems when using an odd number of mirrors.

Another advantage of both methods is the computation time in comparison to the Soltrace software. Soltrace's computation time (44 s) would be quite long to apply defocus control signals given the nature of the problem, overheating. The computation time of both methods is less than 1 second, with the ANFIS-based system being the

Figure 77 – Comparison of the results for the optimization approach, Neuro-Fuzzy approach and the reference values for the focus.

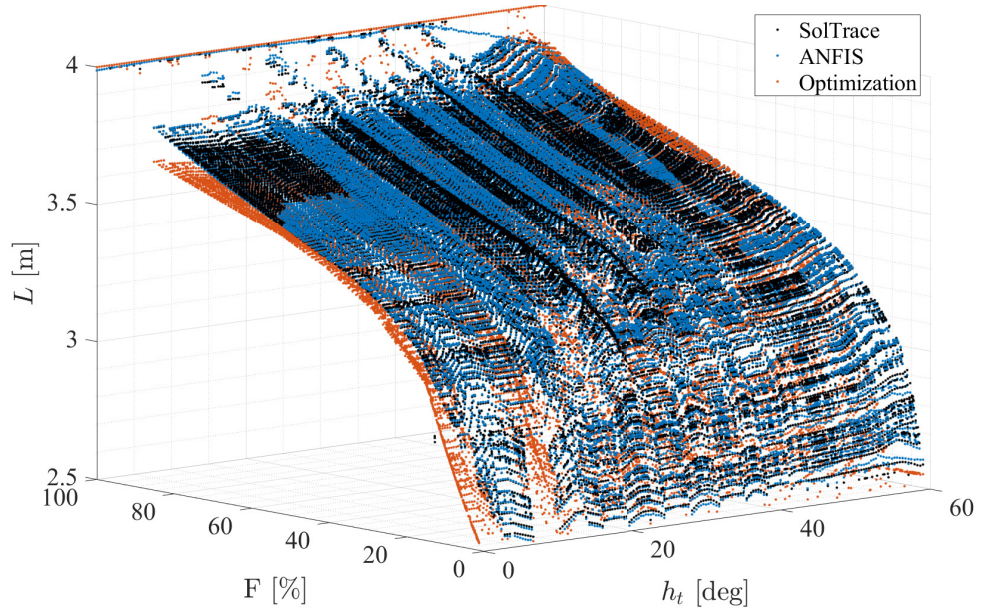

Source: The author.

Figure 78 – Comparison of the error for the optimization approach, Neuro-Fuzzy approach.

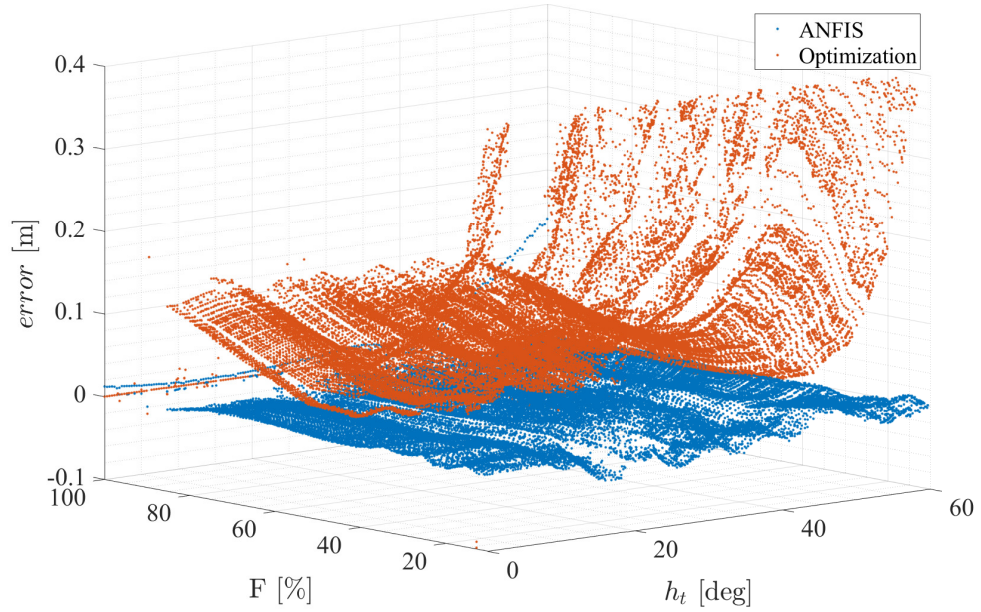

Source: The author.

shortest, less than 1 millisecond. In large scale Fresnel solar plants the computation time is an important factor.

Table 11 – Performance indexes.

Index	$\mathbf{FIS}_{defocus}$	Opt. simple model	Opt. SolTrace
Mean	$4.4650e{-}05$	0.3365	-
RMSE	$6.6544e{-}05$	0.0033	-
MAPE	0.2722%	11.3107%	-
R^2	0.9979	0.8344	-
Avg. comp. time (s)	$0.4e^{-3}$	0.4	44

6.5 CONCLUSION

In this work, an ANFIS network was employed to capture the focus point value of a fresnel collector modeled in Ray-Tracing software. A fuzzy inference system of First-order recursive of 5 rules is obtained once the learning process is completed. In addition, the FIS obtained presents a low error, about the real value of the focus point. It also presented an optimization approach that also implements the proposed defocusing algorithm and showed inferior results when compare to ANFIS. Results showed that the proposed defocus strategy based on the optimisation algorithm have limitations when using an odd number of mirrors in the fresnel collector. On the other hand, the system ANFIS based approach has shown to have a high performance, with a mean error of $4.4650e{-}05$, a MAPE of 0.2722% and low computation time.

Future works can explore the limitations of the defocusing strategy by considering a change of behavior when only the central mirror is illuminating the absorber. Improving the optimization-based approach with a better optical model is also an interesting research path as using a FIS model as the optical model of the problem could unite the advantages of both approaches.

7 CONCLUSION AND FUTURE WORK

This document presented the results obtained from the thesis titled "Modeling and predictive control with defocusing in thermosolar systems". The thesis explored the issue of controlling a solar fresnel collector filed with manipulation of the level of focus at the solar energy collectors. The manipulation of the focus on each collector is studied as it contributed to fast actuation on overheating scenarios of the HTF, which are common in solar thermal power plants. This issue is tipically handled by safety systems, thus is not usually incorporated in the control of the process, which can possibly reduce the energy yeld of the solar field due to conservative defocusing.

Contributions were made in proposing MPC formulations for control of the field, proposing a novel simplified optical model for the fresnel collector, and the proposal of two defocusing strategies and and sensitivity analysis for some factors that could significantly depreciate the performance of the control.

The first contribution was a variation of the controllers proposed by Elias et al. (2018), by incorporating aspects of the On//Off and partial defocusing formulations. The results showed that the proposed controller was able to avoid the overheating of the process with smoother movement of the manipulated variables, with the exception of pump failure scenario, where it presented difficulties on avoiding excessive movement of the HTF flow. These results were presented at the Solar World Congress 2019:

BRANDÃO, Adriano S. M.; COSTA MENDES, Paulo Renato da; ELIAS, Tiago De Araújo, et al. Overheating Prevention in Solar Collectors Using a Hybrid Predictive Controller. In: ISES Solar World Congress 2019 Proceedings. Santiago, Chile: International Solar Energy Society, 2019. p. 861–872.

The second contribution was the development of a novel simplified optical model for a fresnel collector, allowing the study of different solar aiming strategies and later the implementation of defocusing strategies. The model is non-iterative and does not require complex computations. It was validated through IAM with data from the manufacturer of the reference collector and with the SolTrace software. These results were published in the Renewable Energy journal:

BRANDÃO, Adriano S. M.; COSTA MENDES, P.R. da; NORMEY-RICO, Julio E. Simplified optical model, aiming strategy and partial defocusing strategy for solar Fresnel collectors. **Renewable Energy**, v. 188, 2022. ISSN 18790682. DOI: 10.1016/j.renene.2022.02.019.

The third contribution of this thesis was a methodology for evaluating the impacts of using the proposed defocusing strategy through the lens of process control. It was proposed a simple nonlinear MPC controller that provided reference focus values to a lower structure that computes the inclination of each mirror of the collector in order to obtain the desired focus. Then, it was simulated the error in obtaining this desired

focus when introducing errors on the inclination of the mirrors, on the parallelism of the mirrors and it was also analyzed the error introduced by the sampling time applied to the solar aiming strategy. Results showed that errors as small as 0.5^o on the inclination of the mirrors can offset the effective focus in more than 20% of the desired focus value. These results were submitted for publishing on the Solar Energy journal.

BRANDÃO, Adriano S. M.; NORMEY-RICO, Julio E. CSP field predictive control with Fresnel collector defocusing. **Solar Energy**, submitted.

Finally, the last contribution of this thesis was an alternative to the optimization-based approach for computing the inclination of the mirrors for defocusing. It was proposed an ANFIS structure that was trained with data from SolTrace and presented superior performance in both accuracy and computing time. These results were submitted for the 2023 IFAC World Congress.

BRANDÃO, Adriano S. M.; CHICAIZA, William D., et al. Neurofuzzy Defocusing strategy for a Fresnel collector. In: submitted

During the development of this thesis, it was also published an scientific dissemination paper at the Revista PPGEAS. In this paper, the issues of generating thermossolar energy were presented, some of which are the motivation of this thesis.

BRANDÃO, Adriano S. M.; NORMEY-RICO, Julio E. Energia termossolar, coletores Fresnel e os desafios da geração sustentável de eletricidade. **Revista PPGEAS**, v. 4, p. 14–19, 2022.

7.1 FUTURE WORK

Much of the work of this thesis are the initial steps on researching the use of defocusing with fresnel collectors. There are opportunities for improving the optical model, the defocusing strategies and the controllers, such as:

- Improve the optical model by considering the geometry of the absorber, mirror blocking and improving some of the approximations that are made.
- Analyze the impact of the different solar tracking strategies on the distribution of heat over the absorber tube.
- Formulate a tracking strategy that minimizes the irradiance gradient over the absorber tube.
- Propose a robust controller or stochastic controller considering the uncertanties involved in the use of defocusing and the uncertain nature of the weather.
- Use ANFIS to learn the optics of the fresnel collector and use this model to propose other optimization-based defocusing strategies.

- Improve the proposed continuous defocusing stategy in order to allow total defocusing when considering an odd number of mirrors.

REFERENCES

ACHLEITNER, S. et al. SIPS: Solar Irradiance Prediction System. In: IPSN-14 Proceedings of the 13th International Symposium on Information Processing in Sensor Networks. [S.l.: s.n.], 2014. p. 225–236.

ALHAJ, Mohamed; AL-GHAMDI, Sami G. Reducing electric energy consumption in linear Fresnel collector solar fields coupled to thermal desalination plants by optimal mirror defocusing. **Heliyon**, v. 4, n. 9, e00813, 2018. ISSN 2405-8440. DOI: https://doi.org/10.1016/j.heliyon.2018.e00813. Available from: https://www.sciencedirect.com/science/article/pii/S2405844018309691.

ANDERSSON, J. **A General-Purpose Software Framework for Dynamic Optimization**. [S.l.: s.n.], 2013. p. 186. ISBN 9789460187506. DOI: 10.4103/1319-3767.91729. Available from: https://lirias2repo.kuleuven.be/bitstream/id/243411/.

ANDRADE, G.A. et al. A practical NMPC with robustness of stability applied to distributed solar power plants. **Solar Energy**, v. 92, p. 106–122, 2013. ISSN 0038-092X. DOI: https://doi.org/10.1016/j.solener.2013.02.013. Available from: https://www.sciencedirect.com/science/article/pii/S0038092X13000789.

ARAÚJO ELIAS, Tiago de; COSTA MENDES, Paulo Renato da; NORMEY-RICO, Júlio Elias. Hybrid predictive controller for overheating prevention of solar collectors. **Renewable Energy**, Elsevier Ltd, v. 136, p. 535–547, 2019. ISSN 18790682. DOI: 10.1016/j.renene.2019.01.001. Available from: https://doi.org/10.1016/j.renene.2019.01.001.

AUROUSSEAU, Antoine et al. Control systems for direct steam generation in linear concentrating solar power plants, 2016. DOI: 10.1016/j.rser.2015.11.083Ãŕ. Available from: https://hal.archives-ouvertes.fr/hal-01609110/document.

AXEHILL, Daniel; HANSSON, Anders. A preprocessing algorithm for MIQP solvers with applications to MPC. In: 2497–2502 vol.3. DOI: 10.1109/CDC.2004.1428790.

BAKHTIARI, Amin; BIDI, Mokhtar. INVESTIGATION OF TRACKING SYSTEMS CONTRIBUTION TO PARABOLIC. August, 2015.

BARBÓN, A. et al. Influence of solar tracking error on the performance of a small-scale linear Fresnel reflector. **Renewable Energy**, v. 162, p. 43–54, 2020. ISSN 0960-1481. DOI: https://doi.org/10.1016/j.renene.2020.07.132. Available from: http://www.sciencedirect.com/science/article/pii/S0960148120312088.

BEMPORAD, Alberto; MORARI, Manfred. Control of systems integrating logic, dynamics, and constraints. **Automatica**, v. 35, n. 3, p. 407–427, 1999. ISSN 00051098. DOI: 10.1016/S0005-1098(98)00178-2.

BEMPORAD, Alberto; NAIK, Vihangkumar V. A Numerically Robust Mixed-Integer Quadratic Programming Solver for Embedded Hybrid Model Predictive Control. **IFAC-PapersOnLine**, v. 51, n. 20, p. 412–417, 2018. 6th IFAC Conference on Nonlinear Model Predictive Control NMPC 2018. ISSN 2405-8963. DOI: https://doi.org/10.1016/j.ifacol.2018.11.068. Available from: https://www.sciencedirect.com/science/article/pii/S2405896318327265.

BENYAKHLEF, S et al. Development of Ray Tracing Code for Modeling Linear Fresnel Collector Systems. **International Conference on Mechanics and Energy**, 2014.

BIEGLER, Lorenz Theodor. A perspective on nonlinear model predictive control. **Korean J. Chem. Eng**, v. 38, p. 1317–1332, 7 2021. ISSN 1975-7220. DOI: 10.1007/s11814-021-0791-7.

BOCK, H. G.; PLITT, K. J. Multiple Shooting Algorithm for Direct Solution of Optimal Control Problems. **IFAC Proceedings Series**, Elsevier, v. 17, n. 2, p. 1603–1608, 1984. ISSN 07411146. DOI: 10.1016/S1474-6670(17)61205-9. Available from: http://dx.doi.org/10.1016/S1474-6670(17)61205-9.

BRAGA, M.; DO NASCIMENTO, L. R.; RÜTHER, R. Spectral Impacts on the Performance of mc-Si and New-Generation CdTe Photovoltaics in the Brazilian Northeast. In: 2019 IEEE 46th Photovoltaic Specialists Conference (PVSC). [S.l.: s.n.], 2019. p. 1226–1231.

BRANDÃO, Adriano S. M.; CHICAIZA, William D., et al. Neurofuzzy Defocusing strategy for a Fresnel collector. In: submitted.

BRANDÃO, Adriano S. M.; COSTA MENDES, P.R. da; NORMEY-RICO, Julio E. Simplified optical model, aiming strategy and partial defocusing strategy for solar Fresnel collectors. **Renewable Energy**, v. 188, 2022. ISSN 18790682. DOI: 10.1016/j.renene.2022.02.019.

BRANDÃO, Adriano S. M.; NORMEY-RICO, Julio E. CSP field predictive control with Fresnel collector defocusing. **Solar Energy**, submitted.

BRANDÃO, Adriano S. M.; NORMEY-RICO, Julio E. Energia termossolar, coletores Fresnel e os desafios da geração sustentável de eletricidade. **Revista PPGEAS**, v. 4, p. 14–19, 2022.

BUIE, D.; MONGER, A.G.; DEY, C.J. Sunshape distributions for terrestrial solar simulations. **Solar Energy**, v. 74, n. 2, p. 113–122, 2003. ISSN 0038-092X. DOI: https://doi.org/10.1016/S0038-092X(03)00125-7. Available from: https://www.sciencedirect.com/science/article/pii/S0038092X03001257.

CAGNOLI, M. et al. Analysis of the performance of linear Fresnel collectors: Encapsulated vs. evacuated tubes. **Solar Energy**, v. 164, p. 119–138, 2018. ISSN

0038-092X. DOI: https://doi.org/10.1016/j.solener.2018.02.037. Available from: https://www.sciencedirect.com/science/article/pii/S0038092X18301695.

CAMACHO, E. F.; RAMIREZ, D. R., et al. Model predictive control techniques for hybrid systems. In: 1. ANNUAL Reviews in Control. [S.l.]: Elsevier Ltd, 2010. p. 21–31. DOI: 10.1016/j.arcontrol.2010.02.002.

CAMACHO, Eduardo F.; BERENGUEL, Manuel; GALLEGO, Antonio J. Control of thermal solar energy plants. **Journal of Process Control**, Elsevier Ltd, v. 24, p. 332–340, 2 2014. ISSN 09591524. DOI: 10.1016/j.jprocont.2013.09.026.

CAMACHO, Eduardo F.; BERENGUEL, Manuel; RUBIO, Francisco R., et al. **Control of Solar Energy Systems**. London, Uk: Springer, 2012. p. 400. ISBN 9780857299154.

CAMACHO, Eduardo F.; BORDONS, Carlos. **Model predictive control**. 2. ed. [S.l.]: Springer, 2002. v. 1, p. 280. ISBN 3540762418.

CAMACHO, Eduardo F.; GALLEGO, Antonio J. Model Predictive Control in Solar Trough Plants: A Review. **IFAC-PapersOnLine**, Elsevier B.V., v. 48, n. 23, p. 278–285, 2015. ISSN 24058963. DOI: 10.1016/j.ifacol.2015.11.296. Available from: http://dx.doi.org/10.1016/j.ifacol.2015.11.296.

CAMACHO, Eduardo F.; GALLEGO, Antonio J.; ESCAÑO, Juan M., et al. Hybrid Nonlinear MPC of a Solar Cooling Plant. **Energies**, MDPI AG, v. 12, n. 14, p. 2723, July 2019. ISSN 1996-1073. DOI: 10.3390/en12142723. Available from: http://dx.doi.org/10.3390/en12142723.

CAMACHO, Eduardo F.; GALLEGO, Antonio J.; ESCAÑO, Juan M., et al. Hybrid nonlinear MPC of a solar cooling plant. **Energies**, v. 12, n. 14, 2019. ISSN 19961073. DOI: 10.3390/en12142723.

CAMACHO, Eduardo F.; SAMAD, Tariq, et al. Control for Renewable Energy and Smart Grids, 2011.

CAMPOS, Mario Cesar M. Massa de; GOMES, Marcos Vinicius de Carvalho; PEREZ, José Manuel Gonzalez Tubio. **Controle Avançado e Otimização na Indústria do Petróleo**. 1. ed. [S.l.]: Interciência, 2013. p. 510. ISBN 978-8571933095.

CARMONA, Ricardo contreras. **Análisis, modelado y control de un campo de colectores solares distribuidos con sistema de seguimiento en un eje**. Aug. 1985. Universidad de Sevilla.

CERVANTES, M. et al. Utilization of Low Cost, Sky-Imaging Technology for Irradiance Forecasting of Distributed Solar Generation. In: 2016 IEEE Green Technologies Conference (GreenTech). [S.l.: s.n.], 2016. p. 142–146.

CHIU, Stephen. Fuzzy Model Identification Based on Cluster Estimation. **Journal of the Intelligent and Fuzzy Systems**, v. 2, p. 267–278, Jan. 1994. DOI: 10.3233/IFS-1994-2306.

DARBALI-ZAMORA, R. et al. Solar irradiance prediction model based on a statistical approach for microgrid applications. In: 2015 IEEE 42nd Photovoltaic Specialist Conference (PVSC). [S.l.: s.n.], 2015. p. 1–6.

EDDHIBI, F. et al. Analytic optical design of a Linear Fresnel solar collector with variable parameters. **Journal of Materials and Environmental Sciences**, v. 8, n. 10, p. 4068–4084, 2017.

, Irec, [s.l.]. **Optimal solar collectors defocusing based on maximum temperature**. [S.l.: s.n.], 2018. ISBN 9781538609989.

ELSAYED, A. M. et al. Study of the Effect of Using Different Solar Tracking Time-Steps on the Central Tower Receiver Power Plant. In: 2018 IEEE Green Technologies Conference (GreenTech). [S.l.: s.n.], 2018. p. 27–32.

ESCAÑO, J. M. et al. Estimador Neuro-Borroso, con reducción de complejidad, de las temperaturas de un campo solar cilindro-parabólico. **Revista Iberoamericana de Automática e Informática industrial**, v. 18, n. 2, p. 134–145, 2021. ISSN 1697-7920. DOI: 10.4995/riai.2020.13261.

ESCAÑO, Juan Manuel et al. Driver Behavior Soft-Sensor Based on Neurofuzzy Systems and Weighted Projection on Principal Components. **IEEE Sensors Journal**, v. 20, n. 19, p. 11454–11462, 2020. DOI: 10.1109/JSEN.2020.2995921.

FONTES, Raony M.; SANTANA, Daniel D.; MARTINS, Márcio A.F. An MPC auto-tuning framework for tracking economic goals of an ESP-lifted oil well. **Journal of Petroleum Science and Engineering**, v. 217, p. 110867, 2022. ISSN 0920-4105. DOI: https://doi.org/10.1016/j.petrol.2022.110867. Available from: https://www.sciencedirect.com/science/article/pii/S0920410522007227.

HANBING et al. H-TMD with hybrid method for vibration control of long span cable-stayed bridge. **Earthquakes and Structures**, v. 16, n. 3, p. 349–358, Mar. 2019.

HOSSAIN, Monowar et al. Application of the hybrid ANFIS models for long term wind power density prediction with extrapolation capability. **PLOS ONE**, v. 13, e0193772, Apr. 2018. DOI: 10.1371/journal.pone.0193772.

HUANG, Farong; LI, Longlong; HUANG, Weidong. Optical performance of an azimuth tracking linear Fresnel solar concentrator. **Solar Energy**, v. 108, p. 1–12, 2014. ISSN 0038-092X. DOI: https://doi.org/10.1016/j.solener.2014.06.028. Available from: http://www.sciencedirect.com/science/article/pii/S0038092X14003272.

HUSSEIN, Ali S.; ELIAS, Catherine M.; MORGAN, Elsayed I. A realistic model predictive control using single and multiple shooting in the formulation of non-linear programming model. **2019 IEEE International Conference on Vehicular Electronics and Safety, ICVES 2019**, IEEE, 2019. DOI: 10.1109/ICVES.2019.8906364.

INTERGOVERNAMENTAL PANEL ON CLIMATE CHANGE. **Climate Change 2021: The Physical Science Basis**. [S.l.: s.n.], 2021. DOI: 10.1017/9781009157896.

INTERNATIONAL ENERGY AGENCY. **Global Energy & CO2 Status Report**. [S.l.], 2019. DOI: 10.4324/9781315252056.

INTERNATIONAL ENERGY AGENCY. **KEY WORLD ENERGY STATISTICS**. [S.l.], 2019. ISBN 9780444641304. DOI: 10.1016/B978-0-12-409548-9.00927-1.

JAMILU, Muhammad. A Review on Solar Tracking Systems and Their Classifications. v. 2, n. 4, p. 46–50, 2017. DOI: 10.11648/j.jeece.20170204.13.

JANG, J.-S.R. ANFIS: adaptive-network-based fuzzy inference system. **IEEE Transactions on Systems, Man, and Cybernetics**, v. 23, n. 3, p. 665–685, 1993. DOI: 10.1109/21.256541.

JANG, J.-S.R.; SUN, Chuen-Tsai. Neuro-fuzzy modeling and control. **Proceedings of the IEEE**, v. 83, n. 3, p. 378–406, 1995. DOI: 10.1109/5.364486.

JANG, J.S.R.; SUN, C.T.; MIZUTANI, E. **Neuro-fuzzy and Soft Computing: A Computational Approach to Learning and Machine Intelligence**. [S.l.]: Prentice Hall, 1997. (MATLAB curriculum series). ISBN 9780132610667.

JOHANSEN, Tor Arne. Introduction to nonlinear model predictive control and moving horizon estimation. In: TOPICS on Constrained and Nonlinear Control. [S.l.: s.n.], 2011. p. 1–53. ISBN 978-80-968627-4-0. Available from: https://iam.chtf.stuba.sk/%7B~%7Dfikar/nil11/nil-tbook-p.pdf%7B%5C#%7Dpage=201.

KIRCHES, Christian. **Fast Numerical Methods for Mixed-Integer Nonlinear Model-Predictive Control**. Fachmedien Wiesbaden: Springer, 2012. v. 53, p. 1689–1699. ISBN 9788578110796. DOI: 10.1017/CBO9781107415324.004. arXiv: arXiv:1011.1669v3.

LIU, Enliang; LIU, Ding; JIANG, Lei. A Mode Selected Mixed Logic Dynamic Model and Model Predictive Control of Buck Converter. **Complexity**, v. 2020, p. 1–11, Jan. 2020. DOI: 10.1155/2020/5415636.

LOVEGROVE, Keith; STEIN, Wes (Eds.). **Concentrating solar power technology**. Philadelphia: Woodhead Publishing, 2012. ISBN 978-0-85709-617-3.

MACEDO, Isaías Carvalho De. Estado da arte e tendências tecnológicas para energia, p. 90, 2003.

MACHADO, Diogo O. et al. Fresnel Solar Collector Control With Active Defocus. In: 2022 European Control Conference (ECC). [S.l.]: IEEE, July 2022. p. 1804–1809. DOI: 10.23919/ECC55457.2022.9838182. Available from: https://ieeexplore.ieee.org/document/9838182/.

MNKENI, A. P.; SOUNDY, P.; BRUTSCH, M. O. **Solar drying of fruit and vegetables**. [S.l.: s.n.], 2001. Available from: http://www.nda.agric.za/docs/solar/solardrying.htm. Visited on: 12 May 2020.

NEUMANN, Andreas et al. Representative terrestrial solar brightness profiles. **Journal of Solar Energy Engineering, Transactions of the ASME**, v. 124, n. 2, p. 198–204, 2002. ISSN 01996231. DOI: 10.1115/1.1464880.

OLIVEIRA JUNIOR, Hime Aguiar e et al. **Inteligência Computacional Aplicada À Administração, Economia E Engenharia Em Matlab**. [S.l.]: Cengage, 2007.

ORDÓÑEZ, Freddy; FLORES, Esteban; SORIA, Rafael. Fast coupled optical and thermal model for a trapezoidal Fresnel solar collector. **AIP Conference Proceedings**, v. 2303, p. 090001, Dec. 2020. DOI: 10.1063/5.0028485.

OSÓRIO, Tiago et al. Ray-tracing software comparison for linear focusing solar collectors. **AIP Conference Proceedings**, v. 1734, May 2016, 2016. ISSN 15517616. DOI: 10.1063/1.4949041.

PADILLA, Ricardo Vasquez et al. Heat transfer analysis of parabolic trough solar receiver. **Applied Energy**, Elsevier Ltd, v. 88, n. 12, p. 5097–5110, 2011. ISSN 03062619. DOI: 10.1016/j.apenergy.2011.07.012. Available from: http://dx.doi.org/10.1016/j.apenergy.2011.07.012.

BRANDÃO, Adriano S. M.; COSTA MENDES, Paulo Renato da;
ELIAS, Tiago De Araújo, et al. Overheating Prevention in Solar Collectors Using a Hybrid Predictive Controller. In: ISES Solar World Congress 2019 Proceedings. Santiago, Chile: International Solar Energy Society, 2019. p. 861–872.

PEREIRA, Enio Bueno et al. **Atlas Brasileiro da Energia Solar**. 2. ed. [S.l.: s.n.], 2017. p. 80. ISBN 9788517000300. DOI: 978-85-17-00030-0. Available from: http://ftp.cptec.inpe.br/labren/publ/livros/brazil%7B%5C_%7Dsolar%7B%5C_%7Datlas%7B%5C_%7DR1.pdf%7B%5C%%7D5Cnhttp://sonda.ccst.inpe.br/publicacoes/atlas%7B%5C_%7Dsolar.html.

PINO, F. J. et al. Experimental validation of an optical and thermal model of a linear Fresnel collector system. **Applied Thermal Engineering**, Elsevier Ltd, v. 50, n. 2,

p. 1463–1471, 2013. DOI: 10.1016/j.applthermaleng.2011.12.020. Available from: http://dx.doi.org/10.1016/j.applthermaleng.2011.12.020.

PINO, F.J. et al. Experimental validation of an optical and thermal model of a linear Fresnel collector system. **Applied Thermal Engineering**, v. 50, n. 2, 1463–1471, 2013. ISSN 1359-4311. DOI: {https://doi.org/10.1016/j.applthermaleng.2011.12.020}. Available from: %7Bhttp://www.sciencedirect.com/science/article/pii/S1359431111007174%7D.

PINTALDI, Sergio et al. Model predictive control of a high efficiency solar thermal cooling system with thermal storage. **Energy and Buildings**, Elsevier B.V., v. 196, p. 214–226, 2019. ISSN 03787788. DOI: 10.1016/j.enbuild.2019.05.008.

PLUCENIO, A. et al. A PRACTICAL APPROACH TO PREDICTIVE CONTROL FOR NONLINEAR PROCESSES. **IFAC Proceedings Volumes**, v. 40, n. 12, p. 210–215, 2007. 7th IFAC Symposium on Nonlinear Control Systems. ISSN 1474-6670. DOI: https://doi.org/10.3182/20070822-3-ZA-2920.00035. Available from: https://www.sciencedirect.com/science/article/pii/S1474667016355288.

PRADA, C. de et al. Hybrid control of a mixed continuous-batch process. **Computer Aided Chemical Engineering**, v. 18, n. 100, p. 739–744, 2004. ISSN 15707946. DOI: 10.1016/S1570-7946(04)80189-5.

RAWLINGS, James B.; ANGELI, David; BATES, Cuyler N. Fundamentals of economic model predictive control. In: 2012 IEEE 51st IEEE Conference on Decision and Control (CDC). [S.l.: s.n.], 2012. p. 3851–3861. DOI: 10.1109/CDC.2012.6425822.

RETORTA, Fábio Sester et al. Estudo De Alternativas Tecnológicas Visando Nacionalização E Metodologia Para Alocação De Plantas Termossolares Concentradas No Brasil. **VII Congresso Brasileiro de Energia Solar**, p. 10, 2018. DOI: 978-85-62179-02-0.

ROBLEDO, María et al. Development and experimental validation of a dynamic model for a Fresnel solar collector. **IFAC Proceedings Volumes (IFAC-PapersOnline)**, v. 44, 1 PART 1, p. 483–488, 2011. ISSN 14746670. DOI: 10.3182/20110828-6-IT-1002.03252.

SÁ, Alexandre De et al. **Optical and Thermal Investigations of an Experimental Linear Fresnel Concentrator Workbench for Direct Steam Generation**. 2018. PhD thesis – Universidade Federal de Santa Catarina.

SALAZAR, William Chicaiza et al. Neuro-Fuzzy Digital Twin of a High Temperature Generator. **IFAC-PapersOnLine**, v. 55, n. 9, p. 466–471, 2022. 11th IFAC Symposium on Control of Power and Energy Systems CPES 2022. ISSN 2405-8963. DOI: https://doi.org/10.1016/j.ifacol.2022.07.081.

SALAZAR, William D. Chicaiza et al. Neuro-fuzzy Modelling of a Linear Fresnel-type Solar Collector System as a Digital Twin. In: JOINT Proceedings of the 19th World Congress of the International Fuzzy Systems Association (IFSA), the 12th Conference of the European Society for Fuzzy Logic and Technology (EUSFLAT), and the 11th International Summer School on Aggregation Operators (AGOP). [S.l.]: Atlantis Press, 2021. p. 242–249. DOI: https://doi.org/10.2991/asum.k.210827.033.

SALAZAR, William David Chicaiza. **Modelado neuro-borroso de un sistema captador solar lineal tipo Fresnel como gemelo digital**. 2020. MA thesis – Universidad de Sevilla.

SÁNCHEZ, A.J. et al. Event-based MPC for defocusing and power production of a parabolic trough plant under power limitation. **Solar Energy**, v. 174, p. 570–581, 2018. DOI: https://doi.org/10.1016/j.solener.2018.09.044. Available from: http://www.sciencedirect.com/science/article/pii/S0038092X18309289.

SANDIA NATIONAL LABORATORIES. **Sandia's Ephemeris Model**. [S.l.: s.n.], 2018. Available from: https://pvpmc.sandia.gov/modeling-steps/1-weather-design-inputs/sun-position/sandias-code/.

SILVI, Cesare. Italian contribution to CSP with flat or almost flat reflectors. **30th ISES Biennial Solar World Congress 2011, SWC 2011**, v. 2, November, p. 952–962, 2011. DOI: 10.18086/swc.2011.06.12.

SOLAR, Industrial. **Fresnel Collector LF-11 datasheet**. [S.l.], 2007. Available from: https://www.google.com/search?q=Industrial+solar+LF-11&source=lmns&bih=625&biw=1366&hl=pt-BR&ved=2ahUKEwibir29u8DoAhUzCbkGHetXBnwQ_AUoAHoECAEQAA.

SOLAR PAYBACK. Energia Termossolar Para a Indústria - Brasil, p. 68, 2018. ISSN 1043-4542. Available from: https://www.solarwirtschaft.de/fileadmin/user%7B%5C_%7Dupload/national%7B%5C_%7Dprocess%7B%5C_%7Dheat%7B%5C_%7Dmex%7B%5C_%7Dspb.pdf.

SPOLADORE, Marco; CAMACHO, Eduardo F.; VALCHER, M. Elena. Distributed Parameters Dynamic Model of a Solar Fresnel Collector Field. **IFAC Proceedings Volumes**, v. 44, n. 1, p. 14784–14789, 2011. 18th IFAC World Congress. ISSN 1474-6670. DOI: https://doi.org/10.3182/20110828-6-IT-1002.02992. Available from: https://www.sciencedirect.com/science/article/pii/S1474667016460040.

SUHAIL, Mohammad et al. Development of Progressive Fuzzy Logic and ANFIS Control for Energy Management of Plug-In Hybrid Electric Vehicle. **IEEE Access**, v. 9, p. 62219–62231, 2021. DOI: 10.1109/ACCESS.2021.3073862.

SUN, Xiaoqiang et al. Optimal control of intelligent vehicle longitudinal dynamics via hybrid model predictive control. **Robotics and Autonomous Systems**, v. 112,

p. 190–200, 2019. ISSN 0921-8890. DOI: https://doi.org/10.1016/j.robot.2018.11.020. Available from: http://www.sciencedirect.com/science/article/pii/S0921889018306122.

TAKAGI, T.; SUGENO, M. Fuzzy identification of systems and its applications to modeling and control. **IEEE Transactions on Systems, Man, and Cybernetics**, SMC-15, n. 1, p. 116–132, 1985. DOI: 10.1109/TSMC.1985.6313399.

PIGOZZO, Victor Cesar. **DESENVOLVIMENTO E ANALISE EXPERIMENTAL DE UM CONCENTRADOR SOLAR FRESNEL LINEAR PARA GERACAO DIRETA DE VAPOR**. 2019. PhD thesis – Universidade Federal de Santa Catarina. Available from: http://tede.ufsc.br/teses/PEMC1997-T.pdf.

TIAN, Y.; ZHAO, C.Y. A review of solar collectors and thermal energy storage in solar thermal applications. **Applied Energy**, v. 104, p. 538–553, 2013. ISSN 0306-2619. DOI: https://doi.org/10.1016/j.apenergy.2012.11.051. Available from: https://www.sciencedirect.com/science/article/pii/S0306261912008549.

TIAN, Zhiyong; PERERS, Bengt, et al. Analysis and validation of a quasi-dynamic model for a solar collector field with flat plate collectors and parabolic trough collectors in series for district heating. English. **Energy**, Elsevier, v. 142, p. 130–138, 2018. ISSN 0360-5442. DOI: 10.1016/j.energy.2017.09.135.

TORRICO, B. C. et al. Robust Nonlinear Predictive Control Applied to a Solar Collector Field in a Solar Desalination Plant. **IEEE Transactions on Control Systems Technology**, v. 18, n. 6, p. 1430–1439, 2010.

TSEKOURAS, P.; TZIVANIDIS, C.; ANTONOPOULOS, K. Optical and thermal investigation of a linear Fresnel collector with trapezoidal cavity receiver. **Applied Thermal Engineering**, v. 135, p. 379–388, 2018. ISSN 1359-4311. DOI: https://doi.org/10.1016/j.applthermaleng.2018.02.082. Available from: http://www.sciencedirect.com/science/article/pii/S1359431117363354.

U.S. DEPARTMENT OF ENERGY. **Concentrating solar power commercial application study: Reducing water consumption of concentrating solar power electricity generation**. v. 2001. [S.l.], 2011. p. 175–205. ISBN 9781607419860.

UNITED NATIONS. Paris Agreement. **United Nations Treaty Collection, Chapter XXVII 7. d**, 2015. Available from: https://treaties.un.org/pages/ViewDetails.aspx?src=TREATY&mtdsg_no=XXVII-7-d&chapter=27&clang=_en.

VASALLO, Manuel Jesús; BRAVO, José Manuel. A MPC approach for optimal generation scheduling in CSP plants. **Applied Energy**, v. 165, p. 357–370, 2016. ISSN 03062619. DOI: 10.1016/j.apenergy.2015.12.092.

VERGARA, José Dolores et al. Controle de temperatura em campos solares de grande porte utilizando a abordagem do {PNMPC} - Practical Nonlinear Model Predictive Control. **{XXI} Congresso Brasileiro de Automática**, April, p. 1885–1890, 2016.

VILJOEN, J. H.; MULLER, C. J.; CRAIG, I. K. Hybrid nonlinear model predictive control of a cooling water network. **Control Engineering Practice**, Elsevier Ltd, v. 97, February, p. 104319, 2020. ISSN 09670661. DOI: 10.1016/j.conengprac.2020.104319. Available from: https://doi.org/10.1016/j.conengprac.2020.104319.

WAGNER, Michael J. Results and Comparison from the SAM Linear Fresnel Technology Performance Model. **Pix**, v. 16560, April, p. 10, 2012. Available from: http://www.osti.gov/bridge:.

WANG, Gang et al. Experimental and optical performances of a solar CPV device using a linear Fresnel reflector concentrator. **Renewable Energy**, v. 146, p. 2351–2361, 2020. ISSN 0960-1481. DOI: https://doi.org/10.1016/j.renene.2019.08.090. Available from: http://www.sciencedirect.com/science/article/pii/S0960148119312777.

WEISS, Werner; SPÖRK-DÜR, Monika; MAUTHNER, Franz. Solar Heat Worldwide, edition 2017. **SHC (Solar Heating and Cooling) IEA (International Energy Agency)**, 2017. Available from: http://www.solarthermalworld.org.

WENDELIN, Tim. SolTRACE: A New Optical Modeling Tool for Concentrating Solar Optics. In: INTERNATIONAL Solar Energy Conference. [S.l.: s.n.], Jan. 2003. DOI: 10.1115/ISEC2003-44090.

WILBERT, Stefan. **Determination of Circumsolar Radiation and its Effect on Concentrating Solar Power**. 2014. s. 177. PhD thesis – RWTH Aachen. Available from: http://darwin.bth.rwth-aachen.de/opus3/volltexte/2014/5171/.

YANG, Bryant Bruce Picon. **CONTRIBUIC¸ OES AOS ALGORITMOS PNMPC E DMC COM PASSO DE ESTABILIDADE**. 2016. MA thesis – Universidade Federal de Santa Catarina.

YANG, Chen et al. MLD-MPC for Ultra-Supercritical Circulating Fluidized Bed Boiler Unit Using Subspace Identification. **Energies**, v. 15, n. 15, 2022. ISSN 1996-1073. DOI: 10.3390/en15155476. Available from: https://www.mdpi.com/1996-1073/15/15/5476.

ZADEH, L.A. Fuzzy sets. **Information and Control**, v. 8, n. 3, p. 338–353, 1965. ISSN 0019-9958. DOI: https://doi.org/10.1016/S0019-9958(65)90241-X. Available from: https://www.sciencedirect.com/science/article/pii/S001999586590241X.

ZHANG, H. L. et al. Concentrated solar power plants: Review and design methodology. **Renewable and Sustainable Energy Reviews**, v. 22, p. 466–481, 2013. DOI: 10.1016/j.rser.2013.01.032.

ZHU, Guangdong. Development of an analytical optical method for linear fresnel collectors. **Solar Energy**, v. 94, 2013. ISSN 0038-092X. DOI: https://doi.org/10.1016/j.solener.2013.05.003. Available from: http://www.sciencedirect.com/science/article/pii/S0038092X13001862.

Appendix

APPENDIX A – OPTICAL MODEL ALGORITHMS

Algorithm 2 Computation of the shaded area on mirror i

Result: S_i

$\Delta S_i = -L_{mirr}/2$

if $\beta_i \geq \beta_{i+1} \geq 0$ ***and*** $h_t \leq 0$ *e* $i < n_{mirr}$ **then**

$\xi_i = 90^o - h_t - \beta_{i+1}$

$S_{H,i} = \frac{L_{mirr}}{2} \frac{sin(\xi_i)}{sin(90^o + h_t)}$

$\Delta S_{H,i} = S_{H,i} - (L_{mirr} + \Delta x)$

$\varphi_i = 90^o - h_t - \beta_i$

$\Delta S_i = \Delta S_{H,i} \frac{sin(90^o + h_t)}{sin(\varphi_i)}$

$S_i = \Delta S_i + \frac{L_{mirr}}{2}$

else if $\beta_i \leq \beta_{i-1} \leq 0$ ***and*** $h_t \geq 0$ *e* $i > 1$ **then**

$\xi_i = 90^o - h_t - \beta_{i-1}$

$S_{H,i} = \frac{L_{mirr}}{2} \frac{sin(\xi_i)}{sin(-90^o + h_t)}$

$\Delta S_{H,i} = S_{H,i} - (L_{mirr} + \Delta x)$

$\varphi_i = -90^o - h_t - \beta_i$

$\Delta S_i = \Delta S_{H,i} \frac{sin(-90^o + h_t)}{sin(\varphi_i)}$

$S_i = \Delta S_i + \frac{L_{mirr}}{2}$

end

if $S_i < 0$ **then**

$S_i = 0$

else if $S_i > L_{mirr}$ **then**

$S_i = L_{mirr}$

end

Algorithm 3 Computation of the illuminated band reflected by mirror *i* on the absorber's plane.

Result: $x'^{abs}_{1,i}, x'^{abs}_{2,i}$ e S^{mid}_i

initialization $x'^{abs}_{1,i} = x^{abs}_{1,i}$,$x'^{abs}_{2,i} = x^{abs}_{2,i}$, $S^{mid}_i = 0$

if $h_t < 0$ **then**

$\sigma_i = -2\theta_{t,i} + 90^o + h_t$

$\Delta L_i = \frac{E_{abs}}{tan(\sigma_i)}$

$x^{abs}_{c,i} = x_i + \Delta L_i$

$\eta_i = 90^o - h_t - \beta_i + 2\theta_t$

$\delta S_i = S_i \frac{sin(\eta_i)}{sin(\sigma_i)}$

$\delta x_i = \frac{L_{mirr}}{2} \frac{sin(\eta_i)}{sin(\sigma_i)}$

$x^{abs}_{1,i} = x^{abs}_{c,i} - \delta x_i$

$x^{abs}_{2,i} = x^{abs}_{c,i} + \delta x_i - \delta S_i$

$x^{mirr}_{1,abs} = \frac{E_{abs}}{tan(90^o + h_t) - \frac{L_{abs}}{2}}$

$x^{mirr}_{2,abs} = \frac{E_{abs}}{tan(90^o + h_t) + \frac{L_{abs}}{2}}$

if $x^{mirr}_{2,abs} > x^{mirr}_{1,i}$ *e* $x^{mirr}_{2,abs} < x^{mirr}_{2,i}$ **then**

if $x^{mirr}_{1,abs} < x^{mirr}_{2,i}$ *e* $x^{mirr}_{1,abs} > x^{mirr}_{1,i}$ **then**

$S^{mid}_i = 1$

else

$x'^{abs}_{1,i} = x^{abs}_{1,i} + (x^{mirr}_{2,abs} - x^{mirr}_{1,i})$

end

end

if $x^{mirr}_{1,abs} < x^{mirr}_{2,i}$ *e* $x^{mirr}_{1,abs} > x^{mirr}_{1,i}$ **then**

if $x^{mirr}_{2,abs} > x^{mirr}_{1,i}$ *e* $x^{mirr}_{2,abs} < x^{mirr}_{2,i}$ **then**

$S^{mid}_i = 1$

else

$x'^{abs}_{2,i} = x^{abs}_{2,i} + (x^{mirr}_{1,abs} - x^{mirr}_{2,i})$

end

end

if $h_t \geq 0$ **then**

$\sigma_i = 2\theta_{t,i} + 90^o - h_t$

$\Delta L_i = \frac{E_{abs}}{tan(\sigma_i)}$

$x_{c,i}^{abs} = x_i - \Delta L_i$

$\eta_i = 90^o + h_t + \beta_i - 2\theta_t$

$\delta S_i = S_i \frac{sin(\eta_i)}{sin(\sigma_i)}$

$\delta x_i = \frac{L_{mirr}}{2} \frac{sin(\eta_i)}{sin(\sigma_i)}$

$x_{1,i}^{abs} = x_{c,i}^{abs} - \delta x_i$

$x_{2,i}^{abs} = x_{c,i}^{abs} + \delta x_i - \delta S_i$

$x_{1,abs}^{mirr} = \frac{E_{abs}}{tan(90^o - h_t) - \frac{L_{abs}}{2}}$

$x_{2,abs}^{mirr} = \frac{E_{abs}}{tan(90^o - h_t) + \frac{L_{abs}}{2}}$

if $x_{2,abs}^{mirr} > x_{1,i}^{mirr}$ *and* $x_{2,abs}^{mirr} < x_{2,i}^{mirr}$ **then**

if $x_{1,abs}^{mirr} < x_{2,i}^{mirr}$ *and* $x_{1,abs}^{mirr} > x_{1,i}^{mirr}$ **then**

$S_i^{mid} = 1$

else

$x_{1,i}'^{abs} = x_{1,i}^{abs} + (x_{2,abs}^{mirr} - x_{1,i}^{mirr})$

end

end

if $x_{1,abs}^{mirr} < x_{2,i}^{mirr}$ *and* $x_{1,abs}^{mirr} > x_{1,i}^{mirr}$ **then**

if $x_{2,abs}^{mirr} > x_{1,i}^{mirr}$ *and* $x_{2,abs}^{mirr} < x_{2,i}^{mirr}$ **then**

$S_i^{mid} = 1$

else

$x_{2,i}'^{abs} = x_{2,i}^{abs} + (x_{1,abs}^{mirr} - x_{2,i}^{mirr})$

end

end

Algorithm 4 Computation of the incidence factor τ_t;

Result: τ_t

$\tau_t = 0$

foreach i;$1 \leq i \leq n_{mirr}$ **do**

  $x_{inf} = -L_{abs}$

  $x_{sup} = L_{abs}$

  $\theta_t^{abs} = -\theta_t - \beta_i$

  if $x_{1,i}^{\prime abs} > x_{inf}$ **then**

    $x_{inf} = x_{1,i}^{\prime abs}$

  end

  if $x_{2,i}^{\prime abs} < x_{sup}$ **then**

    $x_{sup} = x_{2,i}^{\prime abs}$

  end

  if $(x_{1,i}^{\prime abs} < -L_{abs}/2$ *and* $x_{2,i}^{\prime abs} < -L_{abs}/2)$ *or* $(x_{1,i}^{\prime abs} > L_{abs}/2$ *and* $x_{2,i}^{\prime abs} > L_{abs}/2)$ **then**

    $\chi_i = 0$

  else

    $\chi_i = x_{sup} - x_{inf}$

    if $S_i^{mid} == 1$ **then**

      $\chi_i = \chi_i - L_{abs}$

    end

  end

  $\tau_i = cos(\theta_t^{abs})\chi_i / L_{abs}$

end

$\tau_t = \sum_{i=1}^{i \leq n_{mirr}} \tau_i$

Algorithm 5 Computation of the incidence factor τ_l;

Result: τ_l

$\tau_l = 0$

if $C_{abs} > E_{abs} tan(h_l)$ **then**

  $\tau_L = (C_{abs} - E_{abs} tan(h_l)) \frac{\tau_t cos(h_l)}{C_{mirr}}$

else

  $\tau_l = 0$

end

Algorithm 6 Computation of de the minimal inclination of a mirror

Result: β_i^{min}

$\theta_{t,i} = h_t + \beta_i^{min}$

$L_{y,i} = (\frac{L_{mirr}}{2})\, sin(\beta_i^{min})$

$L_{x,i} = (\frac{L_{mirr}}{2})\, cos(\beta_i^{min})$

if $h_t \leq 0$ **then**

$\alpha_i = 90^o + 2\theta_{t,i} - h_t$

$\delta_x = \frac{(E_{abs} - L_{y,i})}{tan(\alpha_i)}$

else

$\alpha_i = 90^o - 2\theta_{t,i} + h_t$

$\delta_x = \frac{-(E_{abs} - L_{y,i})}{tan(\alpha_i)}$

end

Solve for β_i^{min} : $x_i + L_{x,i} - \delta_x + \frac{L_{abs}}{2} = 0$

Algorithm 7 Computation of de the maximal inclination of a mirror

Result: β_i^{max}

$\beta_i^{max} = 0$

$\theta_{t,i} = h_t + \beta_i^{max}$

$L_{y,i} = (\frac{L_{mirr}}{2})\, sin(\beta_i^{max})$

$L_{x,i} = (\frac{L_{mirr}}{2})\, cos(\beta_i^{max})$

if $h_t < 0$ **then**

$\alpha_i = 90^o + 2\theta_{t,i} - h_t$

$\delta_x = \frac{(E_{abs} + L_{y,i})}{tan(\alpha_i)}$

else

$\alpha_i = 90^o - 2\theta_{t,i} + h_t$

$\delta_x = \frac{-(E_{abs} + L_{y,i})}{tan(\alpha_i)}$

end

Solve for β_i^{max} : $0 = x_i - L_{x,i} - \delta_x - \frac{L_{abs}}{2}$